

THESIS

DYNAMIC ANALYSIS AND FATIGUE ASSESSMENT OF BRIDGE DECKS SUBJECTED
TO TRAFFIC AND CORROSION EFFECTS

Submitted by

Abdalmaged Salem

Department of Civil and Environmental Engineering

In partial fulfillment of the requirements

For the Degree of Master of Science

Colorado State University

Fort Collins, Colorado

Spring 2013

Master's Committee:

Advisor: Suren Chen

Hussam Mahmoud

Mehmet Egemen Ozbek

ABSTRACT

DYNAMIC ANALYSIS AND FATIGUE ASSESSMENT OF BRIDGE DECKS SUBJECTED TO TRAFFIC AND CORROSION EFFECTS

Fatigue damage has become one of the most common degradation mechanisms of highway bridge decks, which is primarily caused by passing traffic. The increase of heavy traffic over recent years, especially those overweight trucks, further worsens the situation. In the mean time, highway bridges are subjected to various aggressive environmental conditions leading to serious corrosion problems. Corrosion problem, faced by millions of reinforced concrete structures worldwide, can cause deterioration of the reinforcing steel bars, cracks and spalling on the bridge deck surface. As the bridge deck surface deteriorates over time, the road surface roughness profile will vary accordingly. The varying surface roughness profiles over time will generate increased dynamic loads on the bridge decks through dynamic interaction between surface roughness, vehicles of stochastic traffic and bridge structures. The increased dynamic loads, coupled by the reinforcement deterioration of bridge deck due to corrosion, will further cause accelerated response and fatigue accumulations on the bridge deck. Such a nonlinear time-progressive process continues over time throughout the lifespan of the bridge deck, which has not been systematically characterized or studied. The present study aims to characterize the coupling effects between the time-varying dynamic loads from stochastic traffic, deterioration bridge decks due to corrosion, and bridge performance. To tackle such a problem, firstly, a hybrid FEM-based analytical strategy is developed for the bridge and stochastic traffic system considering the time-dependent corrosion process. Secondly, scenario-based numerical studies are conducted for the typical combinations of traffic, corrosion-induced reinforcement

deterioration and associated surface profile variations. Finally, based on the numerical findings, the fatigue damage of the bridge deck over time is analyzed and the remaining life of the prototype bridge decks is assessed under the joint effect of corrosion and stochastic traffic.

ACKNOWLEDGEMENTS

First and foremost, I would like to thank my god who had answered my prayers to finish this thesis. I also want to thank my advisor Dr. Suren Chen for giving his time, patience, assistance, contribution, continuous support and advice that I need and for his moral support to graduate.

On this research, I was so glad to deal with Yufen Zhou and Matt Hardmen who had given me their hands and I give them all my respect and appreciation.

At the last, special thanks to my family, country, parents, friends for trusting and believing me. I want to acknowledge all their sacrifices and express my heartfelt gratitude

TABLE OF CONTENTS

ABSTRACT.....	ii
ACKNOWLEDGEMENTS.....	iv
TABLE OF CONTENTS.....	v
LIST OF TABLES.....	vii
LIST OF FIGURES.....	viii
Chapter 1: Introduction and Background.....	1
Chapter 2: Review of Corrosion Models and Bridge Deck Damage Assessment.....	6
2.1 Review of Corrosion Models.....	6
2.1.1 Time to Corrosion Initiation.....	6
2.1.2 Crack Initiation (t_{1st}).....	13
2.1.3 Crack Propagation (t_{ser}).....	16
2.1.4 Time to Severe Cracking.....	17
2.1.5 The Corrosion Rate.....	17
2.1.6 Reduction of Nominal Moment Strength Due to Corrosion.....	21
2.2 Deterioration Mechanism in RC Decks.....	24
2.3 Bridge Deck Damage Assessment.....	25
2.3.1 Introduction.....	25
2.3.2 S-N Curves Approach.....	26
2.3.3 Palmgren-Miner's Rule.....	28
2.3.4 Rainflow Cycles Counting Method.....	29
Chapter 3: Hybrid Analytical Models and the Prototype Bridge.....	37
3.1 The Prototype Bridge.....	37
3.1.1 Historical Overview.....	37
3.1.2 Bridge Description and Geometry.....	37
3.2 Refined-Scale Finite Element Bridge Model with SAP2000.....	43
3.2.1 Introduction.....	43
3.2.2 Superstructure.....	43
3.2.3 Bent Cap.....	45
3.2.4 Piers.....	46
3.3 Reduced-DOF Bridge/Vehicle/Roughness Model.....	49

3.3.1 Reduced-DOF Bridge Model	49
3.3.2 Vehicle and Bridge Models.....	49
3.3.3 Interaction of Vehicle and Bridge.....	50
3.3.4 Road Surface Roughness Condition	52
3.4 Time History Input of Deck Node Forces from Stochastic Traffic with Dynamic interaction.....	53
3.4.1 Equivalent Dynamic Wheel Load Database of Various Traffic Scenarios	53
3.4.2 Stochastic Traffic Flow Simulation	53
3.4.3 Assemble Cumulative Dynamic Wheel Load from Stochastic Traffic Flow.....	54
3.4.4 Assemble Time-History Input of Bridge Deck Node Forces in Refined SAP Model	55
3.5 Nonlinear Time Domain Dynamic Analysis with Refined-Scale SAP Model	55
Chapter 4: Time-progressive Dynamic Analysis and Fatigue Assessment Methodology of Bridge Deck Subjected to Traffic and Corrosion.....	57
4.1 Scenario-Based Fatigue Damage Model for a Typical Year	57
4.1.1 Categorization of the Representative Scenarios.....	57
4.1.1.1 Roughness Representative Scenarios.....	57
4.1.1.2 Corrosion Representative Scenarios.	58
4.1.1.3 Traffic Representative Scenarios	64
4.1.1.4 Combination of Traffic Flow and Corrosion	65
4.1.2 Calculating Cumulative Fatigue Damage Factor for a Typical Hour.	66
4.1.2.1 Obtaining Stress Time History of the Bridge.....	67
4.1.2.2 Using Rainflow Cycles Counting Method to Decompose the Stress Time Histories	67
4.1.2.3 S-N Curves.....	68
4.1.2.4 The Miner's Rule Method.....	69
4.2 Time-Progressive Dynamic Analysis Procedure	69
Chapter 5: Results of Fatigue Assesment of the Bridge Deck	72
5.1. Overview.....	72
5.2 The Resultant Stresses	72
5.3. The Results from the Rainflow Cycles Counting Method.....	76
5.4. Fatigue Damage Indices for Each Representative Scenario	83
Chapter 6: Conclusion	102
Bibliography	105

LIST OF TABLES

Table 2.1: Surface chloride concentration	8
Table 3.1: The properties of structural members	39
Table 3.2: Girders dimensions	41
Table 3.3: Different types of modeling were used for different components of the bridge	47
Table 4.1: Road-Roughness Coefficient (RRC) values for road-roughness coefficient.....	58
Table 4.2: Statistical parameters for corrosion variables and the concrete bridge deck material properties and dimensions.....	59
Table 4.3: Three levels of service adopted in this study.....	64
Table 4.4: The combined representative scenarios	66
Table 5.1 : Fatigue life for each node of the four elements chosen in this study (years).	85
Table 5.2: Hourly fatigue damage factors DFi for each joint of the four elements chosen for each particular scenario.....	86
Table 5.3: Total hours for each representative traffic condition to occur in each year	89
Table 5.4 the cumulative damage factor for each typical year of each of the representative corrosion conditions.....	89

LIST OF FIGURES

Figure 1.1: The silver bridge collapse (1967),.....	2
Figure 1.2: Concrete spalling due to corrosion (Feldmann 2008)	4
Figure 2.1: Cady and Weyers model (1983).....	12
Figure 2.2: Crack width changes with time	14
Figure 2.3: Changing of the corrosion rate with time based on Vu and Stewart model	18
Figure 2.4: Changing of the corrosion rate with concrete cover based on Scott 2004 model	20
Figure 2.5: Fatigue category based on number of cycles to failure (Thun 2006).....	26
Figure 2.6: Typical S-N Curves	27
Figure 2.7: Hysteresis loops in the stress-strain behavior (Socie & Downing 1982).....	30
Figure 2.8: Example of Rainflow cycles method (Mazzolani 2000).....	32
Figure 2.9(a): Example of Rainflow cycles method (ASTM 1985)	33
Figure 2.9(b): Example of Rainflow cycles method (ASTM, 1985)	34
Figure 2.9(c): Example of Rainflow cycles method (ASTM 1985)	34
Figure 2.9(d): Example of Rainflow cycles method (ASTM 1985).....	35
Figure 2.9(e): Example of Rainflow cycles method (ASTM 1985)	35
Figure 2.9(f): Example of Rainflow cycles method (ASTM 1985).....	36
Figure 3.1: The plan view of the 104th bridge.....	38
Figure 3.2: The elevation of the 104th bridge.....	38
Figure 3.3: Typical Section in the Bridge	40
Figure 3.4: Typical elevation, plan and section of the girder	40
Figure 3.5: Detailed section in approach slab	41
Figure 3.6: Typical caisson detail at abutment	42
Figure 3.7: Typical caisson detail at pier	42
Figure 3.8: 3D view of the finite element model of the bridge.....	44
Figure 3.9: Shell elements plates were used to model the bridge deck	44
Figure 3.10: Cross section in the girder modeled	45
Figure 3.11: Cross section of the bent cap	46
Figure 3.12: Cross section of the caisson modeled.....	47
Figure 3.13: Cross section of the abutment modeled.....	48
Figure 3.14: Cross section of the column modeled.....	48
Figure 3.15: Vehicle model.....	50
Figure 3.16: Hybrid bridge dynamic analytical model	56
Figure 4.1: Time invariant corrosion rate	61
Figure 4.2: A_0/A_t for time variant corrosion rate	62
Figure 4.3: A_0/A_t for time invariant corrosion rate	62
Figure 4.4: Moment of inertia for time invariant corrosion rate.....	63
Figure 4.5A: Steps for calculating fatigue damage factor for each typical year.....	66
Figure 4.5B: Steps for calculating fatigue damage factor for each typical year.....	66
Figure 4.6: S-N curve equation.....	68
Figure 4.7: Time-progressive analysis procedure with hybrid dynamic analytical model	71
Figure 5.1A: Joint locations and numbers	73
Figure 5.1.B: locations of the elements chosen in this study.....	73
Figure 5.2: Stress amplitudes versus time steps for heavy, moderated and light traffic for joint#	

1580.....	74
Figure 5.3: Stress amplitudes versus time steps for Heavy, Light traffic under Good Roughness and Medium-Corrosion conditions for joint #1565	74
Figure 5.4: Stress amplitudes versus time steps for Heavy, Moderate traffic under Very-Good Roughness and No-Corrosion conditions for joint # 1580	75
Figure 5.5: Stress amplitudes versus time steps for No-Corrosion conditions (Very-Good roughness) and Medium-Corrosion conditions (Good roughness) under Moderate traffic for joint #1559.....	75
Figure 5.6: Stress ranges amplitudes versus Number of cycles for the heavy traffic (Joint#1580)	77
Figure 5.7: Stress ranges amplitudes and mean classes versus number of cycles for the heavy traffic (Joint#1580)	77
Figure 5.8: Stress ranges amplitudes versus Number of cycles for the moderate traffic (Joint#1580)	78
Figure 5.9: Stress ranges amplitudes and mean classes versus number of cycles for the moderated traffic (Joint#1580)	78
Figure 5.10: Stress ranges amplitudes versus Number of cycles for the Light traffic (Joint#1580)	79
Figure 5.11: Stress ranges amplitudes and mean classes versus number of cycles for the light traffic (Joint#1580)	79
Figure 5.12: Stress ranges amplitudes versus Number of cycles for the Light traffic (Joint# 914)	80
Figure 5.13: Stress ranges amplitudes and mean classes versus number of cycles for the heavy traffic (Joint# 914)	80
Figure 5.14: Stress ranges amplitudes versus Number of cycles for the Light traffic (Joint# 914)	81
Figure 5.15: Stress ranges amplitudes and mean classes versus number of cycles for the heavy traffic (Joint# 914)	81
Figure 5.16: Stress ranges amplitudes versus Number of cycles for the Light traffic (Joint#914)	82
Figure 5.17: Stress ranges amplitudes and mean classes versus number of cycles for the heavy traffic (Joint#914)	82
Figure 5.18 Fatigue damage index surface under different vehicle densities and corrosion effects for joint #899.....	92
Figure 5.19 Cumulative damage facto versus service life for joint #899	92
Figure 5.20 Fatigue damage index surface under different vehicle densities and corrosion effects for joint #1232.....	93
Figure 5.21 Cumulative damage facto versus service life for joint #1232	93
Figure 5.22 Fatigue damage index surface under different vehicle densities and corrosion effects for joint #914.....	94
Figure 5.23 Cumulative damage facto versus service life for joint #914	94
Figure 5.24 Fatigue damage index surface under different vehicle densities and corrosion effects for joint #1211.....	95
Figure 5.25 Cumulative damage facto versus service life for joint #1211	95
Figure 5.26 Fatigue damage index surface under different vehicle densities and corrosion effects for joint #1241.....	96

Figure 5.27 Cumulative damage facto versus service life for joint #1241	96
Figure 5.28 Fatigue damage index surface under different vehicle densities and corrosion effects for joint #1247.....	97
Figure 5.29 Cumulative damage facto versus service life for joint #1247	97
Figure 5.30 Fatigue damage index surface under different vehicle densities and corrosion effects for joint #1580.....	98
Figure 5.31 Cumulative damage facto versus service life for joint #1580	98
Figure 5.32 Fatigue damage index surface under different vehicle densities and corrosion effects for joint #1544.....	99
Figure 5.33 Cumulative damage facto versus service life for joint #1544	99
Figure 5.34 Fatigue damage index surface under different vehicle densities and corrosion effects for joint #1559.....	100
Figure 5.35 Cumulative damage facto versus service life for joint #1559	100
Figure 5.36 Fatigue damage index surface under different vehicle densities and corrosion effects for joint #1226.....	101
Figure 5.37 Cumulative damage facto versus service life for joint #1226	101

Chapter 1: Introduction and Background

The U.S. infrastructure and transportation systems are considered as the backbone of the nation's economy and the key to the economic growth. The infrastructure and transportation systems importance has been described as following "the infrastructure supporting human activities includes complex and interrelated physical, social, ecological, economic, and technological systems such as transportation, energy production and distribution; water resources management; waste management; facilities supporting urban and rural communities; communications; sustainable resources development; and environmental protection." (Wright1995)

According to FHWA, nearly 270 million residents and 7 million business establishments benefit from a high level of mobility and freight activity as results of the U.S. infrastructure and transportation system (FHWA 2002). The quality of the transportation system not only influences the quality of life due to delay and congestion, but also affects the safety of thousands of drivers every day. Highway bridges become the critical component of any transportation systems by providing vital connection to roadways, across valleys or other natural barriers. In the United States, there are about 583,000 bridges around the nation, 235,000 of which are made of conventional reinforced concrete (FHWA 2002). A major challenge for modern bridges, especially the concrete bridges, is the demand of frequent repair and maintenance to keep necessary serviceability due to constant condition deterioration, material degradation and growing traffic. The increase of heavy traffic over recent years, especially those overweight trucks, further worsens the situation. According to High Capacity Manual, the heavy trucks contribute more than 50% of overall pavement damage with less than 20% of the total traffic volume (HCM 2010). The repairs of bridge decks are usually costly, not only due to the direct

cost of repair, but also due to the indirect cost from the traffic disruption during the repair action (Oh et al. 2007).

In the last few years, significant concerns arise about the combined deterioration from both fatigue and corrosion (Corrosion fatigue) (Tanaka et al. 2009). This is especially true for many existing bridges, which have been designed with the old specification. The collapse of the Silver Bridge (1967) in Ohio State (Figure 1.1), which was been blamed for the loss of 46 lives and millions of dollars, is a good example of corrosion fatigue collapses (LeRose 2001).



Figure 1.1: The silver bridge collapse (1967),

Source: (Lonaker, 2006)

Highway Bridges are exposed to various aggressive environmental conditions. One of the most common aggressive conditions is the aggressive attack from Chloride Ions which causes steel bars corrosion, leading to concrete deterioration, e.g. concrete spalling (see Figure 1.2).

This kind of corrosion usually occurs in highway bridges located in the coastal areas, where the air is full of chloride ions. The Federal Highway Administration (FHWA) has reported that around 15% of the bridges in the United States are in need of some sort of repair, because of steel and reinforcement steel corrosion (FHWA 2002). The report also estimated that the corrosion of bridges costs the nation around 8.3\$ billion, not including the indirect costs to the user due to traffic delays. Due to the ingress of deicing salts into the concrete from sea spray, the chloride contents in the concrete will increase until it reaches a threshold limit value for corrosion initiation in the reinforcement bars. Reinforcement steel bars will be corroded by the influence of chloride ingress causing bar-area reduction. Consequently, concrete strength will decrease as the reinforcement bar area gets smaller. Also, the use of road salts and chemicals to remove the ice accumulated on bridge decks will also lead to reinforcing steel corrosion and rapid degradation of existing concrete bridge decks (Yehia 1998).

At the same time, highway bridges are subjected to dynamic forces due to moving vehicles. The repetitive loads from vehicles, although typically not large enough to cause strength failure, may cause damage accumulation due to fatigue on bridges (Tong 2011). Such a situation becomes more serious with the increase of the number of overloaded vehicles recently (Oh et al. 2007). Fatigue, as defined in materials science, is the progressive and localized structural damage that occurs when material is subjected to cyclic or fluctuating strains at nominal stresses much less than the ultimate tensile stress limit (Bond & harris 2008).

One of the most important components of the superstructure of bridges is the bridge decks. The bridge decks are directly exposed to both daily traffic loads and environmental attacks, which make them the most rapidly deteriorating component of bridges (Nasvik 2003). At the same time, bridge decks are considered as the most expensive component to construct and

repair of a bridge in North America (Lounis 2003). The review of existing bridges shows extensive deterioration has been found to be a result of “the corrosion of reinforcing steel due to the application of de-icing chemicals in winter, freezing and thawing cycles, along with direct impact from traffic loads” (Lounis 2003).

The most employed approach to evaluate the fatigue damage is the S-N curves approach (Rigo 2011). The S-N curves describe the relationship between stress ranges and load cycles. Stress ranges and load cycles are plotted in log-log scales, where the vertical scale is for stress ranges and the horizontal one represents the load cycles. The S-N curves approach is usually used to determine the number of cycles to failure caused by constant stress amplitude (Siemes 1982). The cumulative damage due to fatigue for a structure subjected to complex loading is typically assessed by the Palmgren-Miner linear damage hypothesis, which will be discussed later in more detail.



Figure 1.2: Concrete spalling due to corrosion (Feldmann 2008)

The present study aims to characterize the coupling effects between the time-varying dynamic loads from stochastic traffic, deterioration bridge decks due to corrosion, and bridge performance. To tackle such a problem, firstly, a hybrid FEM-based analytical strategy is developed for the bridge and stochastic traffic system considering the time-dependent corrosion process. Secondly, scenario-based numerical studies are conducted for the typical combinations of traffic, corrosion-induced reinforcement deterioration and associated surface profile variations. Finally, based on the numerical findings, the fatigue damage of the bridge deck over time is analyzed and the remaining life of the prototype bridge decks is assessed under the joint effect of corrosion and stochastic traffic. The thesis has six chapters: Chapter 2 summarizes the literature review; the hybrid analytical model is introduced in Chapter 3; based on the hybrid analytical model, the time-progressive dynamic analysis procedure is discussed in Chapter 4; the fatigue assessment of the bridge deck is made in Chapter 5 and Chapter 6 concludes the study.

Chapter 2: Review of Corrosion Models and Bridge Deck Damage Assessment

2.1 Review of Corrosion Models.

The determination of the amount of the penetrated chloride content through the protective cover depth can be made through the chloride diffusion analysis (Oh et al. 2007). Furthermore, when the chloride content around the reinforcement exceeds a threshold value, the corrosion of steel bars will initiate, leading to concrete deterioration and performance reduction of bridge deck (Masi 1997). The chloride-induced corrosion depends on diffusion coefficient, surface chloride concentration and threshold chloride value (Wang 2010). According to the study by Khatri et al (2004), the surface chloride concentration has larger influence on the service life of the structure than the threshold value of chloride content does. In this section, a detailed review of different models for the time to corrosion initiation, crack initiation, crack propagation, reduction of bar diameters and corrosion rate, will be conducted and the details are presented as following.:

2.1.1 Time to Corrosion Initiation

It is the time when the chloride concentration at a depth equals to the cover depth reaches threshold value (critical value) (T_i) (Guo 2006). There are many studies that have described the time to corrosion initiation in terms of the Chloride diffusion based on Fick's second law. The chloride content $C(x, t)$ at a distance x depth from the surface is defined as (Pelton 1972):

$$\frac{\partial C(x, t)}{\partial t} = D_{cl} \frac{\partial^2 C(x, t)}{\partial x^2} \quad \text{Equation 2.1}$$

The boundary conditions as shown below need to be satisfied:

$$C(0, t) = C_0 \text{ (The surface chloride content)}$$

$$C(x, 0) = 0$$

The general solution of Eq. (2.1) can be written as follows,

$$C(x, t) = C_0 \left[1 - \operatorname{erf} \left(\frac{x}{2\sqrt{D_{ch}t}} \right) \right] \quad \text{Equation 2.2}$$

where: C_0 is the surface chloride content; D_{ch} is the constant chloride diffusion coefficient; x is the distance from the concrete surface and erf represents the error function where:

$$\operatorname{erf}(\omega) = \frac{2}{\sqrt{\pi}} \int_0^{\omega} e^{-x^2} dx \quad \text{Equation 2.3}$$

To obtain the time to corrosion initiation, Equation (2.2) must be rearranged:

$$T_i = \frac{X^2}{4D_{ch} \left[\operatorname{erf} \left(1 - \frac{cr}{C_0} \right) \right]^2} \quad \text{Equation 2.4}$$

where:

cr = the chloride threshold concentration value.

T_i = the time to corrosion initiation.

Although wetting and drying cycles may change due to the climate changes from year to year which may cause fluctuation of the value of surface chloride concentration (Wang 2010), the surface chloride concentration is assumed to be a constant value. Val and

Stewart (2003) have assumed that the surface chloride concentration value can be assumed based on the location of the structure as in Table 2.1:

Table 2.1: Surface chloride concentration

Location	Mean	COV	Distribution
Splash zone	7.35 kg/m ³	0.7	Lognormal
Atmospheric zone on the coast	2.95 kg/m ³	0.7	Lognormal
Atmospheric zone >1 km from the coast	1.15 kg/m ³	0.5	Lognormal

Source: (Val 2003)

Various researchers have developed different models to predict the constant chloride diffusion coefficient. Bamforth has proposed a model to estimate the time initiation based on the apparent diffusion coefficient D_{ca} (Bamforth 1999).

$$D_{ca} = at^n \quad \text{Equation 2.5}$$

where: a is apparent diffusion coefficient at one year and n is an empirical constant.

The general form of the model can be written as following:

$$C(x, t) = C_0 \left[1 - \operatorname{erf} \left(\frac{x}{2 \sqrt{D_{ca} \left(\frac{t}{t_m} \right)^n \times t}} \right) \right] \quad \text{Equation 2.6}$$

A new model was proposed by Mangant and Molloy (1994) taking into account that the diffusion coefficient is time invariant. They have proposed that the diffusion coefficient can be found using the following formula (Mangat & Molloy 1994):

$$D_c = D_i \times t^{-m} \quad \text{Equation 2.7}$$

where:

D_c : is the effective diffusion coefficient at time t (cm²/s).

D_i : Effective diffusion coefficient at time t equal to 1 second.

t : is the time in seconds.

m : is an empirical coefficient that varies with mixture proportions and it can be found using the following equation:

$$m = 2.5 \left(\frac{W}{C} \right) - 0.6 \quad \text{Equation 2.8}$$

The general form of the model can be written as following:

$$C(x, t) = C_0 \left[1 - \operatorname{erf} \left(\frac{x}{2 \sqrt{\frac{D_i}{1-m} t^{1-m}}} \right) \right] \quad \text{Equation 2.9}$$

Papadakis (1992) has suggested a model to predict the constant chloride diffusion coefficient using the following formula:

$$D_{ch} = 0.15 * \frac{1 + \rho_c \frac{w}{c}}{1 + \rho_c \frac{w}{c} + \frac{\rho_c a}{\rho_a c}} \left[\frac{\rho_c \frac{w}{c} - 0.85}{1 + \rho_c \frac{w}{c}} \right]^3 * D_{Cl,H_2O} \quad \text{Equation 2.10}$$

where ρ_c is the mass density of cement , ρ_a is the mass density of aggregate, a/c is the aggregate to cement ratio , D_{Cl,H_2O} is the diffusion coefficient of chloride equals to $1.6*10^{-9} \text{ m}^2/\text{s}$ at 25° and w/c is the water –cement ratio based on the concrete compressive strength (f_{ycl}) and it can be found by using Bolomey’s formula (Bazant 1983) :

$$\frac{w}{c} = \frac{27}{f_{ycl} + 13.5} \quad \text{Equation 2.11}$$

The aggregate to cement ratio a/c can be calculated based on the water –cement ratio (Wang 2010):

$$\frac{a}{c} = \frac{s}{c} + \frac{g}{c} \quad \text{Equation 2.12}$$

where:

$$s/c \text{ (Sand to cement ratio)} = 6.703 \frac{w}{c} - 0.084 \quad \text{Equation 2.13}$$

$$g/c \text{ (Gravel to cement ratio)} = 6.364 \frac{w}{c} - 0.258 \quad \text{Equation 2.14}$$

If chloride diffusion coefficient is considered to be time-variant, the following equation can be used in terms of the constant chloride diffusion coefficient (D_{ch}) (DuraCrete 2000)

$$D_{cht} = \sqrt{K_e K_t K_c (D_{ch}) \left(\frac{t_0}{t} \right)^n} \quad \text{Equation 2.15}$$

where:

$n = 0.3$ (submerged members), $n = 0.37$ (members in tidal and splash zones) and $n = 0.65$ (atmospheric)

Environmental factor (K_e):

$K_e = 1.325$ (submerged)

$K_e = 0.924$ (tidal)

$K_e = 0.265$ (splash)

$K_e = 0.676$ (atmospheric)

Curing factor $K_c = 1.0$ (7 days)

Test method $K_t = 1.0$

$t_0 = 1$ year.

Cady and Weyers (1993) have proposed a model to predict the remaining service life of bridge decks in corrosive environments. The salt-induced corrosion of the steel has been considered as the main reason of deck deterioration. In the study, the service model of the bridge deck consists of four time periods as following (see Figure 2.1):

1-Subsidence cracking period: Subsidence cracking period is the period of time when cracks appear due to construction faults.

2-Chloride diffusion period: It is the time that chloride ions will take to penetrate through the concrete cover and to initiate corrosion at the lowest 2.5 percentile concrete cover. Fick's

second law was employed to estimate the diffusion time.

3-Corrosion of steel period: It is the period of time from time of initiation at the 2.5 percentile cover depth to first cracking of concrete cover.

4-Deterioration period: It is the time to reach a level of the allowed percent damage of the deck with a uniform deterioration rate. The allowed percent damage is defined as the end of functional service life.

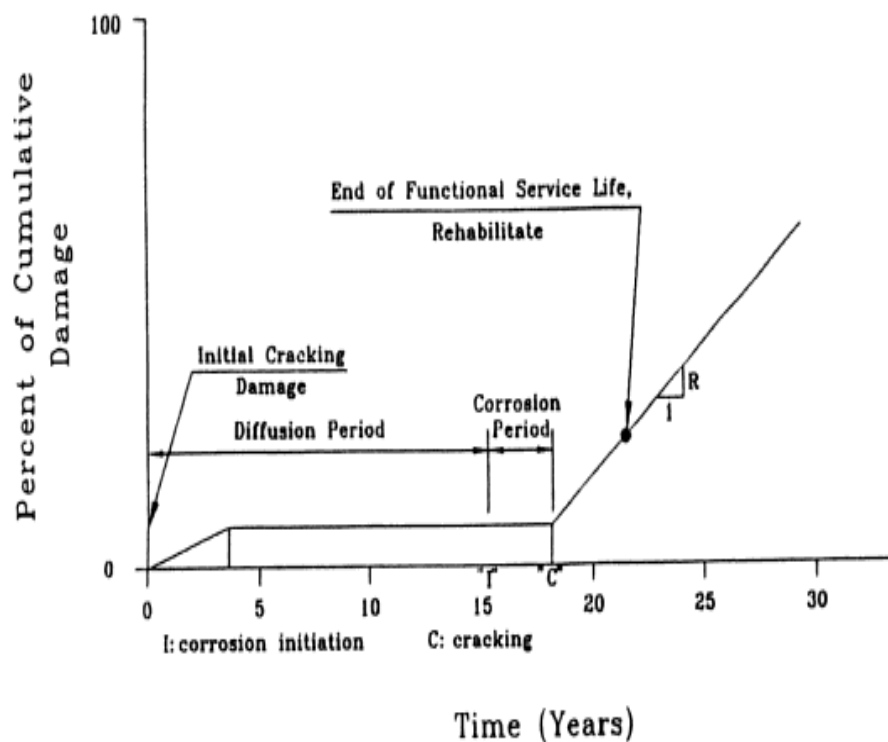


Figure 2.1: Cady and Weyers model (1983)

However, there is a huge discrepancy between the estimated time initiation from the previous models and the data observed from laboratories and fields. According to Williamson (2007), the Mangant and Molot model is not efficient because people cannot make several measurements of the effective diffusion coefficient at time t unless “multiple measurements of

Dc [are] made on a given mixture over a period of time and a regression analysis performed." Additionally, the estimation of m is not always correct. Williamson (2007) also pointed out that "the model assumes that the first exposure to chlorides occurs at t = 1 second, which will result in the overestimation of chloride concentrations."

2.1.2 Crack Initiation (t_{1st})

It is the time from corrosion initiation to the time when the first visible crack of approximately 0.05mm appears (t_{1st}). Many studies have shown that crack initiation occurs after a short time from corrosion initiation, while the time that a crack takes to propagate to the limit crack width is longer (see Figure 2.2) (Mullard & Stewart 2009). Maaddawy & Soudki (2007) suggested that the time to crack initiation can be calculated with following equation:

$$t_{1st} = \left\{ \frac{7117.5(D + 2\delta_o)(1 + \nu + \Psi)}{365 i_{corr} E_{ef}} \right\} \left\{ \frac{2C \times f_t}{D} + \frac{2\delta_o E_{ef}}{(1 + \nu + \Psi)(D + 2\delta_o)} \right\} \quad \text{Equation 2.16}$$

where:

D = diameter of the steel reinforcing bar (mm)

δ_o = thickness of the porous zone around the steel reinforcing bar (0.015 mm)

ν = Poisson's ratio of concrete (0.2)

C = concrete cover (mm)

f_t = concrete tensile strength (MPa)

E_{ef} = effective elastic modulus of concrete (MPa)

i_{corr} = corrosion current density at temperature T =20°C ($\mu\text{A}/\text{cm}^2$)

$$\Psi = \frac{(D + 2\delta_o)^2}{2C(C + D + 2\delta_o)} \quad \text{Equation 2.17}$$

$$E_{ef} = \frac{E_c}{1 + \phi_{cr}}$$

Equation 2.18

where:

ϕ_{cr} = the creep coefficient.

E_c = the elastic modulus of concrete.

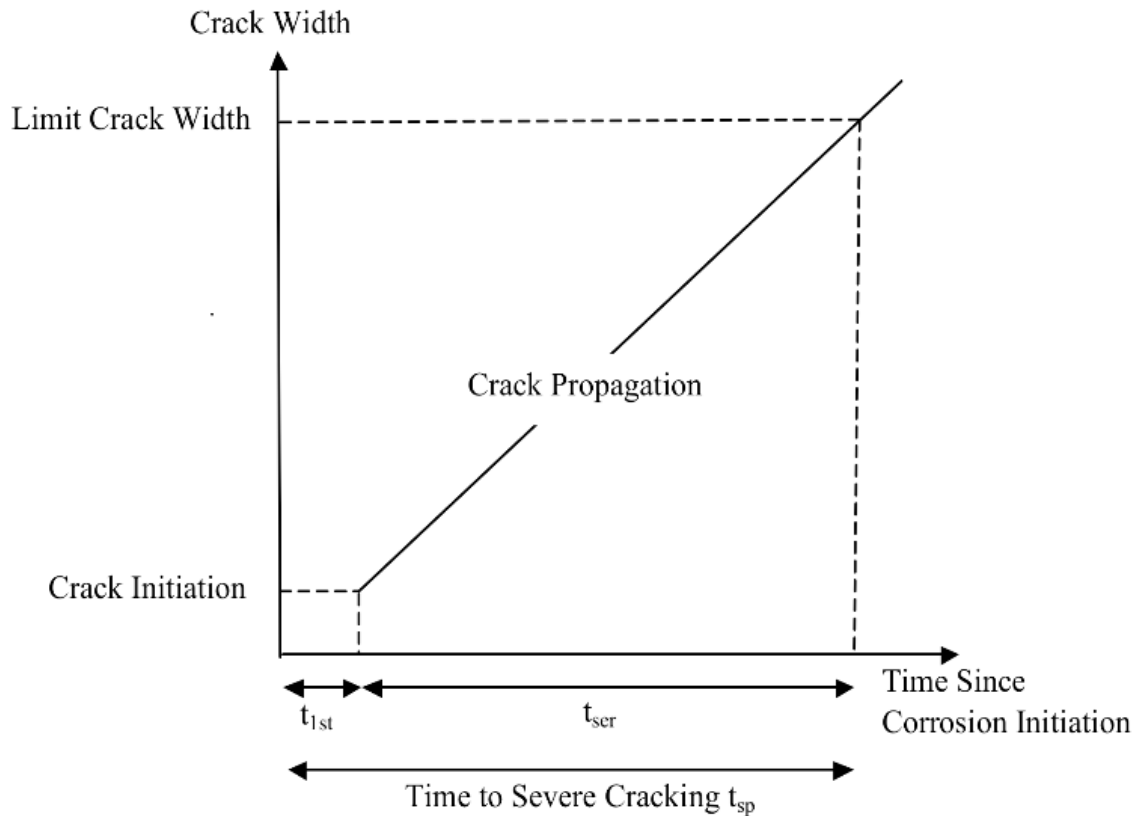


Figure 2.2: Crack width changes with time

Source: (Mullard & Stewart 2009)

For steady state corrosion, Bazant (1979) developed a physical-mathematical model to determine the time to cracking for chloride-induced corrosion of steel in concrete. He has suggested that the time to cracking for chloride-induced corrosion of steel in concrete can be

estimated based on corrosion rate, cover depth, spacing, tensile strength, modulus of elasticity, Poisson's ratio and creep coefficient.

The time to cracking for chloride-induced corrosion of steel in concrete for Bazant's model can be estimated based on the following formula:

$$t_{cr} = \rho_{cor} * \frac{D \Delta_D}{s * j_r} \quad \text{Equation 2.19}$$

where:

D = The diameter of the rebar

s = The bars spacing

j_r = The rate of rust production

Δ_D = The change in the diameter of the bar

ρ_{cor} = Function of mass densities of steel and rust and it can be found as follows:

$$\rho_{cor} = \left[\left(\frac{1}{\rho_r} \right) - \left(\frac{0.523}{\rho_{st}} \right) \right]^{-1} * \frac{\pi}{2} \quad \text{Equation 2.20}$$

where:

ρ_r , **ρ_{st}** are the mass densities of rust and steel respectively.

When the bar spacing **s** is less than six times the diameter of the rebar **D**, the change in the diameter of the bar **Δ_D** can be found using the following suggested formula:

$$\Delta_D = 2 f_t \frac{L}{D} \delta_{pp} \quad \text{Equation 2.21}$$

where:

f_t = the tensile strength of concrete.

δ_{pp} = the bar hole flexibility.

However, Liu (1996) stated that the estimated time initiation from Bazant's model is shorter than the time initiation observed from the laboratory data because the model is based on a linear approximation to estimate the growth of the rust products.

2.1.3 Crack Propagation (t_{ser})

It is the time for a crack to propagate from first visible crack (0.05mm) to a limit crack width (t_{ser}) (Mullard & Stewart 2009). Vu et al. (2005) have proposed a model to predict the time for crack propagation to a limit state of 1 mm based on an empirical model. The proposed model is obtained through accelerated corrosion tests conducted at the University of Newcastle involving eight RC slabs with 16 mm diameter reinforcing bars. The model defines the time for a crack to propagate to a width of 1 mm in terms of corrosion rate, concrete cover depth and water-cement ratio as following (Vu et al. 2005):

$$t_{ser} = K_R \frac{0.0114}{i_{corr}} \left[A \left(\frac{C}{\omega_c} \right)^B \right] \quad \text{Equation 2.22}$$

where: K_R is a correction factor that can be found from the following formula:

$$K_R = 0.95 \left[\exp \left(- \frac{0.3 \times i_{corr}(\text{exp})}{i_{corr}} \right) - \frac{i_{corr}(\text{exp})}{2500 i_{corr}} + 0.3 \right] \quad \text{Equation 2.23}$$

where: ω_c is the water-cement ratio, i_{corr} is the corrosion current density, $i_{corr}(\text{exp})$ is the accelerated corrosion rate, A and B are empirical constants depend on $i_{corr}(\text{exp})$ and the limit crack width (ω_{lim}). $i_{corr}(\text{exp}) = 100 \mu\text{A}/\text{cm}^2$, $A = 65$ and $B = 0.45$ for $\omega_{lim} = 0.3 \text{ mm}$ and $A = 700$ and $B = 0.23$ for $\omega_{lim} = 1.0 \text{ mm}$

2.1.4 Time to Severe Cracking

It is the time for cracking of the concrete surface to reach a limit crack width ω_{lim} since corrosion was initiated and it equals to the summarization of crack initiation (t_{1st}) and crack propagation(t_{ser}).

$$t_{sp} = t_{1st} + t_{ser} \quad \text{For} \quad 0.33 \text{ mm} \leq \omega_{lim} \leq 1.0 \text{ mm} \quad \text{Equation 2.24}$$

2.1.5 The Corrosion Rate

The corrosion rate is considered as the most effective parameter in corrosion-induced damage prediction of reinforced concrete bridge decks (Li et al. 2007). However, the corrosion rate is a function of different factors such as supplementary cementations materials, moisture content, cyclic wetting and drying and sustained loading, etc. (Otieno et al. 2011).

Based on the availability of oxygen at the steel surface, Vu and Stewart have developed a model to predict the corrosion rate for concrete structures (Vu & Stewart 2000). The availability of oxygen at the steel surface depends on several factors like: Concrete quality (w/c), concrete cover(C), temperature (T^o) and relative humidity (H) (Vu & Stewart 2000). They have suggested that the corrosion rate changes with the relative humidity. It comes close to zero when the relative humidity is less than 50%. When the relative humidity is between 75% and 90%, the corrosion rate reaches the highest value. However, when the relative humidity is higher than 90%, the corrosion rate equals zero. Stewart and Vu have found that the corrosion rate can be calculated using the following equation (Vu & Stewart 2000):

$$i_{corr} = i_{corr}(1) \times 0.85 \times (t - T_i)^{-0.29} \quad \text{Equation 2.25}$$

where: T_i is the time to corrosion initiation, and $i_{corr}(1)$ is the corrosion rate for one year since corrosion initiation and its value depends on the relative humidity and temperature:

$$i_{corr}(1) = \frac{27(1 - \omega c)^{-1.64}}{C} \quad \text{For 80\% humidity, 20 C}^\circ \quad \text{Equation 2.26}$$

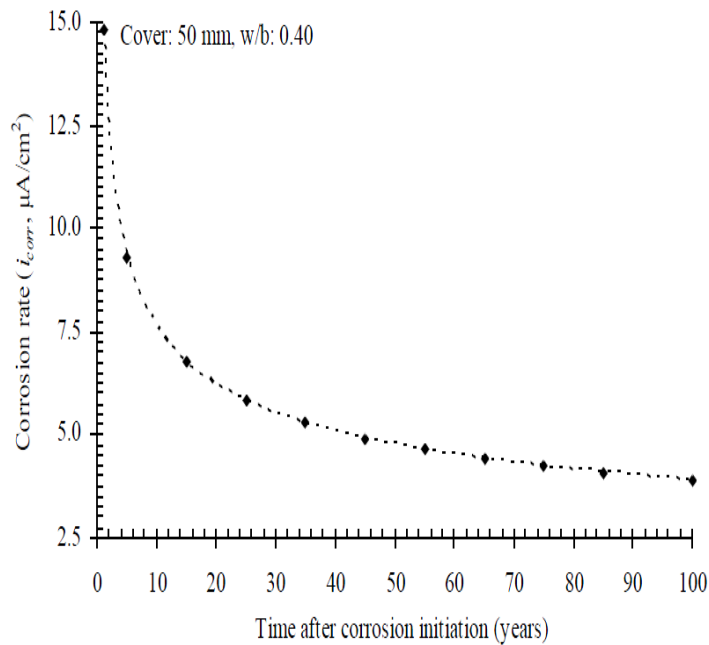


Figure 2.3: Changing of the corrosion rate with time based on Vu and Stewart model

Source: (Vu & Stewart 2000)

The above model takes into account concrete quality and concrete cover as well as temperature and relative humidity changes. However, this model does not take into account the peaks variations of the corrosion rate with time due to changes in the exposure conditions (Otieno et al. 2011). Vu (2005) developed the Vu and Stewart’s model to take into consideration

of time effects on the corrosion rate. Vu has proposed the following formula to calculate the time-variant corrosion rate (Vu et al. 2005):

$$i_{\text{corr}} = i_{\text{corr}}(1) \times \alpha \times (t - T_i)^\beta \quad \text{where } (t - T_i) \geq 1\text{year} \quad \text{Equation 2.27}$$

where: α And β are constants, where $\alpha=1$, $\beta=0$ for time-invariant and $\alpha=0.85$, $\beta= -0.3$ for time-variant corrosion rate.

When the corrosion is considered to be time-variant, the time to reach the limit crack width will be changed as following (Mullard & Stewart 2009):

$$T_{\text{sp}} = \left[\frac{\beta + 1}{\alpha} \left(t_{\text{sp}} - 1 + \frac{\alpha}{1 + \beta} \right) \right]^{\frac{1}{\beta+1}} \quad \text{Equation 2.28}$$

where: α and β are constants; $\alpha=1$, $\beta=0$ for time-invariant and $\alpha=0.85$, $\beta= -0.3$ for time-variant corrosion rate and t_{sp} is time to reach a limit crack width ω_{lim} for time-invariant corrosion rate.

In 2004, Scott developed a model to predict the corrosion rate based on experimental study on cracked beams with a constant w/c ratio of 0.85 (Scott, 2004). The proposed model can be written as in the following equation:

$$i_{\text{corr}} = \left(1.43 \frac{C_c}{f} + 0.02 \right) e^{\left[\left(\frac{40-x}{20} \right) * 1.2 \left(\frac{C_c}{f} \right)^3 \right]} \quad \text{Equation 2.29}$$

where: $f = 10^{|0.5-s|-0.5+s}$ (where S is the slag concentration expressed as a decimal).

C_c is the 90 day chloride conductivity index value (**ms/cm**) and x is the concrete cover depth (mm).

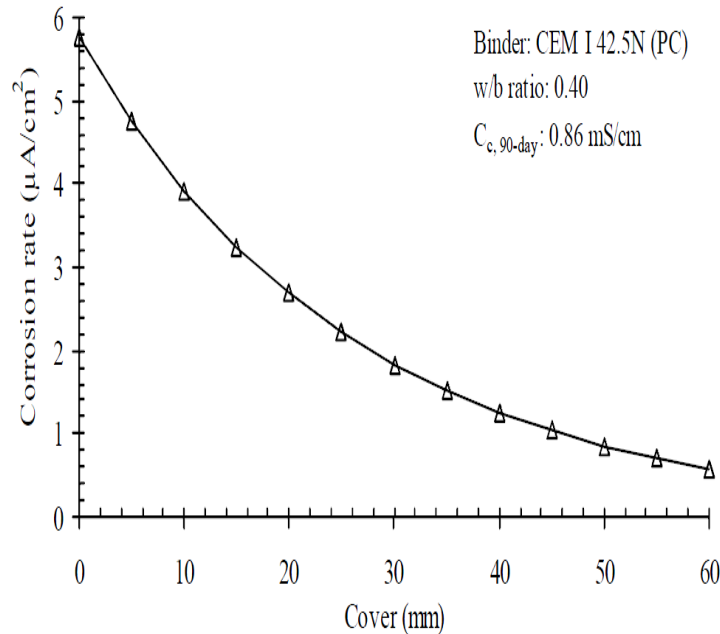


Figure 2.4: Changing of the corrosion rate with concrete cover based on Scott 2004 model

Source: (Scott 2004)

The model was developed based on the cracked specimens and does not take into account the crack width as an input parameter, which means using the models for different scenarios may not be appropriate (Otieno et al. 2011). Also, the equation above does not take w/c ratio as a variable which assumes the corrosion rate does not depend on w/c ratio. Such an assumption is in contrary to what other researchers have found (Otieno et al. 2011).

Liu and Weyer (1998) developed a model to predict the corrosion rate based on experiments was done on uncracked deck slabs with different w/c ratios and concrete covers (Weyers 1998). The developed model was expressed as following:

$$i_{\text{coor}} = 102.47 + 10.09 \ln(1.69cl) - 39038.96(T^{-1}) - 0.0015R_c + 290.91t^{-0.215} \quad \text{Equation 2.30}$$

where:

Cl; is the total chloride content at the steel level(**kg/m³**), **T**; is the temperature at the steel surface (**K**), **Rc**; is the resistivity of the cover concrete (**Ω**) and **t**; is the corrosion time (years).

The model does not take into account the concrete cover as a variable which indicates that the concrete cover does not have an influence on the value of the corrosion rate; which is not correct (Otieno et al. 2011).

2.1.6 Reduction of Nominal Moment Strength Due to Corrosion

It is known that the corrosion of reinforcement and/or spalling of the concrete cover may result in the loss of strength, by reducing the area of steel bar or the bond, as well as serviceability (Rosowsky 1998). Corrosion of steel bars will lead to moment strength reduction as the reinforcement bar cross-sectional area gets smaller. A probabilistic prediction of rebar area reduction was investigated by Mirza and MacGregor (1983), which has shown that about 70% of rebar area will be lost due to corrosion in 20 years of use. Consequently, the nominal moment strength has been reduced by 50%.

Different models have been proposed to estimate the reduction in the steel bars. All of the suggested models can be divided into two common categories: uniform corrosion models and pitting corrosion models. The uniform corrosion model assumes that the geometrical cross-section of the corroded rebars will stay the same as a circular cross-section. Therefore, the surface area and the diameter of the reinforcement steel only will reduce with time (Vu & Stewart 2000). According to this model the changing in the diameter of the steel reinforcement

depends on the current corrosion rate i_{corr} and the corrosion initiation time t_0 as following (Vu & Stewart 2000)

$$\mathbf{D}(t) = \mathbf{D}_i - \gamma * i_{\text{corr}} * (t - t_0) \quad \text{Equation 2.31}$$

where: $\mathbf{D}(t)$ is the diameter of rebar as a function of time, and \mathbf{D}_i , is the original diameter of rebar, t_0 , is the corrosion initiation time and γ , is a factor to change the average corrosion densities to average penetration rates.

Based on the earlier equation, Oh et al. (2007) have employed the uniform corrosion model to predict the reduction in the reinforcement bars. The study estimates that the factor to change the average corrosion densities to average penetration rates equals to **0.023**. Therefore, equation (2.31) can be written as follows (Oh et al. 2007).

$$\mathbf{A}(t) = \left\{ \begin{array}{ll} \mathbf{nD}_i^2 \frac{\pi}{4} & \text{for } t \leq t_0 \\ \mathbf{nD}_t^2 \frac{\pi}{4} & \text{for } t_0 < t < t_0 + \frac{D_i}{0.023i_{\text{corr}}} \\ 0 & \text{for } t \geq t_0 + \frac{D_i}{0.023i_{\text{corr}}} \end{array} \right\} \quad \text{Equation 2.32}$$

Accordingly, Eq. (2.31) can be written as follows (Oh et al. 2007):

$$\mathbf{D}(t) = \mathbf{D}_i - \mathbf{0.023} * i_{\text{corr}} * (t - t_0) \quad \text{Equation 2.33}$$

Pitting corrosion models have been introduced in order to take into consideration the effect of the localized nature of chloride induced (Baboian, 2005). Pitting corrosion can cause a significant reduction in the cross section of the reinforcement bars (Stewart & Al-Harthy 2008).

Val has proposed that changing in the area of the bars can be calculated as follows (Stewart & Al-Harthy 2008):

$$A(t) = \begin{cases} A_1 + A_2 & \text{for } \rho(t) \leq \frac{D_0}{\sqrt{2}} \\ D_0^2 \frac{\pi}{4} - A_1 + A_2 & \text{for } \frac{D_0}{\sqrt{2}} < \rho(t) \leq D_0 \\ D_0^2 \frac{\pi}{4} & \text{for } \rho(t) \geq D_0 \end{cases} \quad \text{Equation 2.34}$$

where:

$$A_1 = 0.5 \left[\phi_1 \left(\frac{D_0}{2} \right)^2 - b \left| \frac{D_0}{2} - \frac{\rho(t)^2}{2} \right| \right] \quad \text{Equation 2.35}$$

$$A_2 = 0.5 \left[\phi_2 \rho(t)^2 - \frac{b * \rho(t)^2}{D_0} \right] \quad \text{Equation 2.36}$$

$$b = 2 \rho(t) \sqrt{1 - \left(\frac{\rho(t)}{D_0} \right)^2} \quad \text{Equation 2.37}$$

$$\phi_1 = 2 * \arcsin\left(\frac{b}{D_0}\right) \quad \text{Equation 2.38}$$

$$\phi_2 = 2 * \arcsin\left(\frac{b}{2\rho(t)}\right) \quad \text{Equation 2.39}$$

$$\rho(t) = 0.0116 i_{\text{corr}} * R_c \quad \text{Equation 2.40}$$

where:

i_{corr} = the current corrosion rate ($\mu\text{A}/\text{cm}^2$ and t is the time since corrosion initiation (years).

Finally, the nominal moment strength can be calculated from the basic flexural strength equation as follows:

$$\mathbf{M_n} = (\mathbf{A_s} - \mathbf{A'_s}) \mathbf{f_y} \left(\mathbf{d} - \frac{\mathbf{a}}{2} \right) + \mathbf{A'_s} \mathbf{f_y} (\mathbf{d} - \mathbf{d'}) \quad \mathbf{Equation\ 2.41}$$

$$\mathbf{a} = \frac{(\mathbf{A_s} - \mathbf{A'_s}) \mathbf{f_y}}{\mathbf{0.85f'_c b}} \quad \mathbf{Equation\ 2.42}$$

2.2 Deterioration Mechanism in RC Decks

Deterioration could occur due to shrinkage, vehicle loads and corrosion. Concrete needs to be able to freely shrink as it dries but this process cannot be done in RC decks due to the restraint that comes from the longitudinal girders (Oh et al. 2007)The restrained shrinkage will increase the elastic strain in the concrete decks. Also, due to the dynamic loads from vehicles, further tensile stresses will be developed in the concrete decks (Oh et al. 2007). The resultant tensile stresses from both shrinkage and traffic load will lead the concrete to crack. First, transverse cracks will occur in the deck making the deck to work as a one-way beam which will fail by the further application of traffic loads (Oh et al. 2007).

Deterioration mechanism due to chloride attacks depends on where it occurs when water and oxygen are available. First, chloride ions penetrate through concrete cover with a rate depending on the quality of the concrete as well as the environmental conditions. According to Neville (1996), in order to protect the steel bars that are used as reinforcement in concrete from corrosion, a thin passive layer of oxide is used. However, that passive layer gets destroyed when the chloride content reaches a threshold value. After the passive layer has been removed, corrosion initiates when oxygen and water exist. Rust layer will be formed around steel bars.

Such a rust layer (ferrous hydroxide) will expand the outer surface of steel due to its large size which will increase the internal stresses in the concrete ending up with longitudinal cracks. These cracks will propagate leading to concrete spalling.

2.3 Bridge Deck Damage Assessment

2.3.1 Introduction:

Bridges are in need of repair and maintenance due to the damage from repetitive loads, such as fatigue. Fatigue occurs when the structure is subjected to cycles of loading and unloading. Although, the cyclic loadings may not cause stress exceeding the extreme stress limit of the material, they will lead to crack formation, propagation and eventually fracture (Thun, 2006). In highway bridges, the bridge decks are considered as the most fatigued element of the structure, because they are directly exposed to both traffic loads and environmental attacks. It has been found that deck slabs experience significant fatigue loadings by moving wheels with a high number of load cycles, such as more than 100 million over the service life of a bridge. As pointed out by Schläfli & Brühwiler (1998), despite the significance on deck fatigue, reinforced concrete deck slabs are commonly not designed for fatigue (Schläfli & Brühwiler 1998).

Laboratory fatigue tests are usually carried on either cracked or uncracked smooth bars specimens (High-Cycle Fatigue (HCF) Testing). Materials, based on the fatigue endurance limits, are divided into three types: low-cycle fatigue, high-cycle fatigue and super-high cycle fatigue. Low-cycle fatigue (LCF) is when a material under a fatigue test endures a small number of load cycles, typically when the number of load cycles to failure is less than 10^3 . High-cycle fatigue (HCF) is when the fatigue test lasts longer than 10^3 number of load cycles (see Figure 2.5). The third kind of fatigue limits, which is the Super-high cycle fatigue, is not common type and its limit is 10^7 number of load cycles (Thun, 2006). Highway and railway bridges are

considered as high-cycle fatigue structures because they last longer than 10^3 number of load cycles.

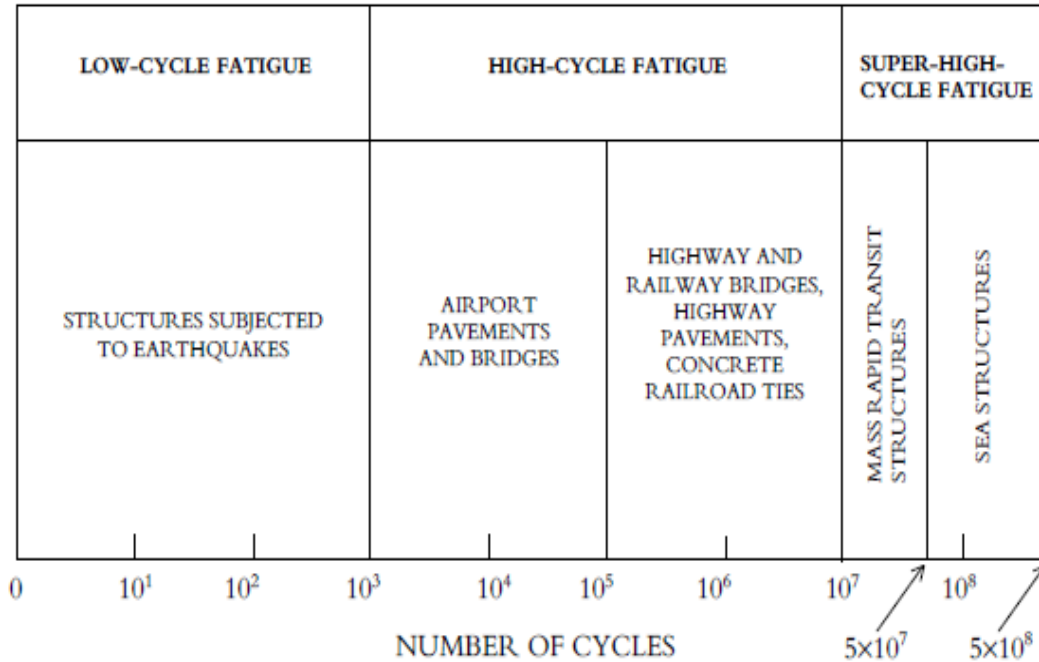


Figure 2.5: Fatigue category based on number of cycles to failure (Thun 2006).

2.3.2 S-N Curves Approach:

Fatigue occurs when a material is subjected to a number of repeated cycles of loading and unloading. Consequently, micro-cracks will initiate at the deck surface. Further application of the traffic loads will increase the size of those cracks ending up with suddenly fracture. Therefore, any fatigue analysis approach has to take into consideration both the stress amplitudes and the number of stress cycles (Sugira & Kunitomo 2008).

Despite being proposed long time ago, one of the most effective and traditional approaches in analyzing fatigue is the S-N curves approach. The S-N curves describe the relationship between stress amplitude and the number of load cycles. Stress ranges and load cycles are plotted in log-log scales, where the vertical scale is for stress amplitudes and the

horizontal represents the number of load cycles (see Figure 2.6). It is clear that when the stress level decreases the number of load cycles that a material can endure increases. The S-N curves are obtained from lab tests by applying constant stresses amplitudes on specimens with counting the applied stress cycles until failure occurs (Maymon 1998). To obtain the number of stress cycles a type of material can endure by using the S-N curves, people just read the value of number of stress cycles corresponding to the constant stress value. In reality the situation is much more complicated because we have different stress ranges with different number of cycles, so the S-N curves cannot be employed directly. Therefore, we need to estimate the cumulative damage by using one of the cumulative damage theories. The linear cumulative damage theory or Palmgren-Miner Rule can be used.

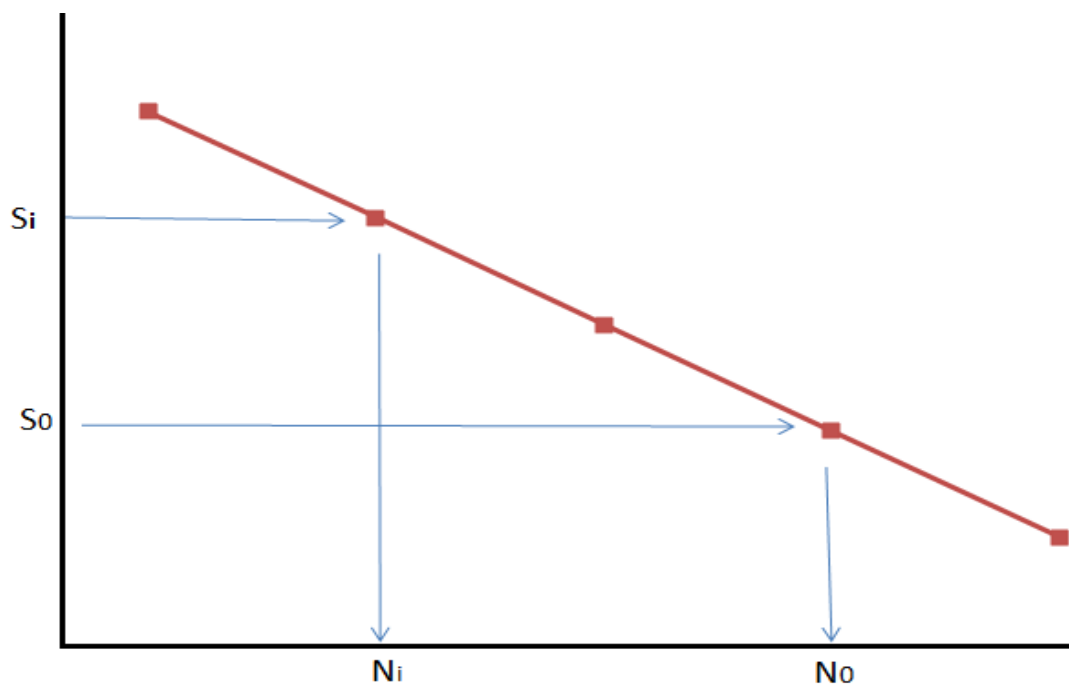


Figure 2.6: Typical S-N Curves

2.3.3 Palmgren-Miner's Rule:

If there is a constant value of loading, the number of load cycles up to failure will be directly obtained from the S-N curves of the material. The material will be considered failed in terms of fatigue when the number of the applied load cycles exceeds the number of load cycles obtained from S-N curves representing the number of load cycles a material can endure. However, in reality the situation is usually more complicated, because we have stress ranges with different amplitudes from load cycles to another, suggesting being stochastic in magnitude. In this case, we must adopt a cumulative hypothesis to assess fatigue damage due to the load variations.

One of the most adopted hypotheses is the Palmgren-Miner's Rule or the linear fatigue damage accumulator theory (Siemes 1982). The Palmgren-Miner's Rule or the linear fatigue damage accumulator theory was first introduced by Palmgren in 1924 and developed by Miner in 1945 (Thun 2006). This method suggests that failure will occur when the number of N_i for non-varying stress range with regard to the stress range $\Delta\sigma_i$ reaches the number of cycles the material can take. Each stress range of n_i cycles may contribute to the failure by n_i/N_i . The fatigue failure under varying loads may occur when the summation of contributions from varying stress ranges reaches to damage index D (Sugira & Kunitomo 2008). Palmgren-Miner's Rule can be written as follows:

$$\sum_{i=1}^n \frac{n_i}{N_i} = D \quad \text{Equation 2.43}$$

where: n_i = the number of applied load cycles causing a certain stress level.

N_i = the corresponding number of load cycles at which stress level S_i leads to failure.

Although this rule is considered as non-conservative tool because it assumes that the damage will be accumulated linearly due to each loading cycles, it is still the most popular method to accumulate the total fatigue damage.

2.3.4 Rainflow Cycles Counting Method

The response time history, either in terms of stress or strain, is irregular with time which means we have stress time history with different peaks and valleys amplitudes. Therefore, we need to employ a cycle counting method to determine the number of stress cycles which have been absorbed by the structure under dynamic loads. There are many different methods which have been introduced to count stress cycles, like Level-Crossing Counting, Peak Counting, Simple-Range Counting and Rainflow counting method (American Society for Testing and Materials 2011). Among all these, the Rainflow cycles counting method is considered to be the best method as compared to the other methods in terms of simplicity, accuracy and time consuming (Socie 1982).

Rainflow cycles counting method theory's depends on the hysteresis loops in the stress-strain behavior (Socie 1982), as shown in Fig. 2.7. As the figure illustrates, the strain will increase linearly from point A to point B, and when the load is removed at point B the strain will decrease until point C. When the member is reloaded the strain will increase linearly from point C to point D crossing its previous strain position before removing the load (point B). Therefore, all of events where the strain is reduced can be ignored like event BC, DE and FG.

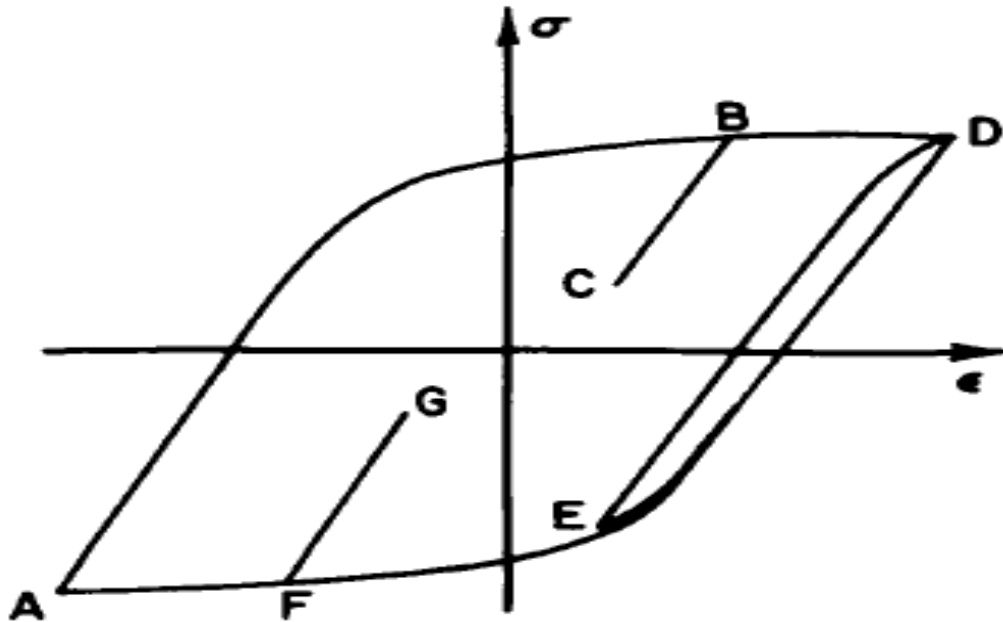


Figure 2.7: Hysteresis loops in the stress-strain behavior (Socie & Downing 1982)

The original name of this method is Pagoda Roofs method based on its graphical representation of the stress time which looks like a series of roofs when it is turned clockwise 90° as in figure (2.8) (Mazzolani 2000). To count the number of half cycles from the stress time history using the Rainflow counting method, the following rules must be followed:

- 1- Rearrange the stress history so it begins with its maximum valley or peak as shown in Figure (2.8) (American Society for Testing and Materials 2011).
- 2- Release a drop from a “valley” or “peak”, and this drop will continue falling until it is stops at a valley or peak that is greater than that it departed from (Mazzolani 2000).
- 3- All drops will continue falling unless there is a path still exists from a previous drop (Mazzolani 2000).

The following example is based on the Figure 2.8 from REF (Mazzolani 2000) :

- 1- Release a drop from point A, this drop will continue falling until it reaches the end of the record and it cannot be stopped because there is no valley is greater than the departure point (point A).
- 2- Another path will start from point B, but it will be stopped at point D. Because point D has a magnitude larger than the magnitude of point B
- 3- Another Rain flow will start from point C, but it will be stopped due to the existing path from point A.
- 4- Rain flows will start from point D and it will continue falling until it reaches the end of the record and it cannot be stopped because there is no valley is greater than the departure point.
- 5- Another rain flow will be released at point E, but it will be stopped at point G since its magnitude is larger than point E magnitude.
- 6- The rain flow that will start from point F will be stopped since it will meet an existing path from point D.
- 7- Another rain flow will be released at point G, but it will be stopped at point A since point A magnitude is larger than point G magnitude.
- 8- The last path will start from point H, but it will be stopped since it will meet an existing path from point D.

The results of this example are shown in Fig. 2.8.

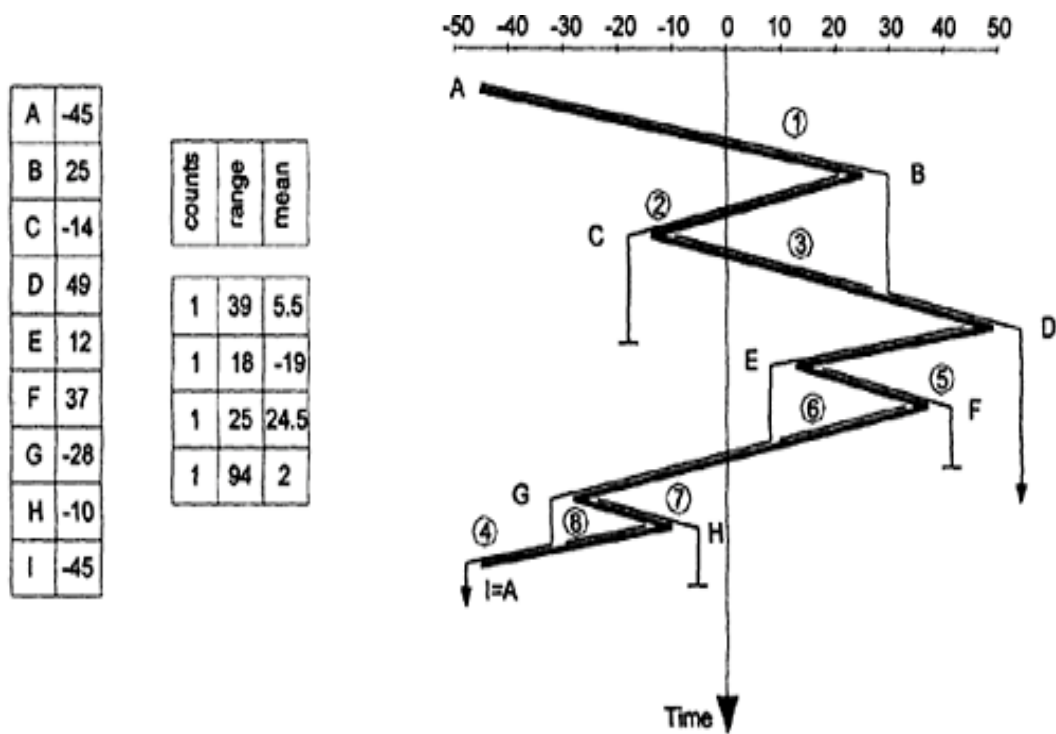


Figure 2.8: Example of Rainflow cycles method (Mazzolani 2000)

Rainflow method is used herein to decompose the stress time history into discrete stress cycles in order to assess the fatigue life.

ASTM (1985) has defined the rules of this method as follows: Let X denote range under consideration; Y, previous range adjacent to X; and S, starting point in the history.

- (1) Read next peak or valley. If out of data, go to Step 6.
- (2) If there are less than three points, go to Step 1. Form ranges X and Y using the three most recent peaks and valleys that have not been discarded.
- (3) Compare the absolute values of ranges X and Y.
 - (a) If $X < Y$, go to Step 1.

(b) If $X \geq Y$, go to Step 4.

(4) If range Y contains the starting point S, go to Step 5; otherwise, count range Y as one cycle; discard the peak and valley of Y; and go to Step 2.

(5) Count range Y as one-half cycle; discard the first point (peak or valley) in range Y; move the starting point to the second point in range Y; and go to Step 2.

(4) If range Y contains the starting point S, go to Step 5; otherwise, count range Y as one cycle; discard the peak and valley of Y; and go to Step 2.

(5) Count range Y as one-half cycle; discard the first point (peak or valley) in range Y; move the starting point to the second point in range Y; and go to Step 2.

(6) Count each range that has not been previously counted as one-half cycle.

The process of this method is described with the following demonstration (ASTM 1985)(Fig. 2.9):

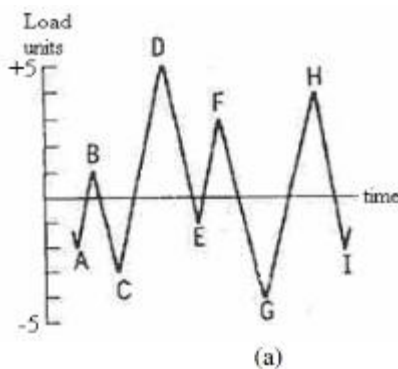


Figure 2.9(a): Example of Rainflow cycles method (ASTM 1985)

(1) $S = A$; $Y = |A-B|$; $X = |B-C|$; $X > Y$. Y contains S , that is, point A . Count $|A-B|$ as one-half cycle and discard point A ; $S = B$ (See Fig. 2.9 (b)).

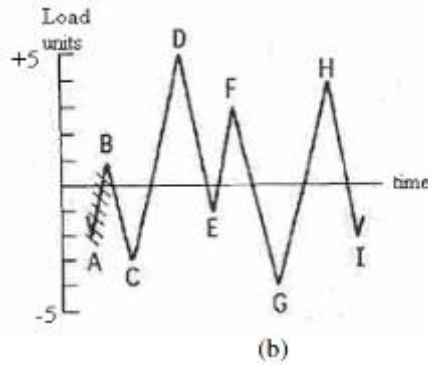


Figure 2.9(b): Example of Rainflow cycles method (ASTM, 1985)

(2) $Y = |B-C|$; $X = |C-D|$; $X > Y$. Y contains S , that is, point B . Count $|B-C|$ as one-half cycle and discard point B ; $S = C$ (See Fig. 2.9(c)).

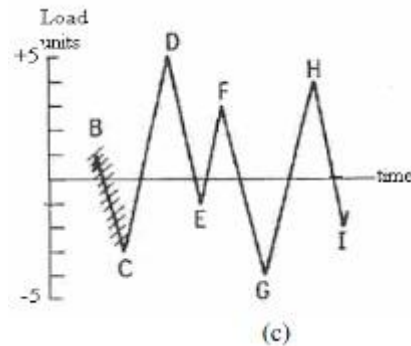


Figure 2.9(c): Example of Rainflow cycles method (ASTM 1985)

(3) $Y = |C-D|$; $X = |D-E|$; $X < Y$.

(4) $Y = |D-E|$; $X = |E-F|$; $X < Y$.

(5) $Y = |E-F|$; $X = |F-G|$; $X > Y$. Count $|E-F|$ as one cycle and discard points E and F . (See Fig. 2.9 (d)). Note that a cycle is formed by pairing range $E-F$ and a portion of range $F-G$.)

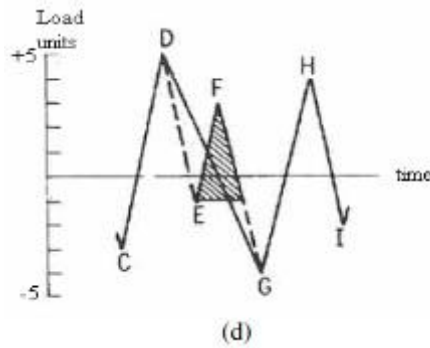


Figure 2.9(d): Example of Rainflow cycles method (ASTM 1985)

(6) $Y = |C-D|$; $X = |D-G|$; $X > Y$; Y contains S , that is, point C . Count $|C-D|$ as one-half cycle and discard point C . $S = D$ See Fig. 2.9(e).

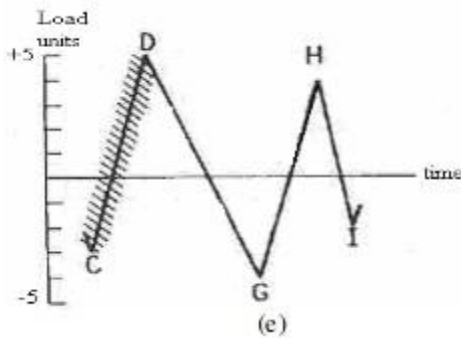


Figure 2.9(e): Example of Rainflow cycles method (ASTM 1985)

(7) $Y = |D-G|$; $X = |G-H|$; $X < Y$.

(8) $Y = |G-H|$; $X = |H-I|$; $X < Y$. End of data

(9) Count $|D-G|$ as one-half cycle, $|G-H|$ as one-half cycle, and $|H-I|$ as one-half cycle (See Fig. 2.9(f)).

(10) End of counting

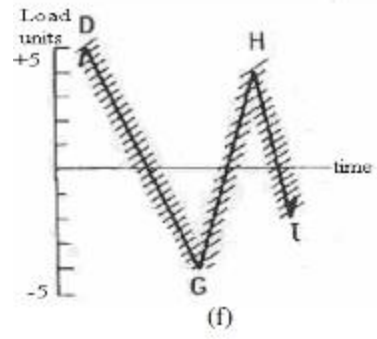


Figure 2.9(f): Example of Rainflow cycles method (ASTM 1985)

Chapter 3: Hybrid Analytical Models and the Prototype Bridge

3.1. The Prototype Bridge

The prototype bridge that was adopted for this investigation is located on 104th AVE, over the I-25 Interstate- Colorado.

3.1.1. Historical Overview

The old bridge was removed in 2008 and the bridge removal consisted of the complete removal of all superstructure and substructure elements including slope pavement, approach slab, wing walls, sleeper slabs and rails. The new bridge was built and designed according to the AASHTO, LRFD Bridge Design Specifications, 4th Edition, 2007, with 2008 Edition Interims. The new bridge is a simple overpass, symmetric, and pre-stressed bridge with two spans and concrete box girders. The 104th bridge is located in Thornton, Colorado, just North of Denver.

3.1.2. Bridge Description and Geometry:

The bridge deck consists of 23 concrete box girders and the bridge was constructed as two simple support spans that were converted to a continuous connection type by the continuous bridge deck. There are two identical spans of 127 ft. curb to curb with no skews, giving a total length of 254 ft and there are five lanes of traffic in each direction with each lane 12 feet wide. This bridge has integrated abutments and the superstructure at the bridge bent is supported by eight 72 in by 48 in elliptical piers. The plan and the elevation views of the bridge are shown as below in Figure 3.1 and Figure 3.2, respectively. Figure 3.3 shows a typical cross section of the bridge modeled.

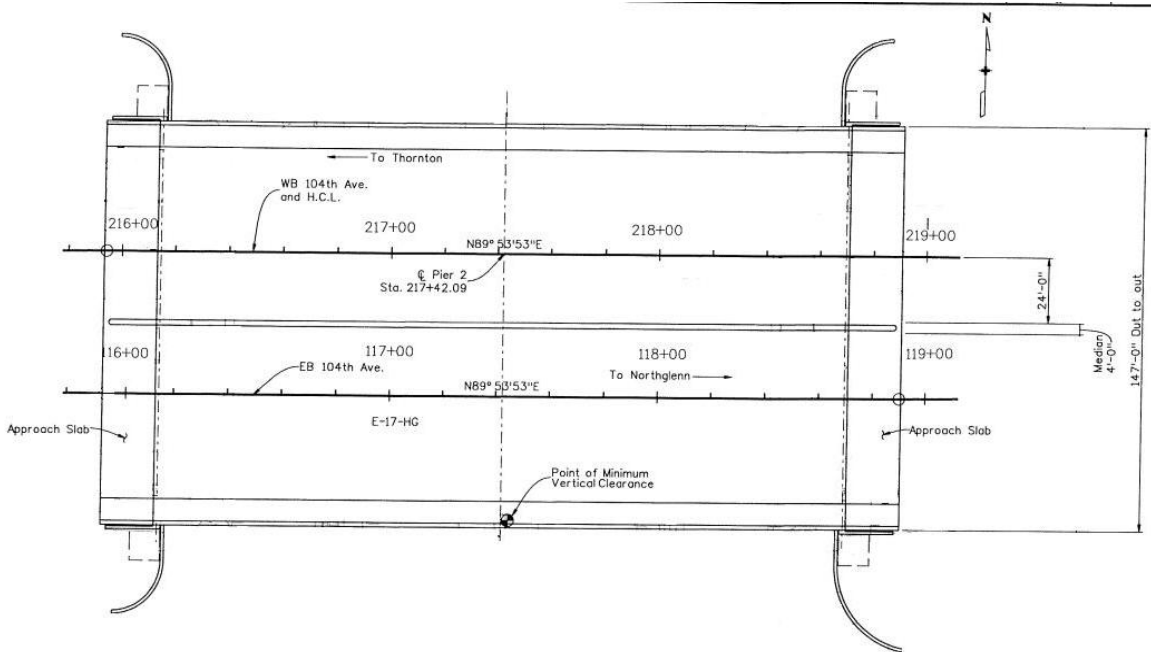


Figure 3.1: The plan view of the 104th bridge

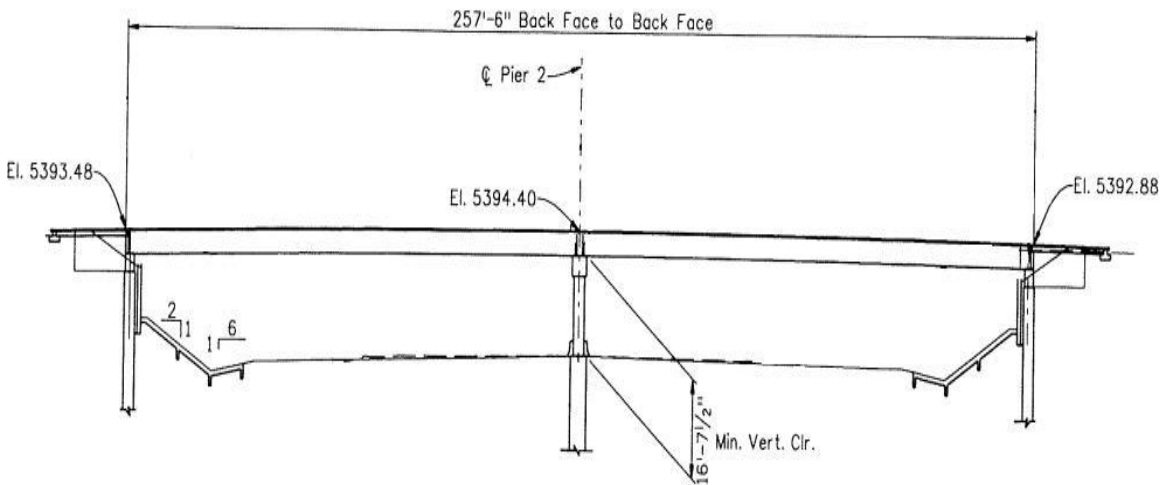


Figure 3.2: The elevation of the 104th bridge

The main superstructure members are made of Class D reinforced concrete ($f_c' = 4,500 \text{ psi}$) and Grad 60 reinforcing steel ($f_y = 60,000 \text{ psi}$). The properties of structural members are listed in Table 3.1. The superstructure consists of two spans were designed of 23 72" \times 46" precast prestressed concrete box girders with minimum cover for the reinforcing steel is 1". The harping point which indicates to a change in the strand geometry and loss in prestress force (critical section) is located at 14 ft. from the center line of the girder (0.39 L from the end). Figure 3.4 shows typical plan, elevation and section in a girder. The superstructure is 147' width out to out and was designed to support ten lanes, five lanes in each direction (three thru lanes and two turn lanes) and each lane is 12' width. Also, there is a 4' median and 8' sidewalk in each direction as illustrated in Figure 3.3. Figure 3.5 gives the detailed section in the approach slab and Figure 3.6 and Figure 3.7 show typical caisson details at abutment and pier. The approach slab is 12' long by 1'-3" thick. The approach slab is made of Class D reinforced concrete ($f_c' = 4,500 \text{ psi}$) and Grad 60 reinforcing steel ($f_y = 60,000 \text{ psi}$).

Table 3.1: The properties of structural members

Bridge Component	Modulus of Elasticity (psi)
Bent Cap	4500
Girder	8500
Deck	4500
Column	4500

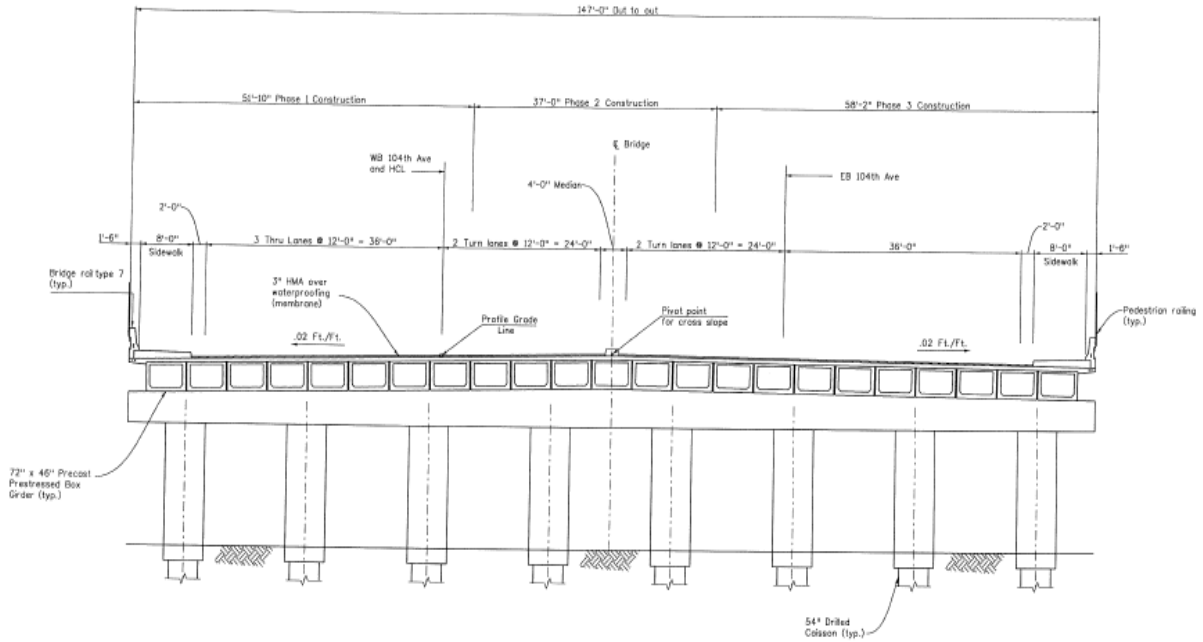


Figure 3.3: Typical Section in the Bridge

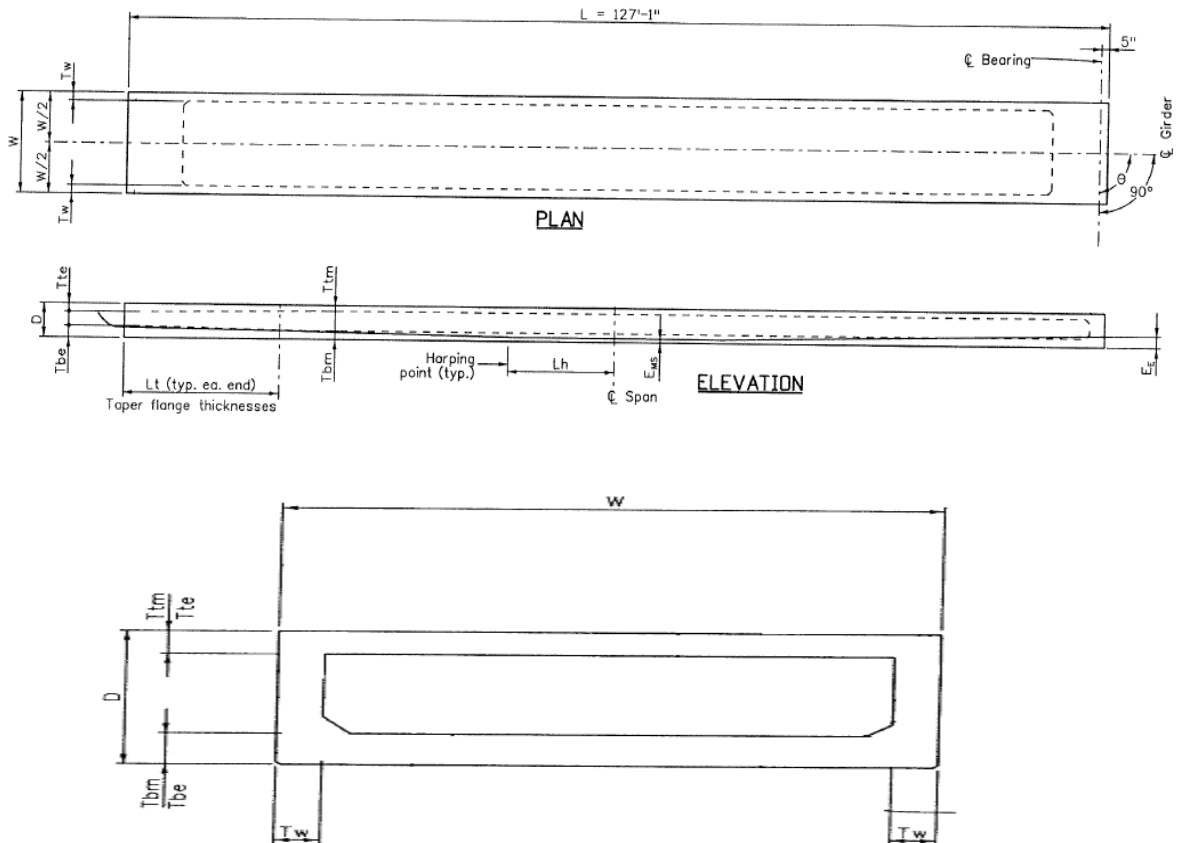


Figure 3.4: Typical elevation, plan and section of the girder

Table 3.2: Girders dimensions

L (ft)	W (in)	D (in)	Tw (in)	Tbm (in)	Ttm (in)	Tbe (in)	Tte (in)	θ (Deg)	L_h (ft)
127 .08	72	46	6	6	4	6	4	90	14
A_s[*] in ²	Debonded Strands (percent)	E_E (in)	E_{ms} (in)	F_j (KIPS)	F_f (KIPS)	f'ci (PSI)	f'c (PSI)	Δ (in)	Predicted camber (in)
13. 888	12.5%	3.25	3.25	2813	2310	6500	8500	-.265	0.91

where: A_s^{*} = minimum area of the prestressing steel.

F_j = jacking force per girder.

F_f = 1 final force per girder after all losses.

f'ci = required concrete strength at release of prestress force.

f'c = required concrete strength at 28 days of age.

L = length of girder along the grade of the girder.

Δ = deflection at centerline of span due to cast-in-place slab, diaphragms, asphalt, curbs, rails, and walks.

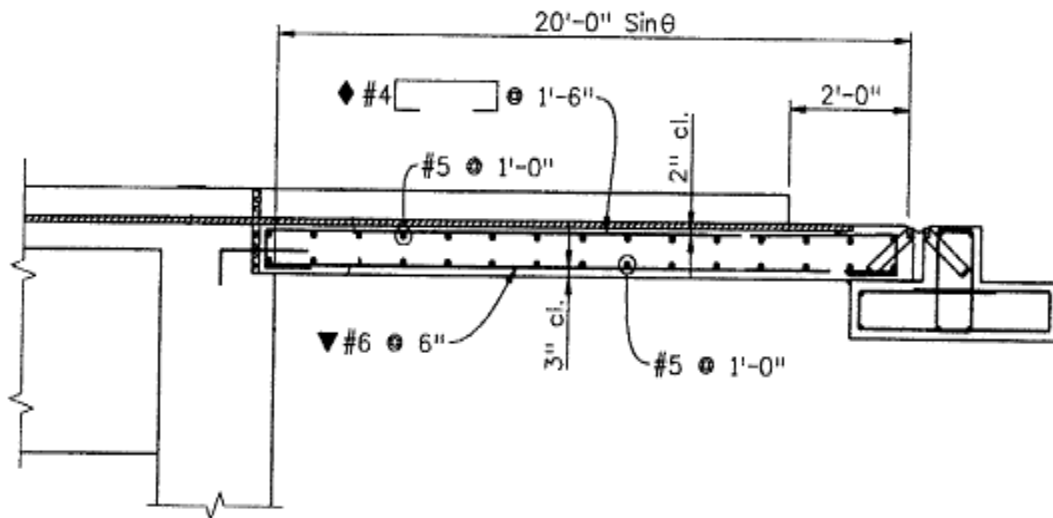


Figure 3.5: Detailed section in approach slab

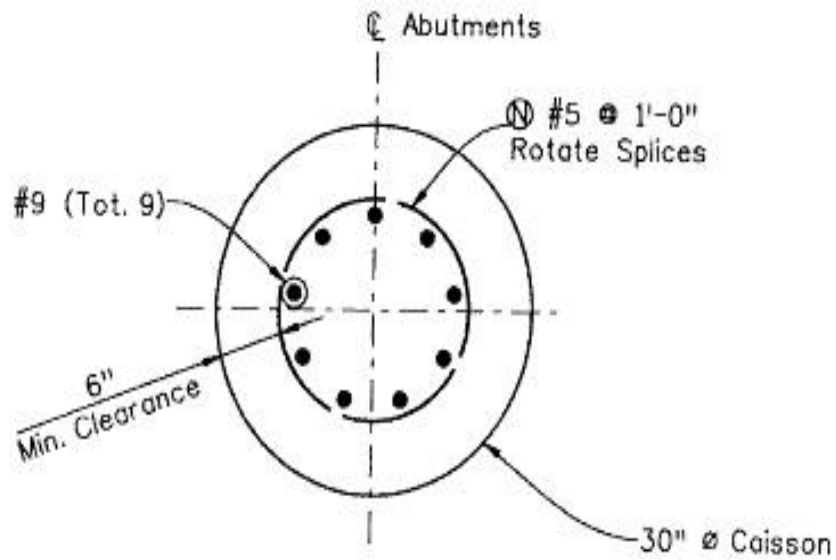


Figure 3.6: Typical caisson detail at abutment

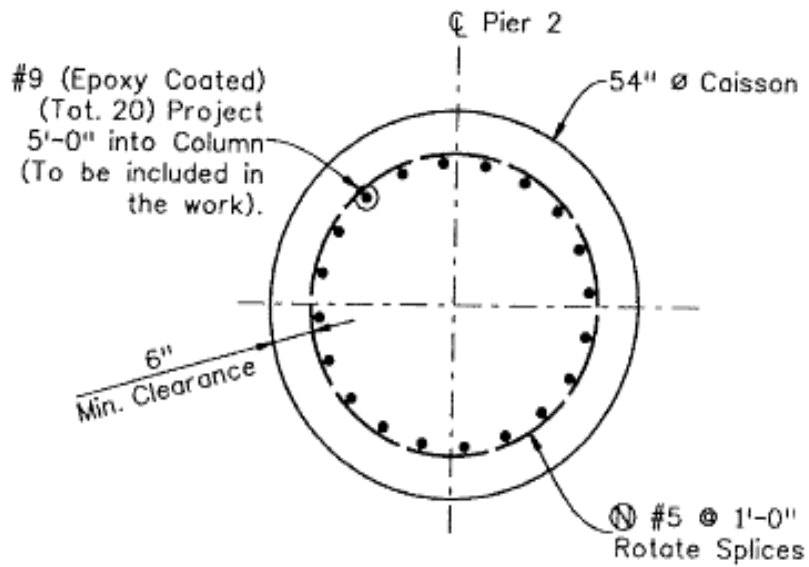


Figure 3.7: Typical caisson detail at pier

3.2 Refined-Scale Finite Element Bridge Model with SAP2000

3.2.1 Introduction:

A refined-scale Finite Element model for the bridge was developed in order to obtain the bridge deck response under dynamic loads. SAP2000 software was employed to establish the finite element model (FEM). The dimensions and material properties which were used in this model follow those of the prototype bridge. The FEM-based model used in the present study was modified from the one developed by another MS graduate student working on the same bridge on other research topics.

3.2.2 Superstructure:

The deck slab was modeled using shell elements and the girders were modeled as straight frame members between nodes. Due to flexural behavior of the bridge decks under repeated loading, the bridge deck was modeled with plates/shell elements. Four nodes shell elements were used to model the deck, also at each node of the shell elements, all of the six degrees of freedom have been activated: translations and rotation in the global X, Y, and Z directions. Figure 3.8 shows 3D view of the finite element model of the bridge. As long as the deck thickness is less than 1/5 to 1/10 of the span, the transverse shear deformation in plate-bending behavior is neglected. Therefore, using thin shell element formulation is more appropriate for our bridge model than using thick shell element formulation. In order to obtain more accurate results from the analysis, all of the plates have been automatically meshed into 4×4 sub-elements plates. Due to the fact that any geometric shape can be easily modeled with quadrilateral shapes, the use of triangular elements has been avoided in the bridge deck modeling. Figure 3.9 shows the quadrilateral elements used to model the bridge deck. Figure 3.10 shows Cross section of the girder.

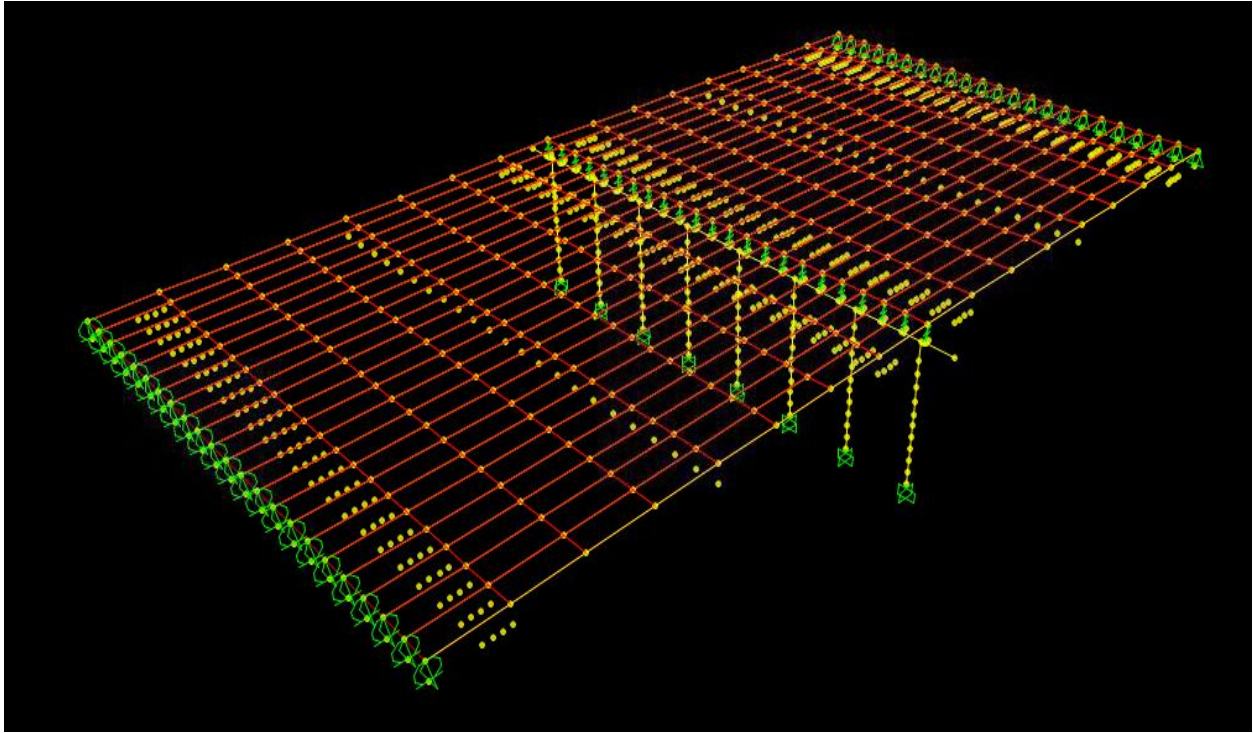


Figure 3.8: 3D view of the finite element model of the bridge

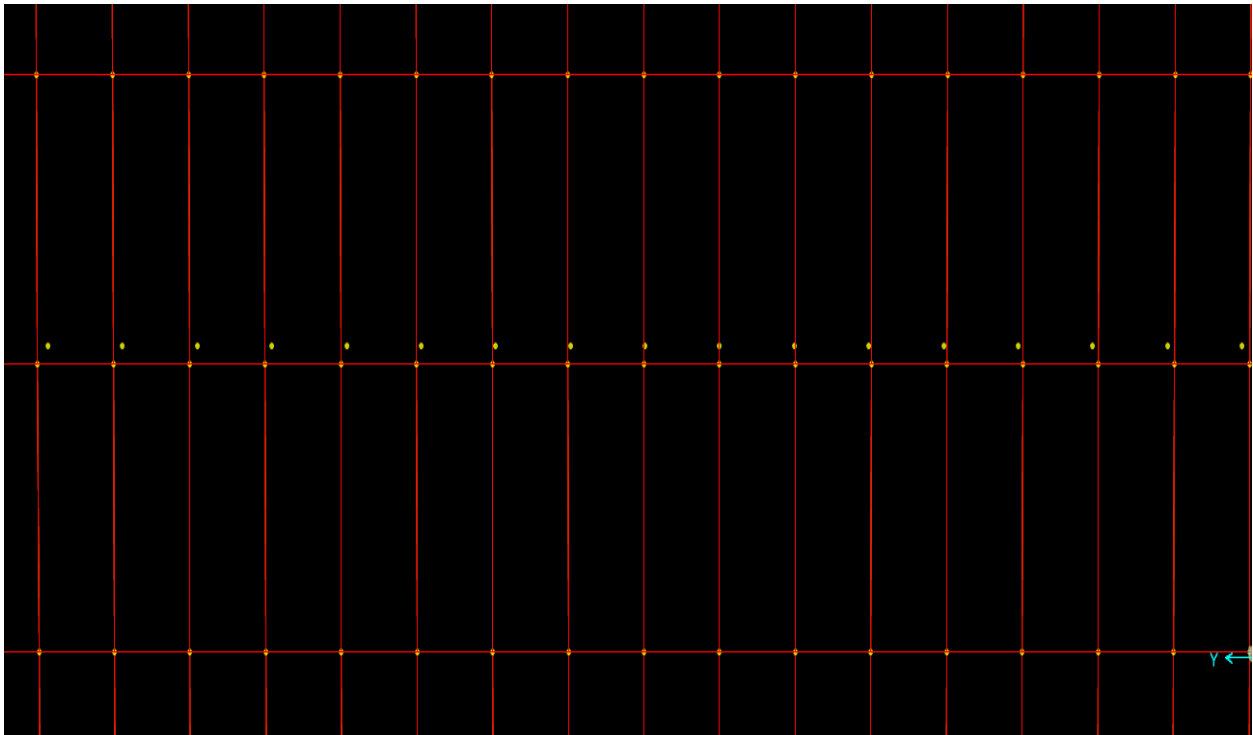


Figure 3.9: Shell elements plates were used to model the bridge deck

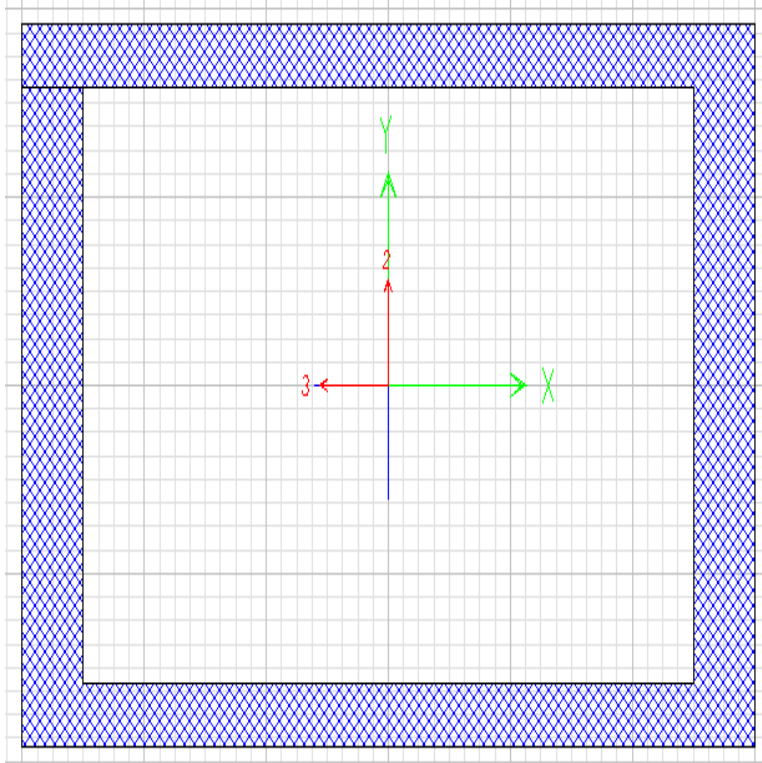


Figure 3.10: Cross section in the girder modeled

3.2.3 Bent Cap:

At the middle of the bridge, there is a bent cap which is a horizontal member (beam) resting on the top of columns. The bent cap is used to provide a support to the longitudinal beams (girders) that in turn support the roadway deck. The bent cap was modeled using two nodes straight frame finite elements with cross-section properties similar to the actual bent cap (Figure 3.11). At each node of the straight frame finite element, all of the six degrees of freedom have been activated. At the location of the bent cap, rigid links were used in order to connect the bent cap (horizontal beam) with the girders (longitudinal beams).

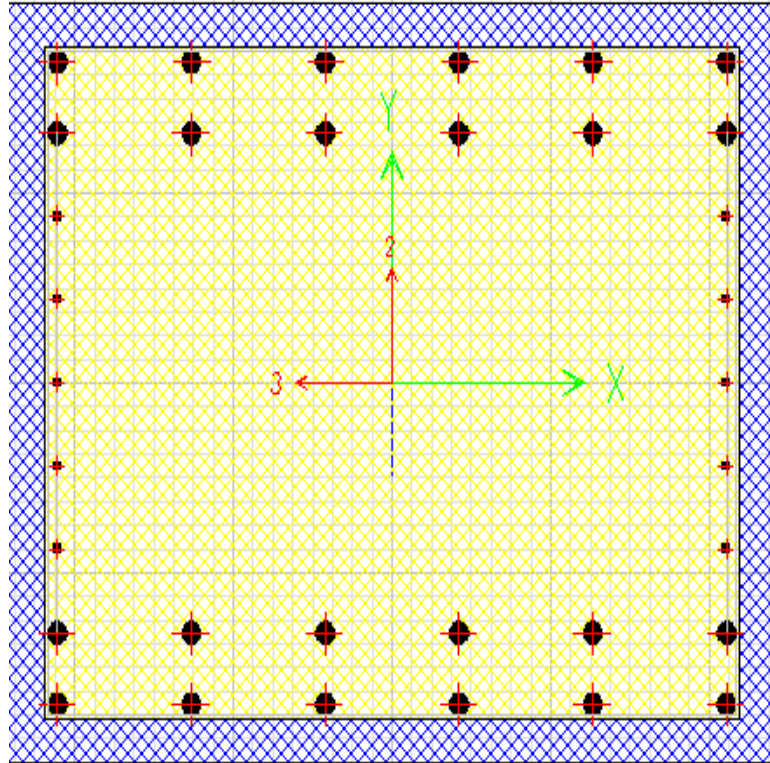


Figure 3.11: Cross section of the bent cap

3.2.4 Piers:

The substructure of the bridge consists of eight piers with the bent cap. The piers were modeled also using two nodes straight finite elements. Table 3.3 shows different components of the bridge which were modeled with various elements. Figure 3.12 depicts the cross section in the caisson modeled. Figure 3.13 shows the cross section in the abutment modeled. Figure 3.14 shows the cross section in the column modeled.

Table 3.3: Different types of modeling were used for different components of the bridge.

Bridge Component	Model
Bent Cap	Straight Frame
Girder	Straight Frame
Deck	Shell-Thin Element
Column	Straight Frame

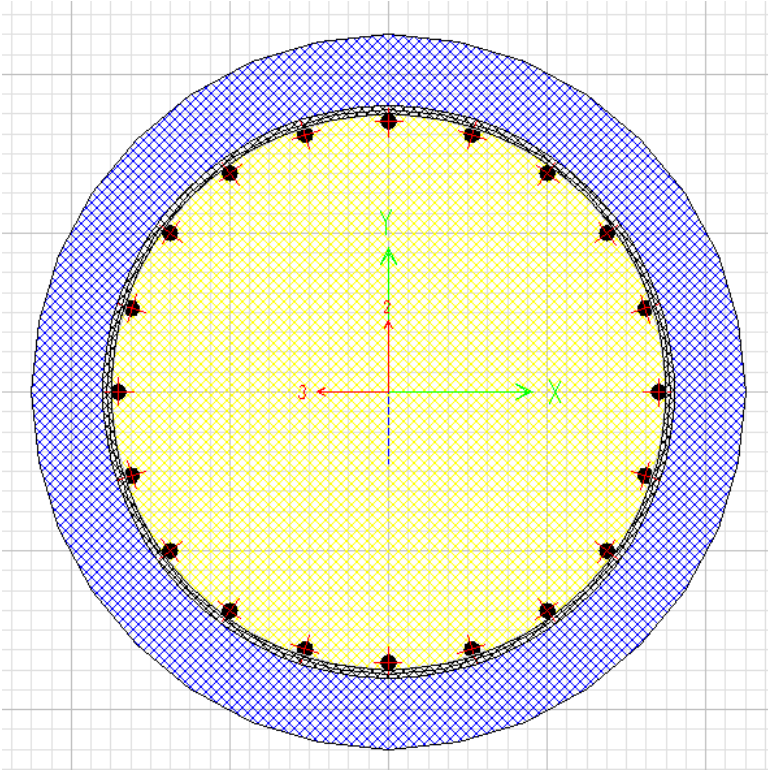


Figure 3.12: Cross section of the caisson modeled

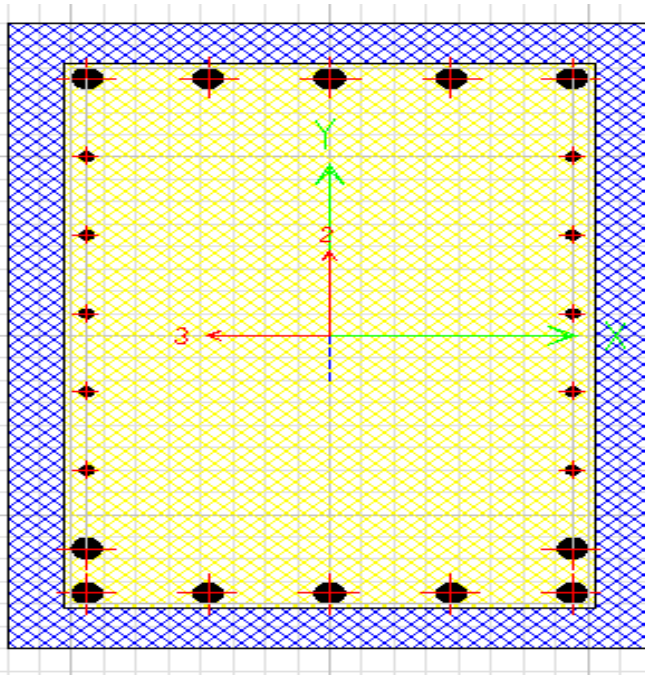


Figure 3.13: Cross section of the abutment modeled

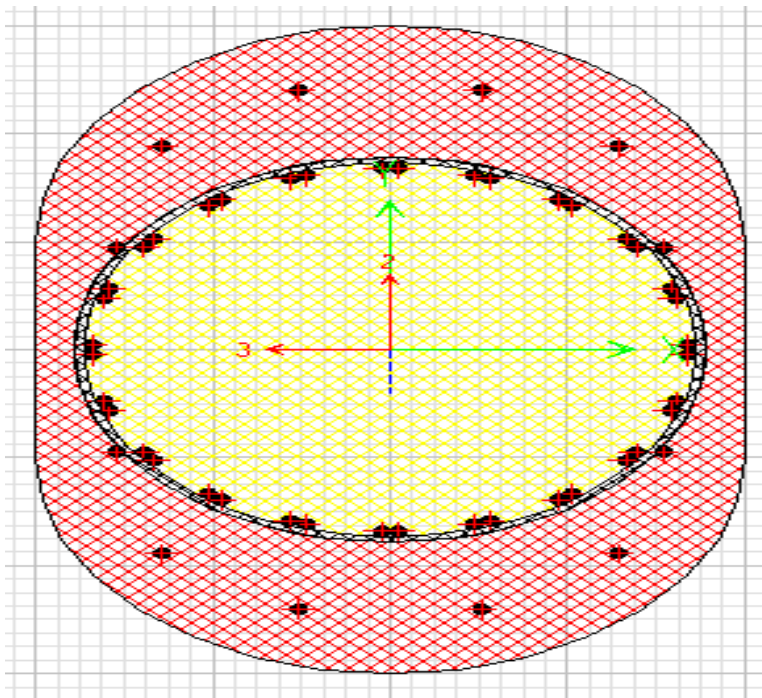


Figure 3.14: Cross section of the column modeled

3.3 Reduced-DOF Bridge/Vehicle/Roughness Model

3.3.1 Reduced-DOF Bridge Model

From the refined-scale FEM model described in Section 3.2, modal analysis is conducted to identify the primary frequencies and mode shapes. A few top modes are typically selected to form a reduced-DOF bridge model in typical dynamic analysis of bridges. The dynamic equations of the reduced-DOF bridge model are then established as:

$$[\mathbf{M}_b] [\ddot{\mathbf{d}}_b] + [\mathbf{C}_b] [\dot{\mathbf{d}}_b] + [\mathbf{K}_b] [\mathbf{d}_b] = [\mathbf{F}_b] \quad \text{Equation 3.1}$$

where $[\mathbf{M}_b]$ the mass matrix, $[\mathbf{C}_b]$ damping matrix, and $[\mathbf{K}_b]$ stiffness matrix of the bridge; $[\mathbf{F}_b]$ is the vector of wheel-bridge contact forces acting on the bridge.

3.3.2 Vehicle and Bridge Models:

The vehicle is modeled as a multi-body system with eleven independent degrees of freedom (DOF) as shown in Figure 3.15. The model consists of several rigid bodies connected by axle mass blocks, springs and damping devices (Cai & Chen 2004). The tires and suspension systems are ideally modeled as linear elastic spring elements and dashpots. The dynamic of the vehicle model is derived based on the following matrix form:

$$[\mathbf{M}_v] [\ddot{\mathbf{d}}_v] + [\mathbf{C}_v] [\dot{\mathbf{d}}_v] + [\mathbf{K}_v] [\mathbf{d}_v] = [\mathbf{F}_v^G] + [\mathbf{F}_c] \quad \text{Equation 3.2}$$

where $[\mathbf{M}_v]$ is the mass matrix, $[\mathbf{C}_v]$ is the damping matrix, and $[\mathbf{K}_v]$ is the stiffness matrix which are obtained by considering the equilibrium of the forces and moments of the vehicle system; $[\mathbf{d}_v]$ is the displacement vector of vehicle; $[\mathbf{F}_v^G]$ is the self-weight of the vehicle; $[\mathbf{F}_c]$ is the vector of wheel-bridge contact forces acting on the vehicle.

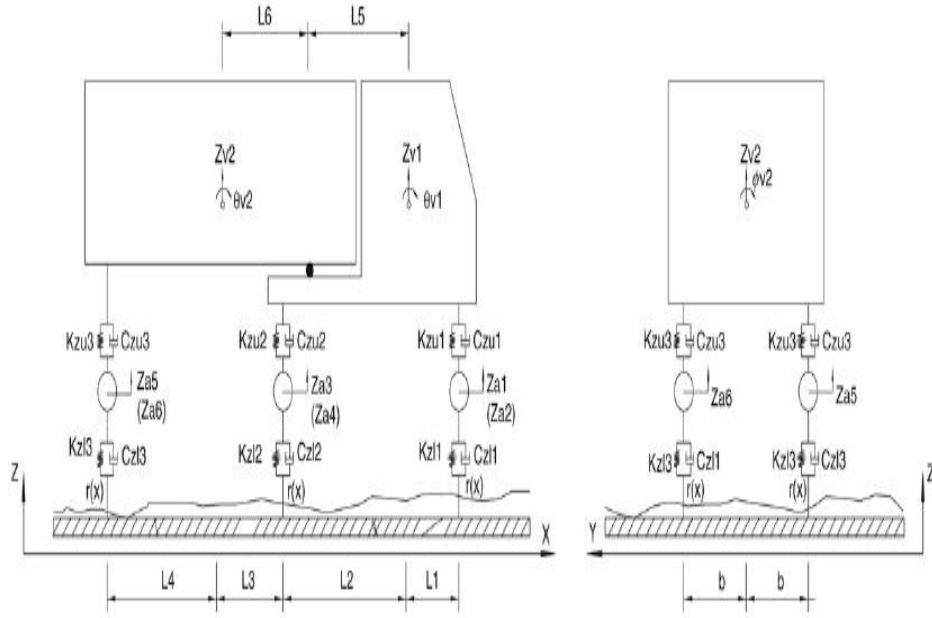


Figure 3.15: Vehicle model

3.3.3 Interaction of Vehicle and Bridge:

The bridge and the moving vehicles interact with each other through the interaction forces i.e. $[\mathbf{F}_b]$ and $[\mathbf{F}_c]$ at points of contacts between the two systems (Shi et al. 2008). In order to calculate the bridge dynamic response, the vectors of wheel-road contact forces acting on the bridge and the vehicle $[\mathbf{F}_b]$ and $[\mathbf{F}_c]$ need to be solved firstly. According to a previous study (Cai & Chen 2004), the contact forces can be stated as a function of deformation of the vehicle's lower spring.

$$[\mathbf{F}_b] = -[\mathbf{F}_c] = [\mathbf{K}_1] [\Delta_1] + [\mathbf{C}_1] [\dot{\Delta}_1] \quad \text{Equation 3.3}$$

where: $[\mathbf{K}_1]$ and $[\mathbf{C}_1]$ are coefficients of vehicle lower spring and damper, and $\Delta 1$ is the deformation of the lower springs of the vehicle which can be calculated from the following equation (Shi et al. 2008):

$$\Delta \mathbf{1} = \mathbf{Z}_a - \mathbf{Z}_b - \mathbf{r}(\mathbf{x}) \quad \text{Equation 3.4}$$

$$\Delta \mathbf{1} = \dot{\mathbf{Z}}_a - \dot{\mathbf{Z}}_b - \dot{\mathbf{r}}(\mathbf{x}) \quad \text{Equation 3.5}$$

where $\dot{\mathbf{r}}(\mathbf{x}) = (\mathbf{dr}(\mathbf{x})/\mathbf{dx}) \cdot (\mathbf{dx}/\mathbf{dt}) = (\mathbf{dr}(\mathbf{x})/\mathbf{dx})$.

By substituting Equations 3.4 and 3.5, into Equation 3.3, the contact force vector between the bridge and the vehicle can be written as

$$[\mathbf{F}_b] = -[\mathbf{F}_c] = [\mathbf{K}_1] [\mathbf{Z}_a - \mathbf{Z}_b - \mathbf{r}(\mathbf{x})] + [\mathbf{C}_1] [\dot{\mathbf{Z}}_a - \dot{\mathbf{Z}}_b - \dot{\mathbf{r}}(\mathbf{x})] \quad \text{Equation 3.6}$$

By substituting Equation 3.6 into Equations 3.1 and 3.2, the final equations of motion for the coupled system are:

$$\begin{bmatrix} \mathbf{M}_b & \\ & \mathbf{M}_v \end{bmatrix} \begin{bmatrix} \ddot{\mathbf{d}}_b \\ \ddot{\mathbf{d}}_v \end{bmatrix} + \begin{bmatrix} \mathbf{C}_b + \mathbf{C}_{bb} & \mathbf{C}_{bv} \\ \mathbf{C}_{vb} & \mathbf{C}_v \end{bmatrix} \begin{bmatrix} \dot{\mathbf{d}}_b \\ \dot{\mathbf{d}}_v \end{bmatrix} + \begin{bmatrix} \mathbf{K}_b + \mathbf{K}_{bb} & \mathbf{K}_{bv} \\ \mathbf{K}_{vb} & \mathbf{K}_v \end{bmatrix} \begin{bmatrix} \mathbf{d}_b \\ \mathbf{d}_v \end{bmatrix} = \begin{bmatrix} \mathbf{F}_b^r \\ \mathbf{F}_v^r + \mathbf{F}_v^G \end{bmatrix} \quad \text{Equation 3.7}$$

where \mathbf{C}_{bb} , \mathbf{C}_{bv} , \mathbf{C}_{vb} , \mathbf{K}_{bb} , \mathbf{K}_{bv} , \mathbf{K}_{vb} , \mathbf{F}_b^r and \mathbf{F}_v^r are additional terms due to dynamic interactions between bridge, vehicle and roughness and the expansion of the contact force. \mathbf{F}_v^G is the gravitational force of vehicle.

During the process of the vehicle moving across the bridge, the contact force vector between the bridge and the vehicle will vary. Accordingly, the additional terms in Equation 3.7 will change with time, which means they are time-dependent. The actual wheel load time history of any moving vehicle through the bridge can be obtained by conducting dynamic interaction

analysis of Eq.3.7. To consider the interaction analysis between a bridge and multiple moving vehicles within stochastic traffic flow, the equivalent wheel loading approach was introduced by (Chen & Cai 2007). Similar procedure to consider the interaction of bridge and stochastic traffic (Chen & Wu 2010) will be followed. More details will be provided in later sections.

3.3.4 Road Surface Roughness Condition:

In order to solve Equations 3.6 and 3.7, the bridge deck roughness profile $r(x)$ needs to be defined. The road surface profile is usually expressed in a random process with a Gaussian probability distribution as:

$$\boldsymbol{\varphi}(\mathbf{n}) = \boldsymbol{\varphi}(\mathbf{n}_0) \left(\frac{\mathbf{n}}{\mathbf{n}_0}\right)^{-2} \quad \text{Equation 3.8}$$

where $\boldsymbol{\varphi}(\mathbf{n})$ = power spectral density function ($\mathbf{m}^2/\mathbf{cycle}/\mathbf{m}$) for the road surface elevation; \mathbf{n} = spatial frequency($\mathbf{cycle}/\mathbf{m}$); \mathbf{n}_0 = discontinuity frequency of $1/ (2\boldsymbol{\pi})(\mathbf{cycle}/\mathbf{m})$; and $\boldsymbol{\varphi}(\mathbf{n}_0)$ = roughness coefficient ($\mathbf{m}^3/\mathbf{cycle}$) whose value is chosen depending on the road condition.

By applying the inverse discrete Fourier transformation, the road roughness profile can be simulated in the space domain as (Wang & Huang 1992).

$$\mathbf{r}(\mathbf{x}) = \sum_{\mathbf{k}=1}^{\mathbf{N}} \sqrt{2\boldsymbol{\varphi}(\mathbf{n}_{\mathbf{k}})\Delta\mathbf{n}} \cos(2\boldsymbol{\pi}\mathbf{n}_{\mathbf{k}}\mathbf{x} + \boldsymbol{\theta}_{\mathbf{k}}) \quad \text{Equation 3.9}$$

where $\boldsymbol{\theta}_{\mathbf{k}}$ = the random phase angle uniformly distributed from 0 to $2\boldsymbol{\pi}$, $\boldsymbol{\varphi}()$ is the power spectral density (PSD) function ($\mathbf{m}^3/\mathbf{cycle}/\mathbf{m}$) for the road surface elevation, $\mathbf{n}_{\mathbf{k}}$ is the wave number ($\mathbf{cycle}/\mathbf{m}$).

3.4 Time History Input of Deck Node Forces from Stochastic Traffic with Dynamic interaction

3.4.1 Equivalent Dynamic Wheel Load Database of Various Traffic Scenarios

When traffic moves on a bridge, the dynamic interaction between the bridge and vehicles needs to be considered in order to obtain the rational estimation of the dynamic response of the bridge ((Xu & Guo 2003); (Cai & Chen 2004)). The dynamic wheel load ratio R (Chen & Cai 2007), defined as the ratio of dynamic wheel load to vehicle gravity, is adopted in this paper to define the time histories of dynamic forces on the bridge due to multiple moving vehicles within traffic flow. The total wheel load for each vehicle in the stochastic traffic flow can be defined as the summation of the dynamic wheel load and the vehicle gravity load, as defined in Eq. (3.10) (Chen & Cai 2007)

$$\mathbf{F}_j(\mathbf{t}) = \left(\mathbf{1} + \mathbf{R}_j(\mathbf{t}) \right) * \mathbf{G}_j(\mathbf{t}) \quad \text{Equation 3.10}$$

where, $\mathbf{R}_j(\mathbf{t})$ is the dynamic wheel load ratio of vehicle j at time t ; $\mathbf{G}_j(\mathbf{t})$ is the gravity of the vehicle j at time t .

The dynamic wheel load is obtained through dynamic interaction analysis with Eq. (3.7) as introduced above (Chen and Cai 2007). Comprehensive numerical analysis has been conducted firstly to quantify the dynamic wheel load for each traffic driving condition, which is defined with a specific vehicle type, driving speed, bridge surface roughness level and driving lane on the bridge. A dynamic wheel load database is therefore developed with the dynamic wheel loads of all the traffic driving conditions.

3.4.2 Stochastic Traffic Flow Simulation

In order to rationally simulate the moving traffic on a bridge, the stochastic traffic flow in this study is simulated with the cellular automaton (CA) traffic simulation model, following the

existing study (Chen & Wu 2011).The CA traffic model is a type of microscopic traffic flow simulation approach, which can generate individual vehicle's behavior in both temporal and spatial domains (Nagel & Schreckenberg 1992).The CA-based traffic flow simulation was performed on a “roadway-bridge-roadway” system to replicate the stochastic traffic flow through the bridge following the approach proposed by Chen and Wu (2011). Accordingly, the number of total vehicles, the instantaneous velocity and the position of each vehicle at any time instant can be identified. The details of the traffic flow simulation including the traffic rules by which the CA model is simulated have been described in several published papers (Chen & Wu 2010); (Chen & Wu 2011), hereby not repeated.

3.4.3 Assemble Cumulative Dynamic Wheel Load from Stochastic Traffic Flow

With the data generated from the CA-based traffic flow simulation, the information of each vehicle within the traffic flow, including the vehicle speed and location at each time step, becomes available. For each time step, the actual wheel load force for each individual vehicle can be extracted from the dynamic wheel load database developed in 3.4.1 based on the instantaneous speed, position and vehicle type as defined in the traffic flow simulation in 3.4.2. The dynamic wheel load for any vehicle will be applied at the same location of the vehicle to represent the actual dynamic impact on the bridge considering dynamic interactions. Repeat the process for all the vehicles remaining on the bridge at a particular time instant, the cumulative wheel loads acting at respective locations on the whole bridge will be obtained for this time instant. Repeat the same process for each time step and finally the time histories of the cumulative wheel loads on the whole bridge will be obtained. The time histories of the equivalent dynamic moving loads are therefore to represent the moving vehicles within the stochastic traffic flow. It is noted that different from traditional moving loads with constant

vehicle gravity force, the equivalent moving wheel loads are equivalent to the actual vehicle dynamic model in the sense that the actual dynamic interactions between the bridge, roughness and vehicle dynamic model have been considered.

3.4.4 Assemble Time-History Input of Bridge Deck Node Forces in Refined SAP Model

In Section 3.4.3, the time histories of moving dynamic wheel loads were generated. These moving loads are applied at the same locations of the respective vehicles within the traffic flow at any time step. In order to apply these loads in the refined-scale SAP model, some conversions are needed to generate the nodal forces on the bridge deck elements of the SAP model.

In this study, at each time step, each dynamic moving wheel load is likely to fall into a specific bridge deck element. Within that element, linear distribution is made in both longitudinal and transverse directions into the four nodes of the bridge deck element. For each node, the nodal forces are accumulated at each time step if multiple vehicles contribute. Continue the process for each time step, and the time histories of the dynamic nodal force inputs for all the bridge deck nodes can be finally generated. The whole process of hybrid dynamic analytical model (i.e. refined-scale FEM model with SAP2000 and reduced-DOF model to quantify traffic loads) is summarized in Fig. 3.16.

3.5 Nonlinear Time Domain Dynamic Analysis with Refined-Scale SAP Model

Time-domain dynamic analysis of the refined-scale FEM bridge dynamic analytical model developed with SAP2000 will be conducted. By taking advantage of the built-in functions of nonlinearity, time-history analysis and time solving algorithms, the time-history analysis is conducted with appropriate bridge deck nodal inputs as defined in Section 3.4. The rebar of the

bridge deck is modeled with appropriate dimension to reflect the corresponding level of corrosion. After the time-history analysis is finished, the detailed time-history response of all the nodes and elements of the bridge can be obtained. The dynamic performance of any bridge component, such as bridge girder, pier and deck can all be assessed. Within the scope of this study, the dynamic response at the bottom layer of the bridge deck will be further analyzed in following chapters to particularly assess fatigue damage of bridge deck due to the joint impact from traffic and corrosion.

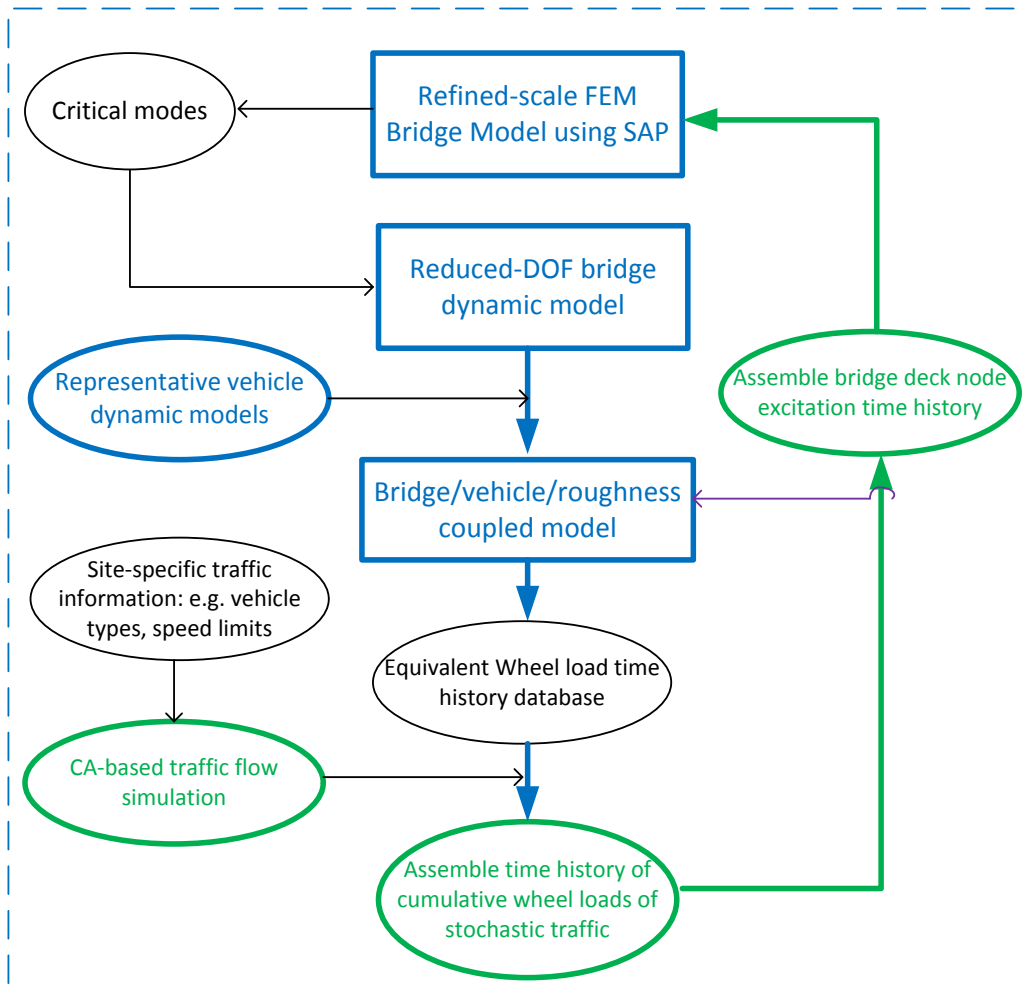


Figure 3.16: Hybrid bridge dynamic analytical model

Chapter 4: Time-progressive Dynamic Analysis and Fatigue Assessment Methodology of Bridge Deck Subjected to Traffic and Corrosion

4.1 Scenario-Based Fatigue Damage Model for a Typical Year

Wu et al. (2012) has conducted the time-progressive fatigue assessment of long-span bridges subjected to wind and stochastic traffic flow based on representative scenarios. Such a procedure developed by Wu et al. (2012) is followed in this study with two major steps:

- 1- Categorizing the representative scenarios of roughness, corrosion and traffic conditions.
- 2- Calculating fatigue damage factor for each typical year in a time-progressive way.

4.1.1 Categorization of the Representative Scenarios:

In order to make this study to cover more realistic performance of bridges, a comprehensive coverage of all of possible roughness, corrosion and traffic scenarios must be investigated. Then all of possible representative combined scenarios of roughness, traffic and corrosion must be defined first.

4.1.1.1 Roughness Representative Scenarios.

According to the ISO guideline (International Standard Organization 1995), road roughness condition is classified based on the Road-Roughness Coefficient (RRC) into five major categories which are Very Good, Good, Average, Poor and Very Poor. Table 4.1 shows the Road-Roughness Coefficient (RRC) values for road-roughness coefficient. In this study, it is assumed that the wearing surface of the bridge deck may be replaced before the surface condition actually would get into poor or very poor conditions. So only three roughness representative scenarios are used in this study: Very Good, Good and Average. As discussed

before, it is known that corrosion can cause the change of surface roughness in addition to deterioration of steel rebar. However, an appropriate model to directly link surface roughness and the corrosion effects is not available. Therefore in this study, the impact on bridge surface roughness from corrosion is indirectly correlated with the models of surface roughness and corrosion with time variable based on existing models.

Table 4.1: Road-Roughness Coefficient (RRC) values for road-roughness coefficient

Road-Roughness Classifications	Ranges for RRC
Very Good	2×10^{-6} to 8×10^{-6}
Good	8×10^{-6} to 32×10^{-6}
Average	32×10^{-6} to 128×10^{-6}
Poor	128×10^{-6} to 512×10^{-6}
Very Poor	512×10^{-6} to 2048×10^{-6}

4.1.1.2 Corrosion Representative Scenarios.

As illustrated in Chapter 2, reinforcement steel rebar will be corroded by the influence of chloride attacks causing bar area reduction. Consequently, concrete strength will decrease as the reinforcement bar area gets smaller. In this section, we will firstly quantify the change of the diameter of the reinforcement bars. Based on the new diameter of the rebar, the refined scale dynamic model will be analyzed and the fatigue damage accumulation is assessed. The changing in the diameter of the steel rebar due to chloride ingress can be calculated by using **Equation 2.32** which was originally suggested by Vu and Stewart (2002) and modified by (Oh et al. 2007). However, before we start calculating the changed diameter with time, we need to

find both the time to corrosion initiation (T_i) and the corrosion rate (i_{corr}). The time to corrosion initiation is usually calculated based on Flick's second law (Equation 2.4) which is defined as a function of the constant chloride diffusion coefficient (D_{ch}), the concrete cover, the surface chloride content (C_0) as well as the chloride threshold concentration value (cr). The surface chloride concentration (C_0) is assumed to be a constant value as Val and Stewart have assumed. Based on that, a value of 1.15 kg/m^3 has been assumed to be the constant value for the surface chloride concentration for our cases because this prototype bridge in Denver is located in Atmospheric zone $>1 \text{ km}$ from the coast (Table 2.1). The constant chloride diffusion coefficient (D_{ch}) will be calculated based on Papadakis's model (Equation 2.10) which in turn depends on concrete properties and concrete cover. The corrosion rate (i_{corr}) will be calculated from Equation 2.26. All of the results have been obtained for both time invariant corrosion rate and time variant corrosion rate in purpose of comparison between the two scenarios. Statistical parameters for corrosion variables and the concrete bridge deck material properties and dimensions are listed below in Table 4.2. MATLAB software has been employed to get these results. All of the results have been obtained for 100 years starting from the time to corrosion initiation.

Table4.2: Statistical parameters for corrosion variables and the concrete bridge deck material properties and dimensions

Parameter	Value
Surface chloride concentration $C_0 \text{ Kg/m}^3$	2.95
Threshold chloride concentration $C_{th} \text{ Kg/m}^3$	0.9
Concrete Cover $C \text{ (in)}$	2.5
Concrete compression strength (ksi)	4.5
Cement mass density Kg/m^3	1506
Aggregate mass density Kg/m^3	1600

Modulus of elasticity of steel (Mpa)	29000
Slab thickness (in)	8
Modulus of elasticity of concrete	$E_c = 4600 * F_c^{0.5}$
The mean 28 day cylinder strength	$f_{yc} = F_c + 7.4$
concrete tensile strength (MPa)	$f_t = 0.53 * F_c^{0.5}$
Water cement ratio (Bolomey's formula)	$w/c = (27 / (f_{yc} + 13.5))$
Aggregate cement ratio	$a/c = 6.703 * w/c - 0.084 + 6.364 * w/c - 0.258$
Effective elastic modulus of concrete (MPa)	$E_{ef} = E_c / (1 + C_c)$
Creep coefficient Cc	4
Thickness of the porous zone around the steel reinforcing bar (δ_o)	0.015
Poisson's ratio of concrete (ν)	0.2

4.1.1.2.1. Corrosion Rate:

Based on **Equation 2.26**, the time invariant corrosion rate has been found equal to $1.6 \mu A/cm^2$. However, the corrosion rate is supposed to decrease with time (time variant) due to the formation of rust products around the steel bars which will reduce the diffusion of iron ions away from the steel surface. Figure 4.1 presents the analysis results by the MATLAB model for the corrosion rate as a time variant parameter based on Vu and Stewart suggested model. It is clear that the corrosion rate will decrease from $16 \mu A/cm^2$ to $3.8 \mu A/cm^2$ within 100 years. This means that the rebar diameter will be corroded slower as the corrosion rate is decreased. Another important finding is that during the first 8 years after the initiation the corrosion rate will slightly decrease with time but after that it will reduce slowly as it reaches a nearly constant level.

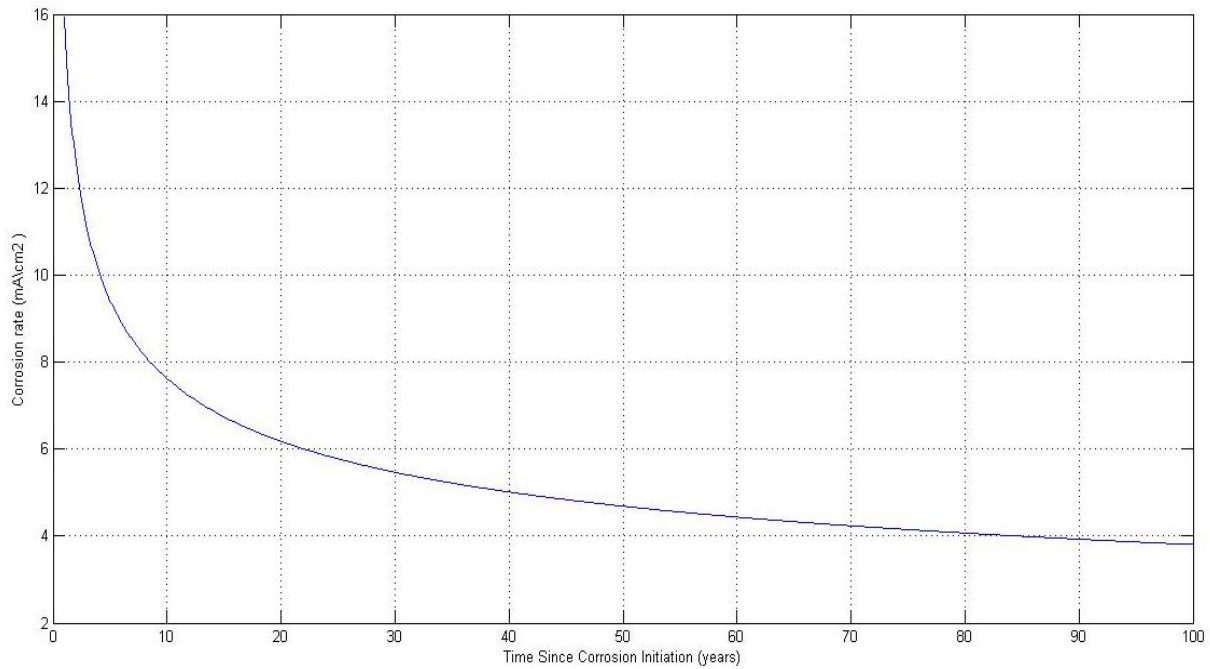


Figure 4.1: Time invariant corrosion rate

4.1.1.2.2. Reduction in the Diameter:

The time-dependent decreases in the steel bars areas for both time variant and time invariant corrosion rates are shown in Figure 4.2 and Figure 4.3 respectively. It is clear that for time variant corrosion rate about 6% of the cross section area of the reinforcing bars will be lost within the first 20 years since the corrosion initiation. Figure 4.3 shows how the cross section area of the reinforcing bars will decrease rapidly for time invariant corrosion rate. It is clear that the cross section area of the reinforcing bars will reduce linearly and about 15% of the cross section area of the reinforcing bars will be lost within the first 20 years since the corrosion initiation.

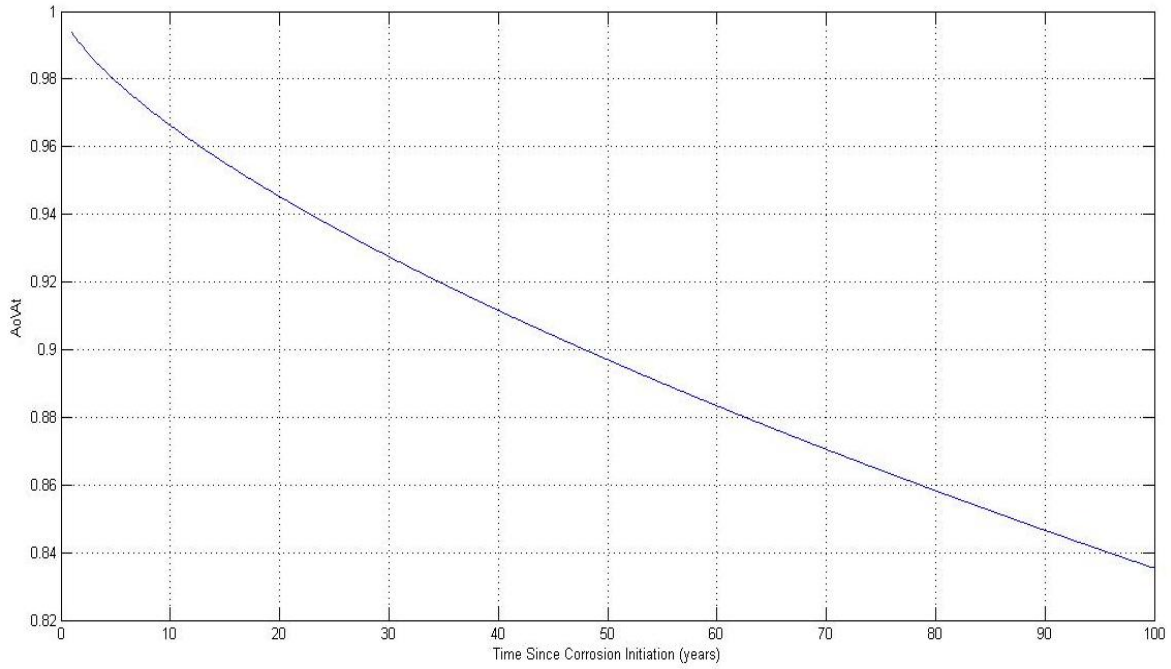


Figure 4.2: A_0/A_t for time variant corrosion rate

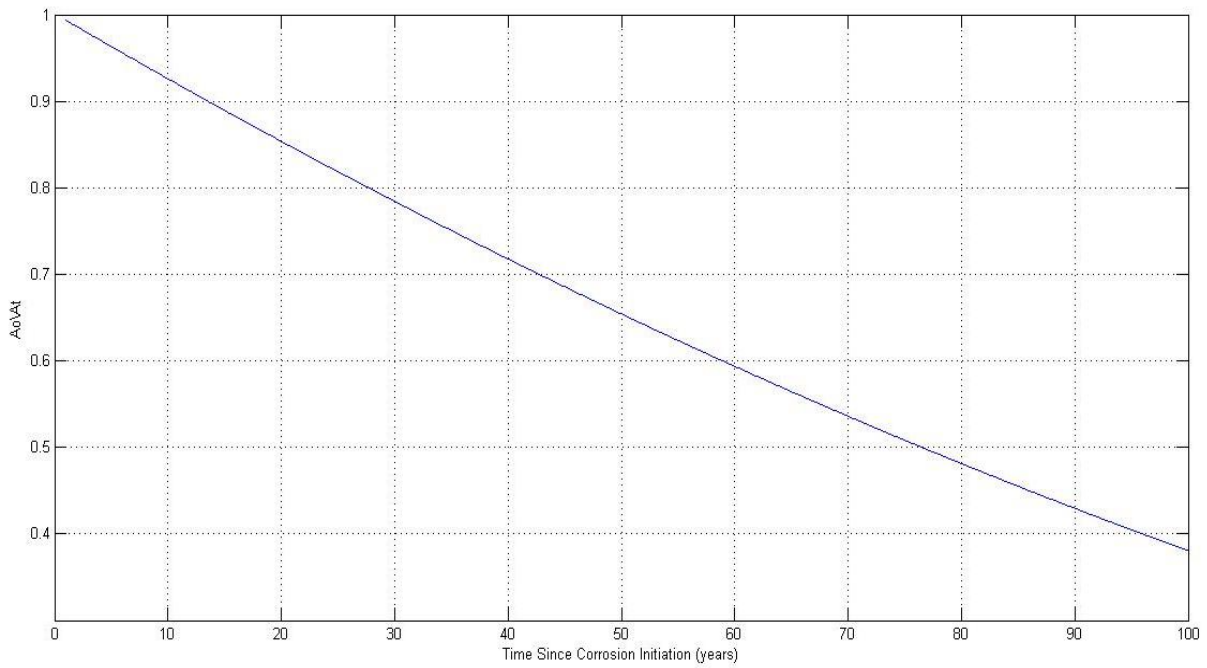


Figure 4.3: A_0/A_t for time invariant corrosion rate

4.1.1.2.3. The Nominal Moment Strength Mn:

The nominal moment strength Mn for the bridge's deck has been calculated based on the conventional flexural theory of reinforced concrete as follows:

$$M_n = A_s * f_y \left(d - \frac{a}{2} \right) \quad \text{Equation 4.1}$$

$$a = \frac{A_s * f_y}{0.85 f_c' * b} \quad \text{Equation 4.2}$$

The nominal moment strength depends directly on the area of the reinforcing steel. So it is clear that when the cross sectional area of reinforcing bars reduces over time due to corrosion, the nominal moment strength will also decrease. Figure 4.4 shows the reduction in the nominal moment strength due to time variant corrosion rate. It is clear that the nominal moment strength decreased by 8% within 100 years due to deterioration.

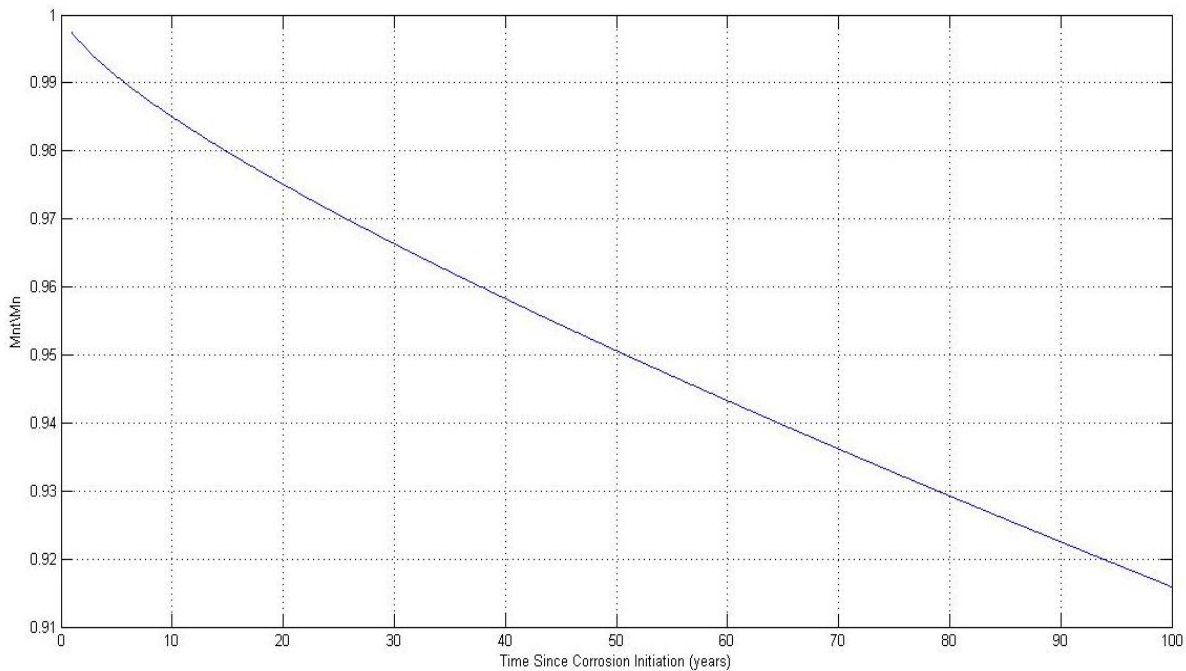


Figure 4.4: Moment of inertia for time invariant corrosion rate

Based on the results from the corrosion model developed with MATLAB by the writer, the corrosion effects on the reinforcing bars of the bridge deck has been approximately divided into four categories as follows:

- During the first year of the bridge service life, no apparent rust will be assumed on the steel (no-corrosion scenario).
- Light corrosion scenario will start from the second year to the fifth year of the bridge service life.
- From the sixth year to the tenth year of the bridge service life, the corrosion scenario will be considered to be Medium Corrosion Scenario.
- Severe corrosion scenario will occur during the last ten years of the twenty years of the study.

4.1.1.3 Traffic Representative Scenarios

The highway capacity manual (HCM) (National Research Council 2000) has classified the traffic volume on a highway into six levels of service (LOS) varying from service level A to service level F as illustrated in Ref. (National Research Council 2000). In this study, in order to maintain feasible computational efforts, the six levels of service are merged in to three levels as illustrated in Table 4.3.

Table 4.3: Three levels of service adopted in this study

3 levels of service	Representative vehicle density (vehicle/km/lane)
Free flow (T1) (LOS A~B)	10
Moderate (T2) (LOS C~D)	20
Congested (T2) (LOS E~F)	32

4.1.1.4 Combination of Traffic Flow and Corrosion

In the present study we have three representative traffic conditions, four representative corrosion conditions and three road roughness representative scenarios. In principle, at any time we could have varying traffic flow conditions since traffic flow is a random process. Considering typical variation nature of traffic volume over time, an hour has been taken to represent the basic time unit in which the traffic flow rate can be assumed to be constant. The flow rate can be calculated by converting the annual average daily traffic (AADT) to the flow rate of a month, week, hour and the probability of each traffic scenario to occur T_i can be found (Wu et al. 2012). Road roughness and corrosion conditions representative scenarios are essentially related because corrosion also causes the increase of road roughness. So, for the corrosion and road roughness conditions we will have only joint condition for a certain time of the bridge service life i.e. we will have “No-corrosion condition” for the first year of the service life of the bridge at the same year the roughness of the road will be considered as “Very-Good”. As a result, we will have totally twelve representative combined scenarios of traffic, road roughness and corrosion conditions. Table 4.4 summarizes all of the combined representative scenarios in this study. Therefore, the probability of K_{th} representative scenario $P(c_i s_i)$ to occur in a year equals to the occurrence probability of the traffic representative scenario (T_i) to occur in that year. The traffic volume increase over years is known to be very site-specific, and hard to be quantified in a general way. As the first step without introducing unnecessary complexness and uncertainties, we have neglected the effect of the growth facto of AADT which means the probability of each traffic scenario to occur in a year will be the same along the service life of the bridge:

$$P(c_i s_i) = P_{s_i} \quad \text{Equation 4.3}$$

Table 4.4: The combined representative scenarios

Roughness Condition	Corrosion Condition	Traffic Conditions		
		Light	Moderate	Heavy
Very Good	No-Corrosion	K1	K2	K3
	Light	K4	K5	K6
Good	Medium	K7	K8	K9
Average	Severe	K10	K11	K12

4.1.2 Calculating Cumulative Fatigue Damage Factor for a Typical Hour.

This section consists of four major steps as follows: (1) obtaining stress time history of the bridge, (2) using Rainflow cycles method to decompose the stress time histories, (3) using S-N curves, and (4) using the miner’s rule method. Figure 4.5A and 4.5B depicts the steps for calculating fatigue damage factor for each typical year.

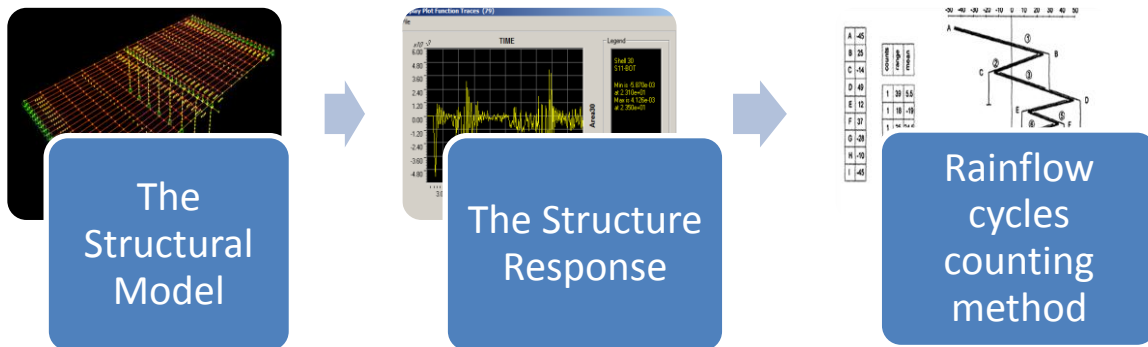


Figure 4.5A: Steps for calculating fatigue damage factor for each typical year.

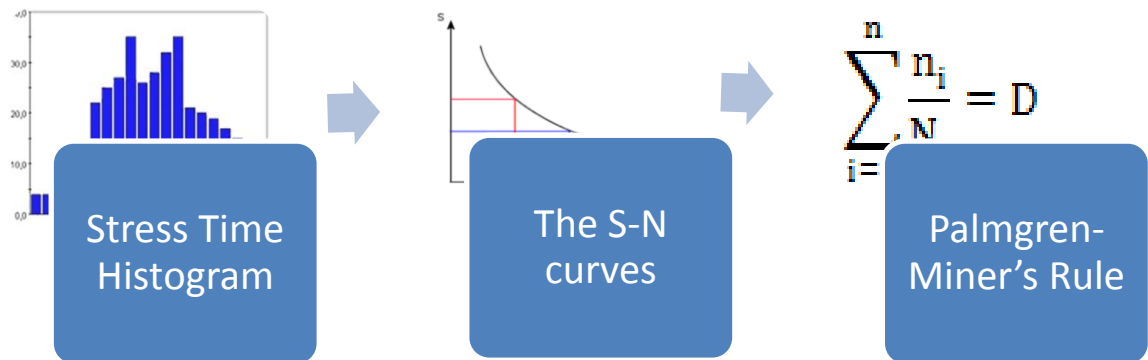


Figure 4.5B: Steps for calculating fatigue damage factor for each typical year.

4.1.2.1 Obtaining Stress Time History of the Bridge

In order to evaluate a structure under fatigue loading, the first thing to do is to obtain the structure response under each representative combined scenario with the hybrid dynamic analytical model as introduced in Chapter 3. The structural response under dynamic loads is typically assessed in the form of stress or strain time history functions. In this study, a refined-scale SAP2000 model as introduced in Chapter 3 was developed for the prototype bridge. The time-dependent loads from stochastic traffic were obtained using equivalent wheel load approach and converted to nodal time history input of the SAP2000 model. The detailed process has been discussed in the hybrid dynamic analytical model in Chapter 3, hereby not repeated. Since the traffic loads are stochastic dynamic loads, which change in position and magnitude with time. Because of that, the nonlinear time history analysis method is used herein to determine the dynamic response of the bridge with the refined-scale SAP2000 bridge model. After conducting the dynamic analysis, the stress time histories response of all the nodes in the bottom of the bridge deck can be obtained for each representative scenario.

4.1.2.2- Using Rainflow Cycles Counting Method to Decompose the Stress Time Histories

After we obtain the stress/strain time histories for the structure, we need to count the number of stress cycles N_i for the chosen plates of the structure deck. If we have a constant value of loading, the number of stress cycles will be directly obtained from the S-N curves of the material. However, the response time history, either in terms of stress or strain, actually varies over time, namely we have stress time history with different peaks and valleys amplitudes. Therefore, using one of the cycle counting methods to decompose the number of stress cycles those have been absorbed by the structure under dynamic loads is essential. As we have explained in the chapter 2, the Rainflow cycles counting method is considered as the best method

as compared to the other methods in terms of simplicity, accuracy and time consuming. Because of that, in our study we will use this method to decompose the irregular time history into equivalent stress or strain of block loading.

4.1.2.3- S-N Curves

After counting the number of stress cycles for each stress range, we go to the typical S-N curves to obtain the number of stress cycles up to fail (N_i) can each stress range cause. The S-N curves are usually presented in either log-log plot or semi log plot, which converts the relationship of stress amplitudes and number of cycles to fail to a linear relationship. We can find the number of stress cycles to fail N_i for a specific material under a stress amplitude or range S_i , by knowing both the S-N curve slope m , and any coordinate pair (S_0, N_0) through using Equation 4.4 that can be concluded from Figure 4.6.

$$N_i = N_0 \times \left(\frac{S_i}{S_0}\right)^{\frac{1}{m}} \quad \text{Equation 4.4}$$

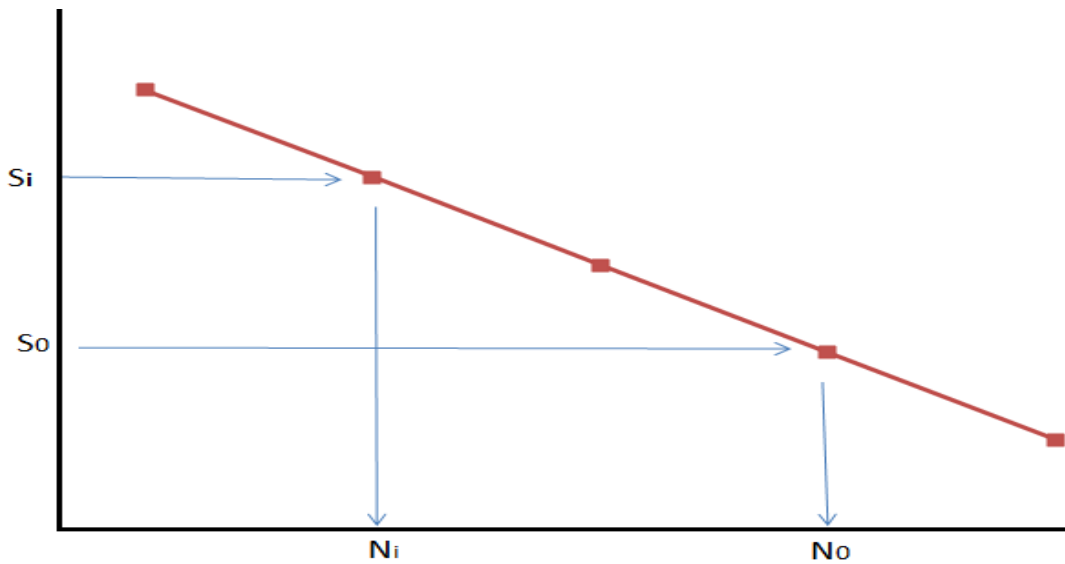


Figure 4.6: S-N curve equation

4.1.2.4- The Miner's Rule Method

According to Palmgren-Miner rule, linear damage rule, the total damage is the sum of the individual damage ratios and it states that the failure occurs when the total damage equals to the unity.

$$D_i = \sum_{i=1}^n \frac{n_i}{N_i} = 1 \quad \text{Equation 4.5}$$

So, the total damage can be calculated by dividing the number of cycles found in the time domain for each stresses to the number of cycles found from the S-N curve approach.

4.2 Time-Progressive Dynamic Analysis Procedure

As shown in Fig. 4.7, time-progressive dynamic analysis procedure starts with time-dependent corrosion model, which will quantify rebar dimension reduction and the surface roughness change over time. At a particular time of the lifespan, the updated surface roughness level will be brought into the bridge/vehicle/roughness coupled model (Fig. 4.7) to quantify the updated equivalent wheel load of vehicles with interactions. By considering the time-specific traffic condition, the stochastic traffic flow can be simulated and in turn the cumulative wheel loads of stochastic traffic and nodal force time histories of the refined SAP model. In the meantime, the rebar dimension of the refined SAP model is also updated based on the rebar dimension reduction model due to corrosion. The time-domain dynamic analysis of the refined bridge model is conducted to obtain the time histories of the bridge deck response, such as displacement and stress. The stress histories can be analyzed to predict the fatigue damage accumulation. In the next time step, the same procedure will repeat again with the new conditions from the corrosion and surface roughness models. In principle, this time-progressive analysis process can continue in very small time steps (e.g. seconds, minutes). Considering the time-varying nature of traffic volume and the corrosion development, too small time steps are

not necessary except causing unrealistic computational burden. Traffic condition can be approximated to be the same within each hour of a day. For corrosion, 1 year is probably a reasonable time unit to consider the change, which can practically cause considerable impact on the bridge deck performance.

Therefore, for fatigue damage assessment, the stress time history obtained from time-domain analysis with a certain time period will be assessed and expanded to one hour as introduced in Section 4.1, assuming there is no considerable change of traffic or corrosion condition within the same hour. In the next hour, the new traffic density will be updated following the daily traffic density variation information, but the corrosion condition still remains the same. This process repeats for 24 hours of a day. Following the weekly traffic volume variation, the process repeats for each day considering daily variation within a week. The corrosion condition will not be updated until the next year and will remain the same for all the hours within that year. Once the cumulative fatigue damage assessment is made for a week, the same results will be extrapolated to one month assuming there is no weekly difference within the same month. Once monthly simulation is finished, the same process will further extend to each month of a year by following the monthly traffic volume variation within a year. Finally, the yearly cumulative fatigue damage can be assessed. Between years, the corrosion effects are considered. Typically, traffic volume may have some increase over years, and the yearly increase of traffic volume is found to be very site-specific with lots of uncertainties. As discussed earlier, to avoid introducing unnecessary uncertainties when the updated corrosion effects over years are considered, the yearly growth of traffic volume is not considered in the present study. Only the corrosion-causes effects will be considered over different years.

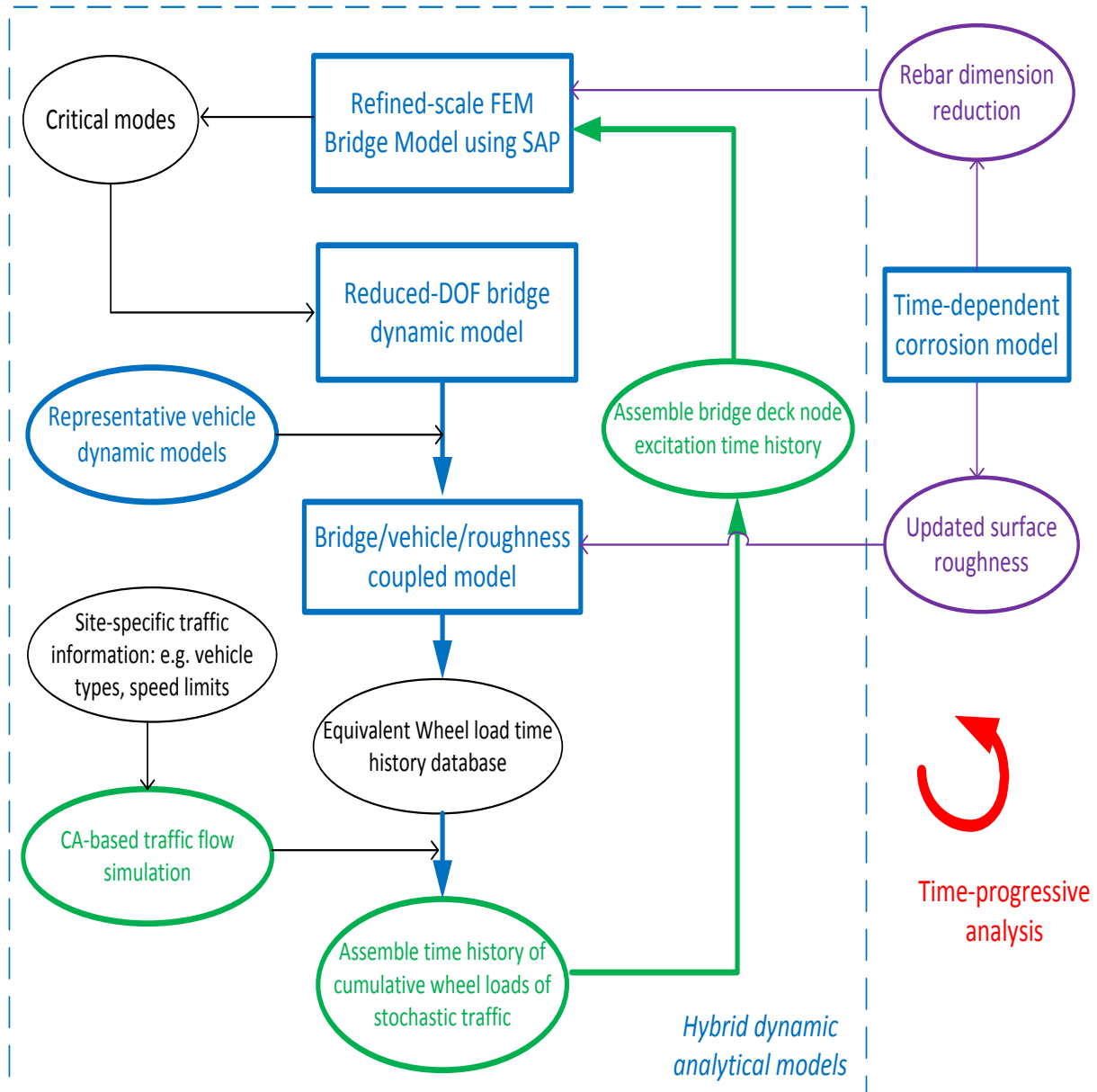


Figure 4.7: Time-progressive analysis procedure with hybrid dynamic analytical model

Chapter 5: Results of Fatigue Assessment of the Bridge Deck

5.1. Overview:

The results have been obtained in time domain and the fatigue strength was estimated based on s-n curves approach. Fatigue life calculation has been carried out by adopting the Palmgren-Miner rule along with the rainflow cycle counting procedure. The resultant stresses due to the dynamic loads for the bottom of the deck have been obtained for different joints in the bridge deck by using SAP2000 software for 90 seconds.

5.2 The Resultant Stresses:

In this study, the middle four elements have been chosen to calculate the estimated fatigue life of the bridge deck as they are supposed to have the largest stresses. Figure 5.1.A shows the locations and numbers of the joint those have been chosen in this study. Figure 5.1.B shows the locations of the elements chosen in this study. The resultant stresses for each representative traffic condition (T_i) “Free, Moderate and Congested” versus time steps can be drawn for the data collected for 90 seconds as it is shown in Figure 5.2. Figure 5.2 shows the resultant stresses for the heavy, moderated and light traffics scenarios with “no-corrosion” condition for a particular joint (#1580) versus the time steps. It is found that all the stresses are larger than zero suggesting the fact that the bottoms of the bridge deck elements are always under tension. As expected, the resultant stresses from the heavy traffic are much bigger than those from the moderate and the light in magnitude. However, it is clear that the resultant stresses from the moderate traffic have larger stress-ranges than the resultant stresses from the heavy traffic. However, as it can be seen in Figure 5.2, the first 50 seconds of the bridge response is composed of small amplitudes which indicates that girders have not been excited yet. For this reason, the first 50 seconds of the resultant stress signal has been truncated and only the last 40

seconds has been used to evaluate the fatigue performance of the bridge deck. Figures 5.3 to 5.5 show a comparison between the resultant stresses for different joints under different traffic loads, corrosion conditions and road roughness scenarios.

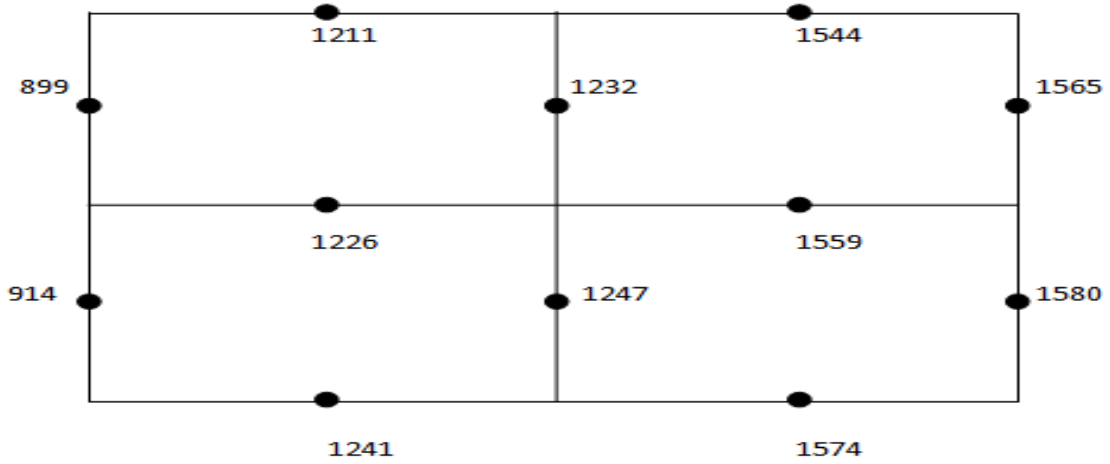


Figure 5.1A: Joint locations and numbers

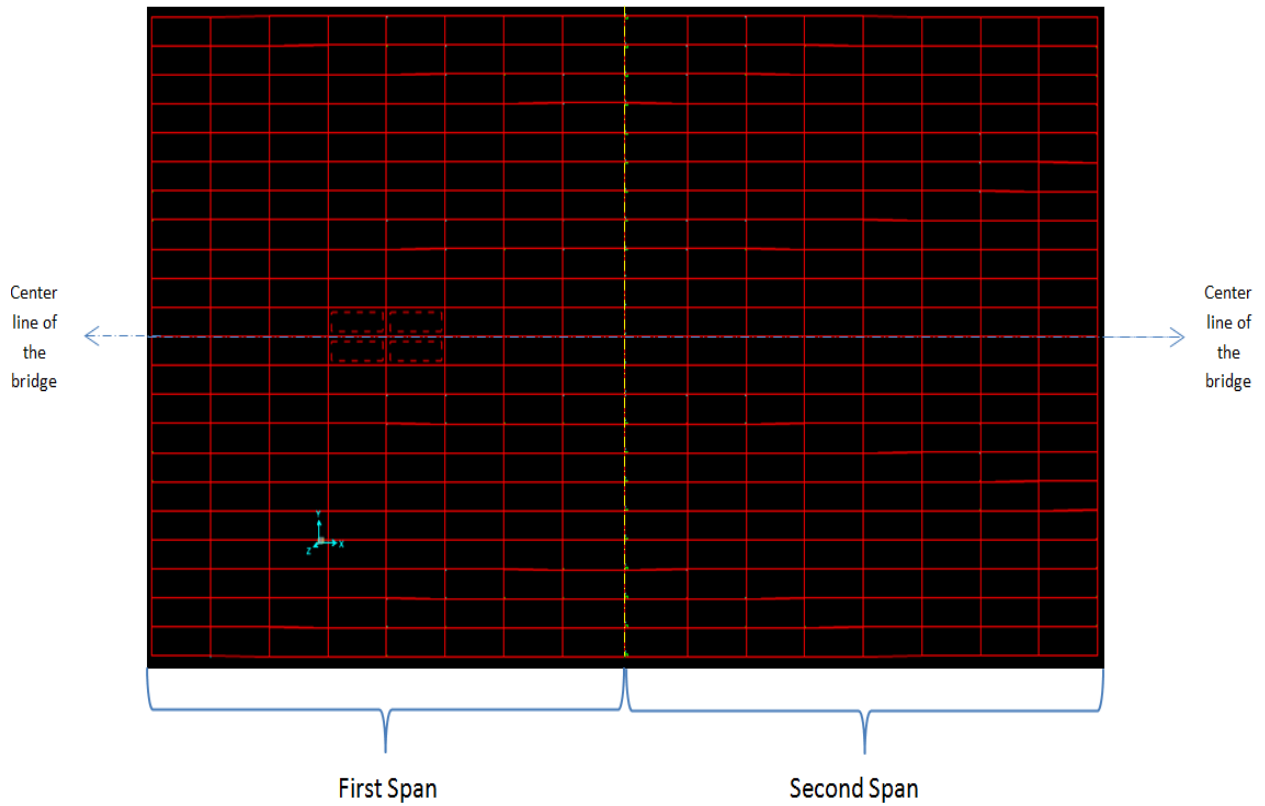


Figure 5.1.B: locations of the elements chosen in this study

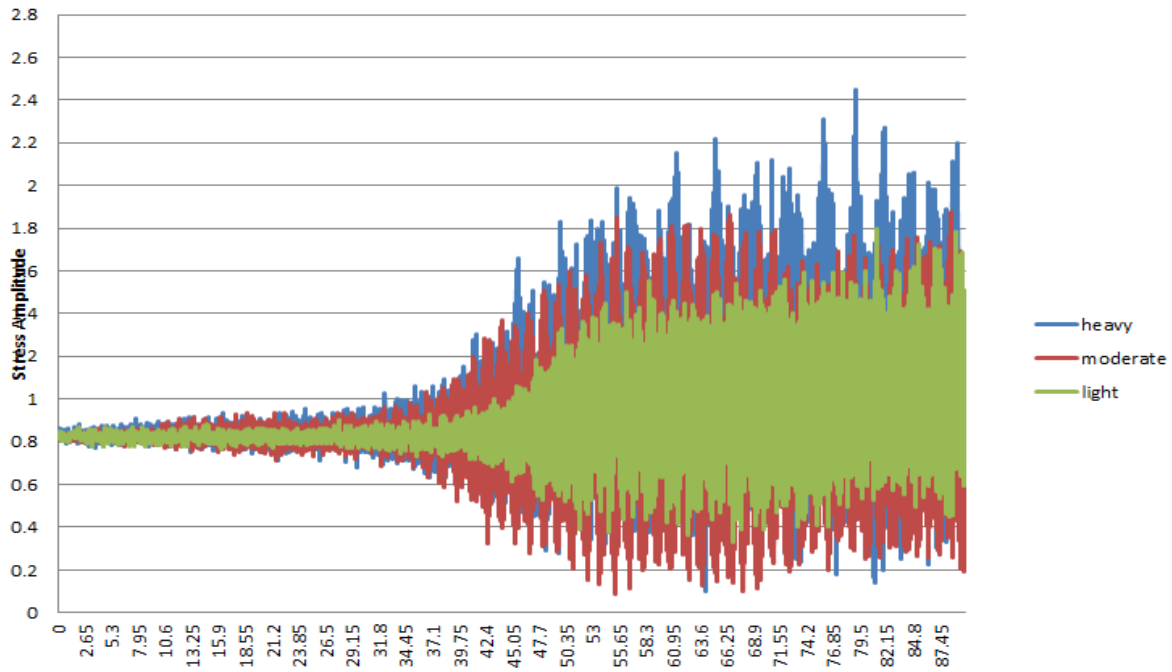


Figure 5.2: Stress amplitudes versus time steps for heavy, moderated and light traffic for joint#1580

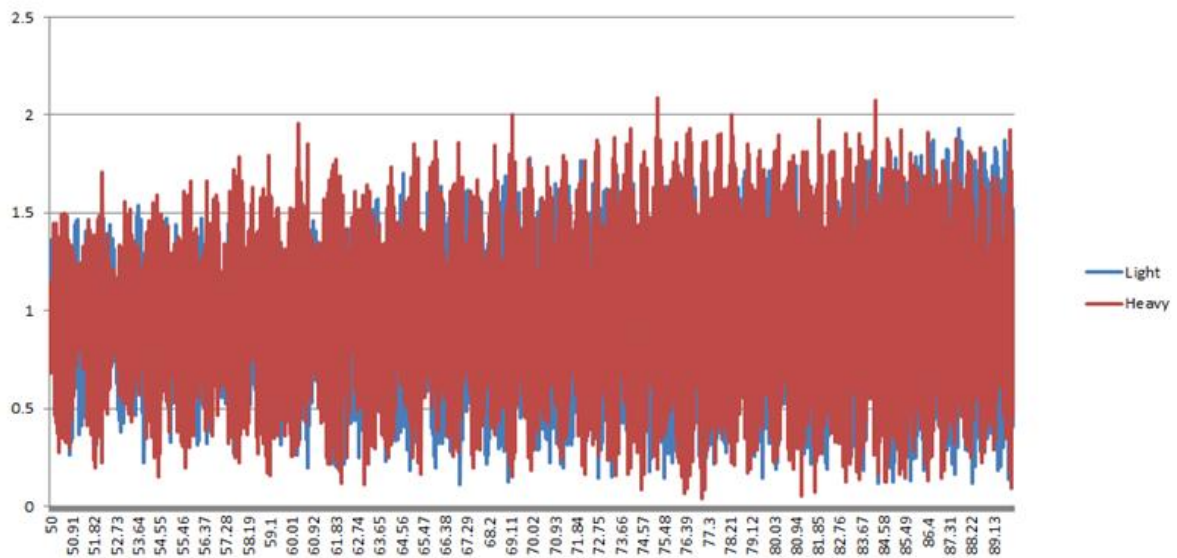


Figure 5.3: Stress amplitudes versus time steps for Heavy, Light traffic under Good Roughness and Medium-Corrosion conditions for joint #1565

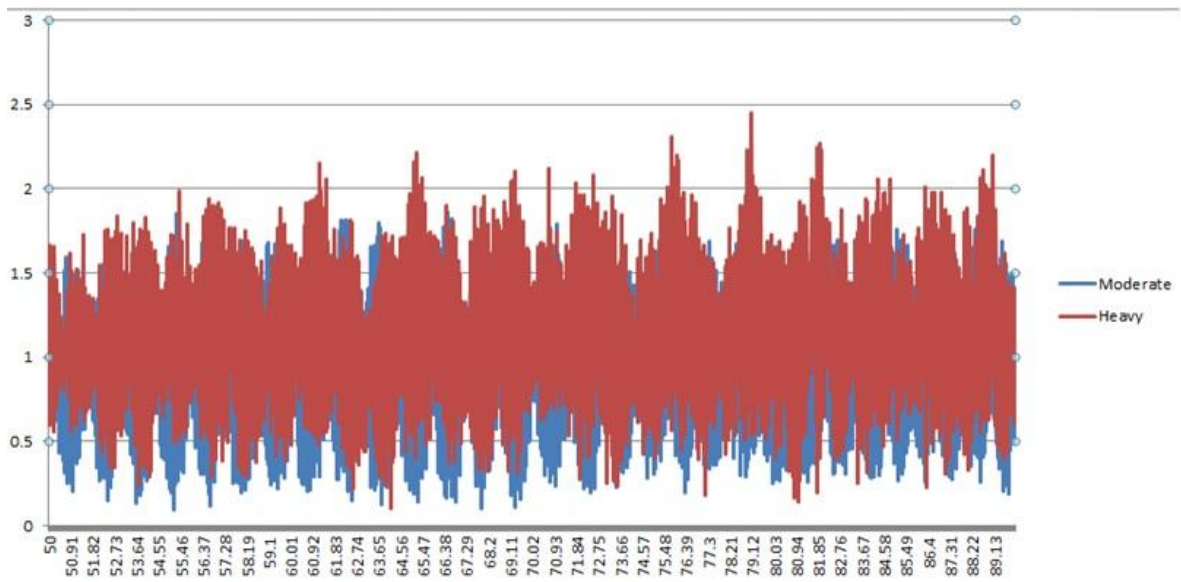


Figure 5.4: Stress amplitudes versus time steps for Heavy, Moderate traffic under Very-Good Roughness and No-Corrosion conditions for joint # 1580



Figure 5.5: Stress amplitudes versus time steps for No-Corrosion conditions (Very-Good roughness) and Medium-Corrosion conditions (Good roughness) under Moderate traffic for joint #1559

5.3. The Results from the Rainflow Cycles Counting Method:

Cycle counting by using Rainflow has been executed to find the Rainflow cycles in time domain for the stress signals. Each classified cycle has been described by the stress amplitude and the mean stress value. According to the S-N curve chosen for this study, the equation of the concrete material has been obtained and the number of cycles has been found equals to:

$$N_i = 1 * 10^{\left(\frac{si-1.13}{-0.086487}\right)} \quad \text{Equation 5.1}$$

Cycles count versus stress amplitude value is obtained and the results are shown in Figure 5.6 to Figure 5.11 for Heavy, Moderated and Light traffics respectively for joint #1580 under “no-corrosion” condition. As we do a comparison between those figures, it is clear that the stress ranges amplitudes and the encounter numbers of cycles from the heavy traffic are larger than those from the moderate and light traffic. Consequently, we can predict that the fatigue damage index from the heavy traffic will be larger than those from the moderate and light traffic. Figure 5.12 to Figure 5.17 show cycles count versus stress amplitude value for Heavy, Moderate and Light traffics respectively for another joint #914 under “no-corrosion” condition. In these figures it is clear that the stress ranges amplitudes from the heavy traffic is larger than the stress ranges amplitudes from the moderate and light traffic. However, when we compare Figure 5.12 and Figure 5.14 we find out that the larger stress cycles from the moderate traffic are concentrated in the middle of the chart while the larger stress cycles from the heavy traffic are concentrated in the left side of the chart. In other words, the number of stress cycles for the large stress ranges amplitudes (0.45 -0.9 ksi) from the moderate traffic are larger than those from the heavy traffic. From this comparison we can say that even if the stress amplitudes increase slightly with the increase of the traffic condition the numbers of cycles of different stress ranges vary in a complicated manner.

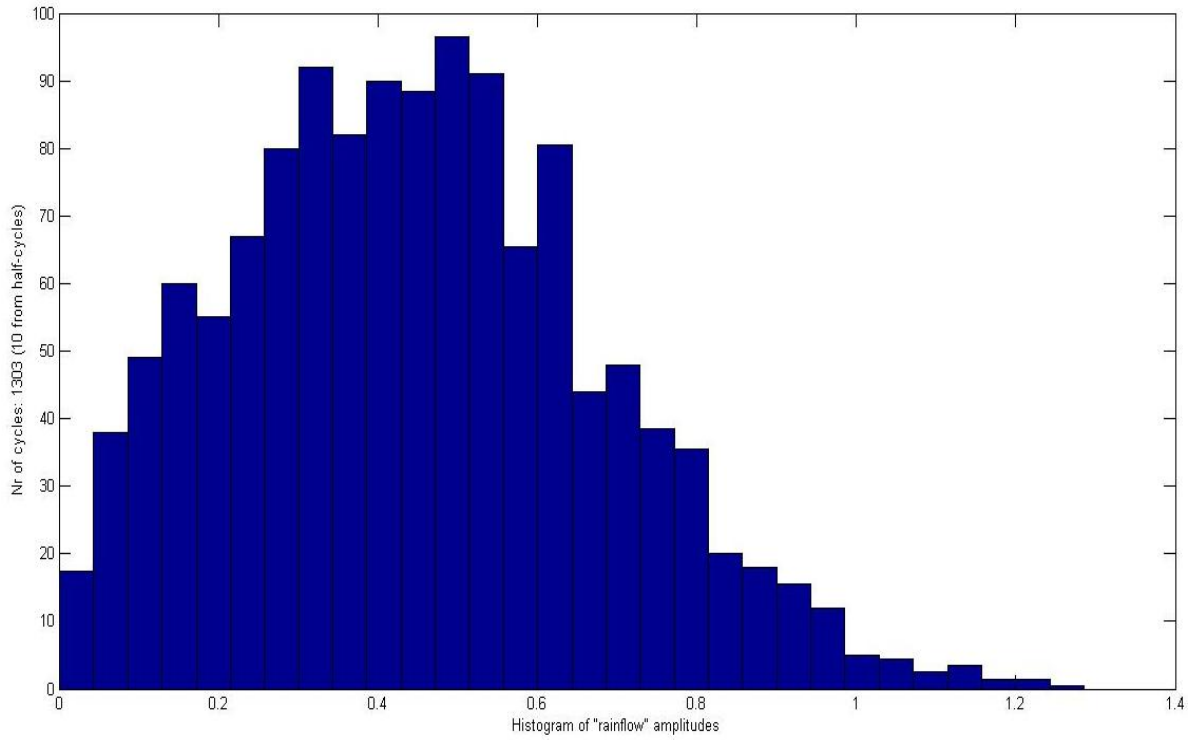


Figure 5.6: Stress ranges amplitudes versus Number of cycles for the heavy traffic (Joint#1580)

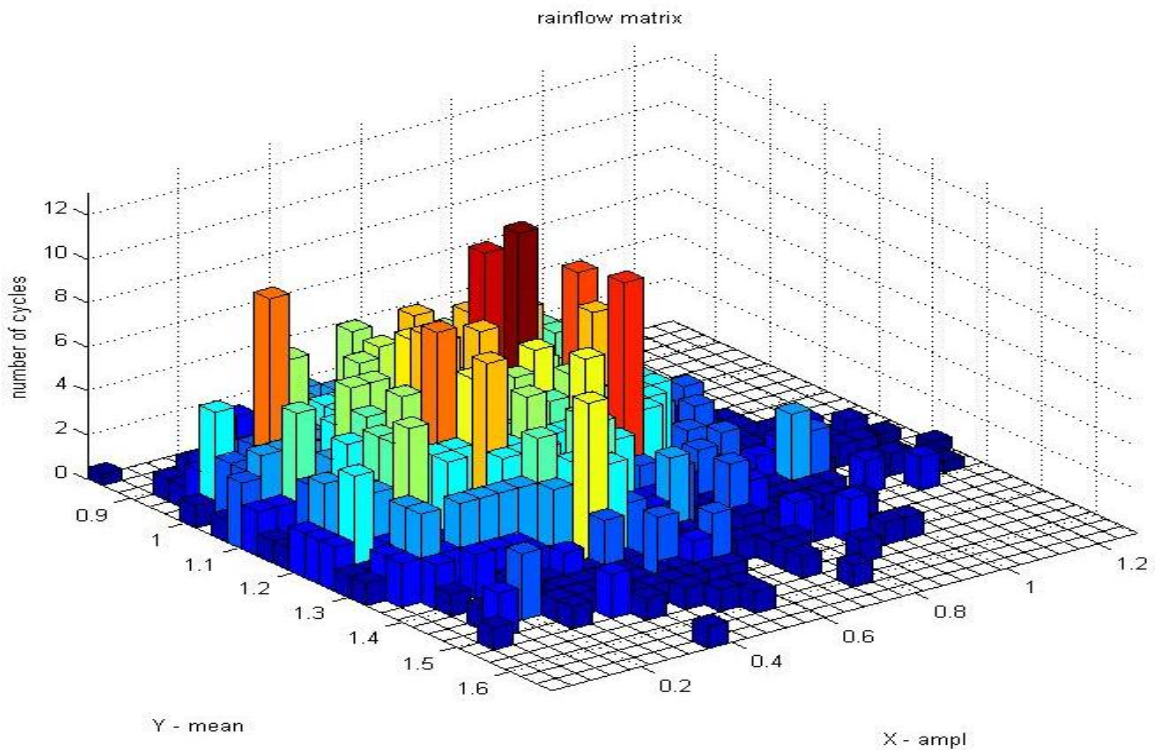


Figure 5.7: Stress ranges amplitudes and mean classes versus number of cycles for the heavy traffic (Joint#1580)

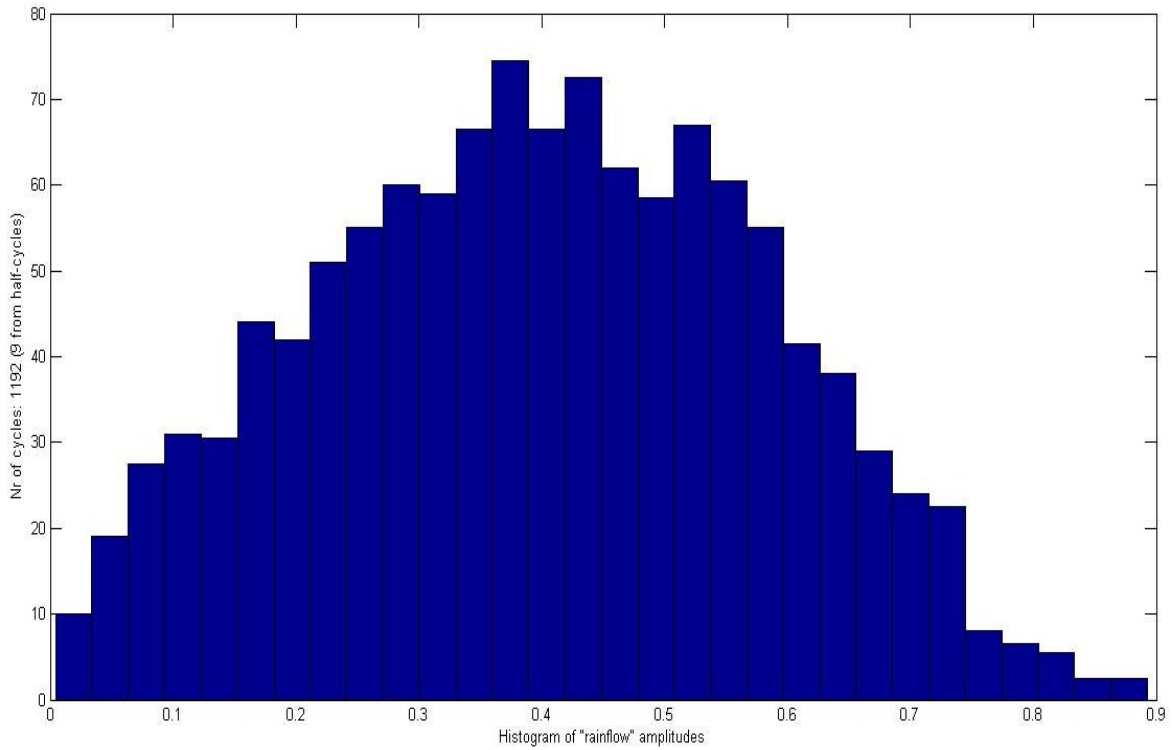


Figure 5.8: Stress ranges amplitudes versus Number of cycles for the moderate traffic (Joint#1580)

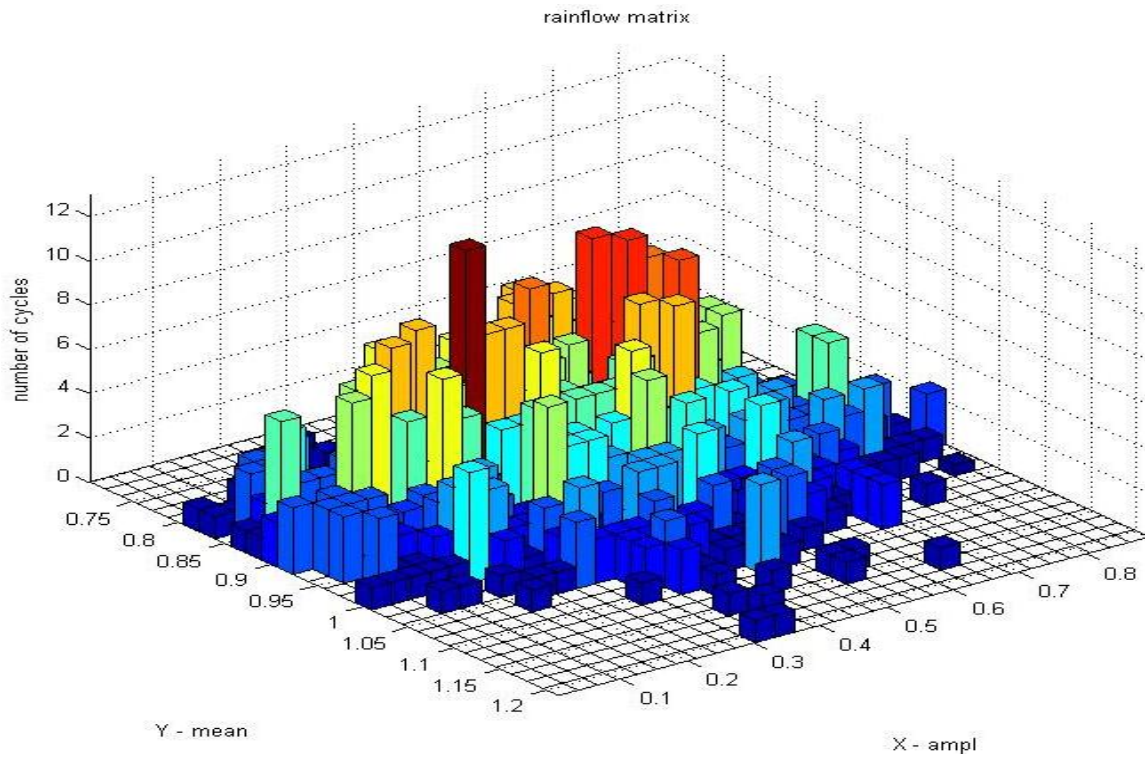


Figure 5.9: Stress ranges amplitudes and mean classes versus number of cycles for the moderated traffic (Joint#1580)

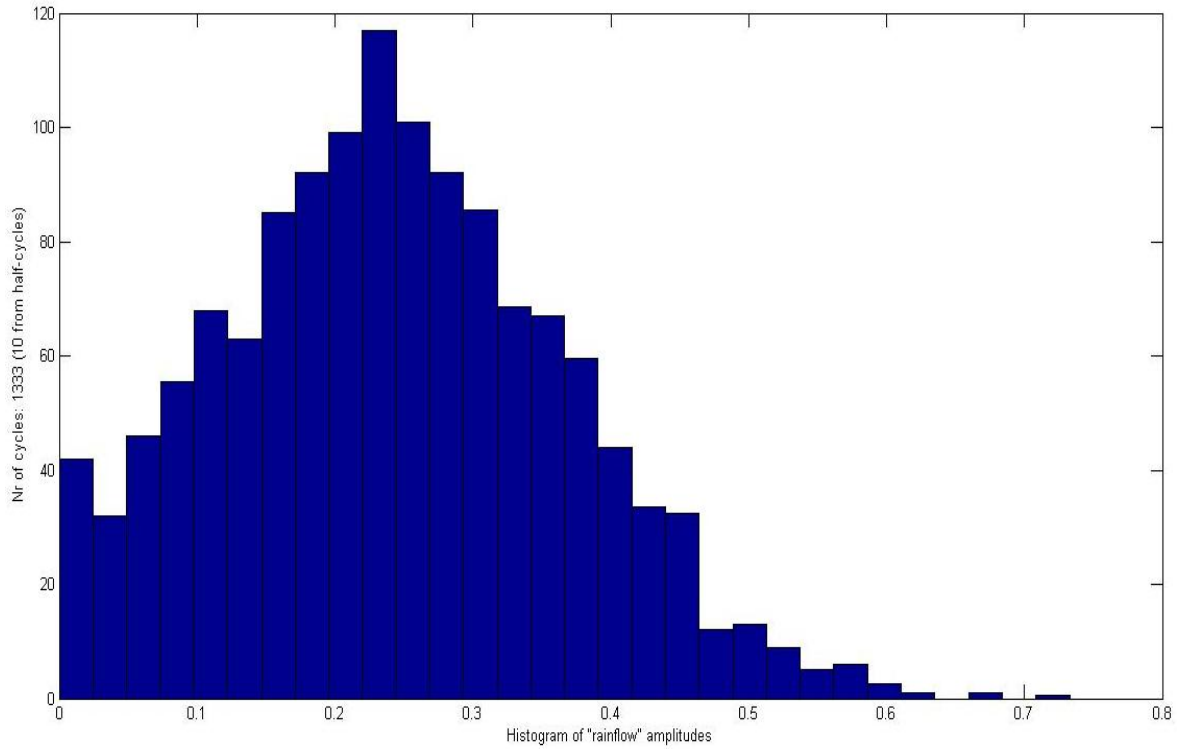


Figure 5.10: Stress ranges amplitudes versus Number of cycles for the Light traffic (Joint#1580)

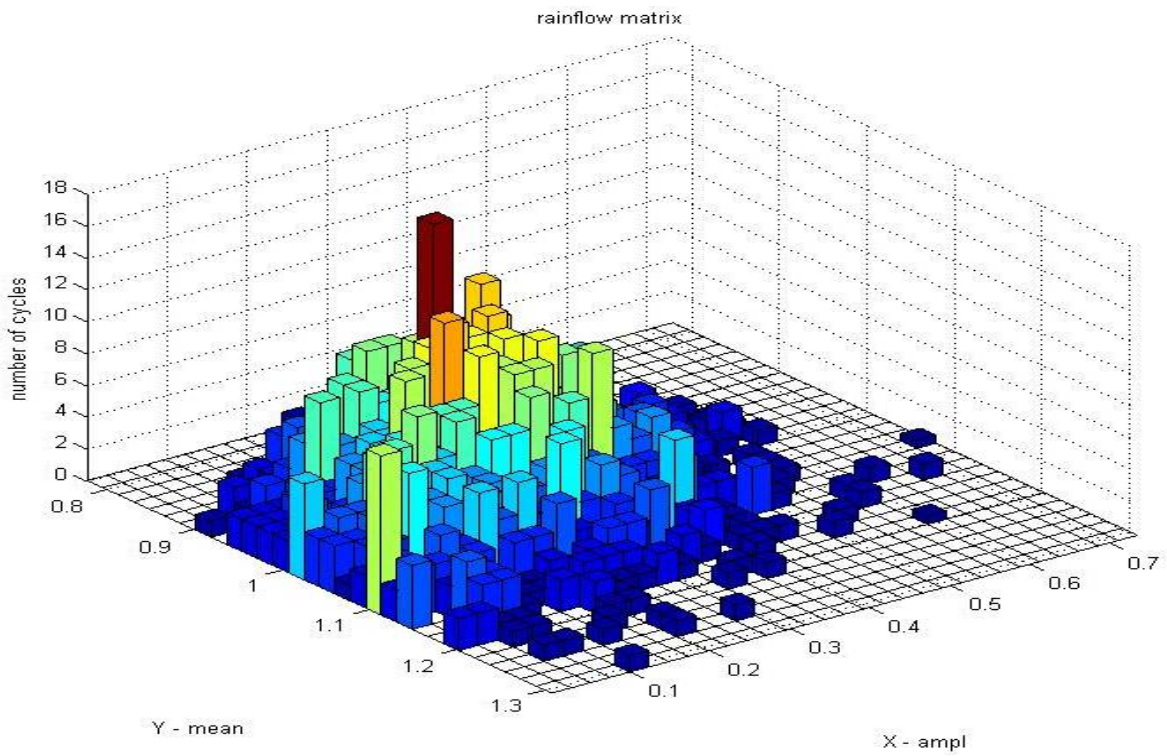


Figure 5.11: Stress ranges amplitudes and mean classes versus number of cycles for the light traffic (Joint#1580)

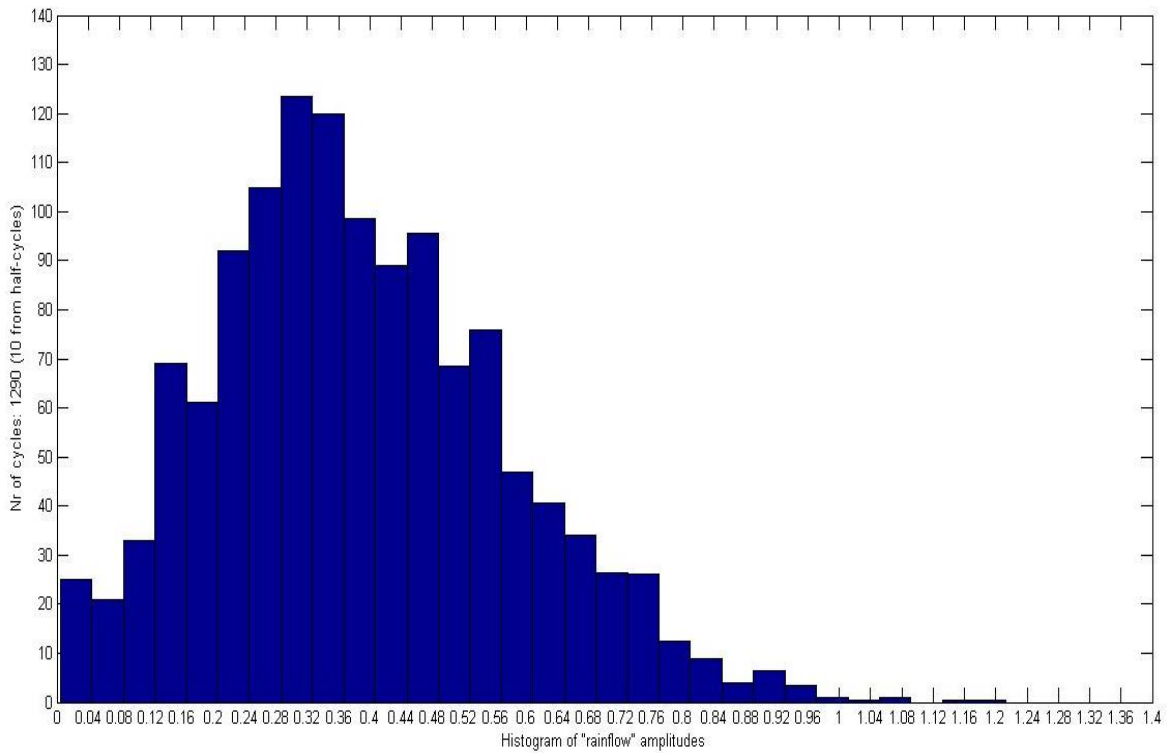


Figure 5.12: Stress ranges amplitudes versus Number of cycles for the Light traffic (Joint# 914)

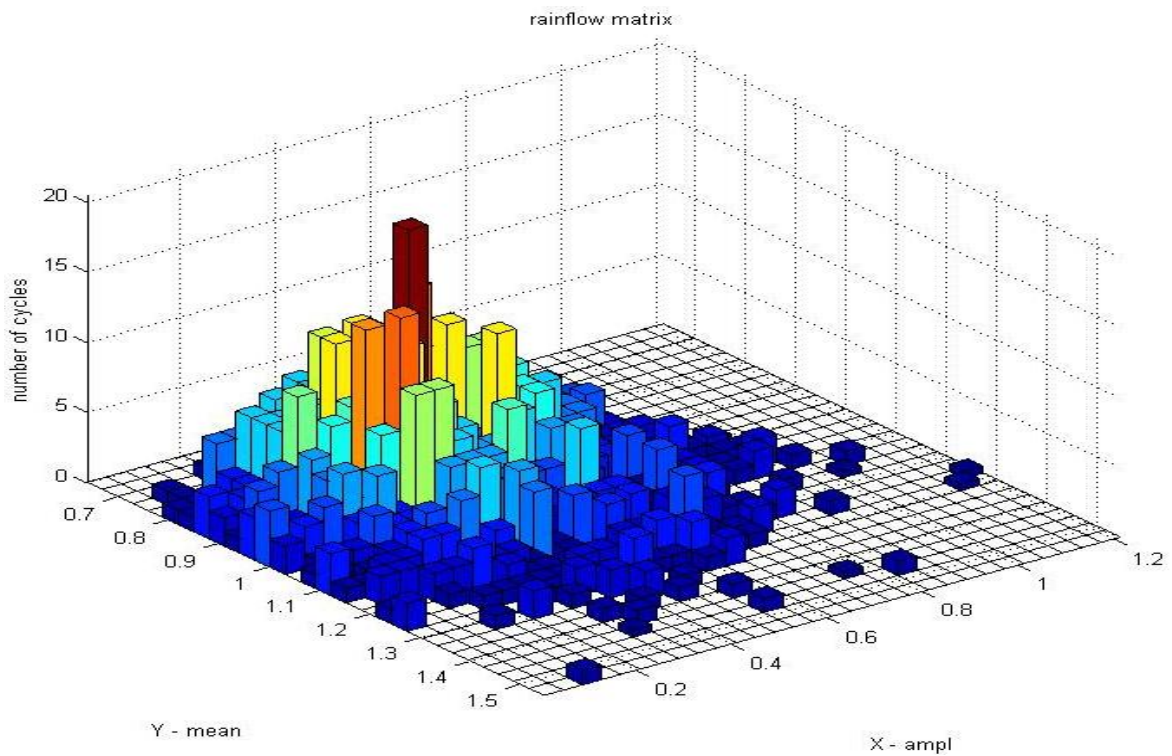


Figure 5.13: Stress ranges amplitudes and mean classes versus number of cycles for the heavy traffic (Joint# 914)

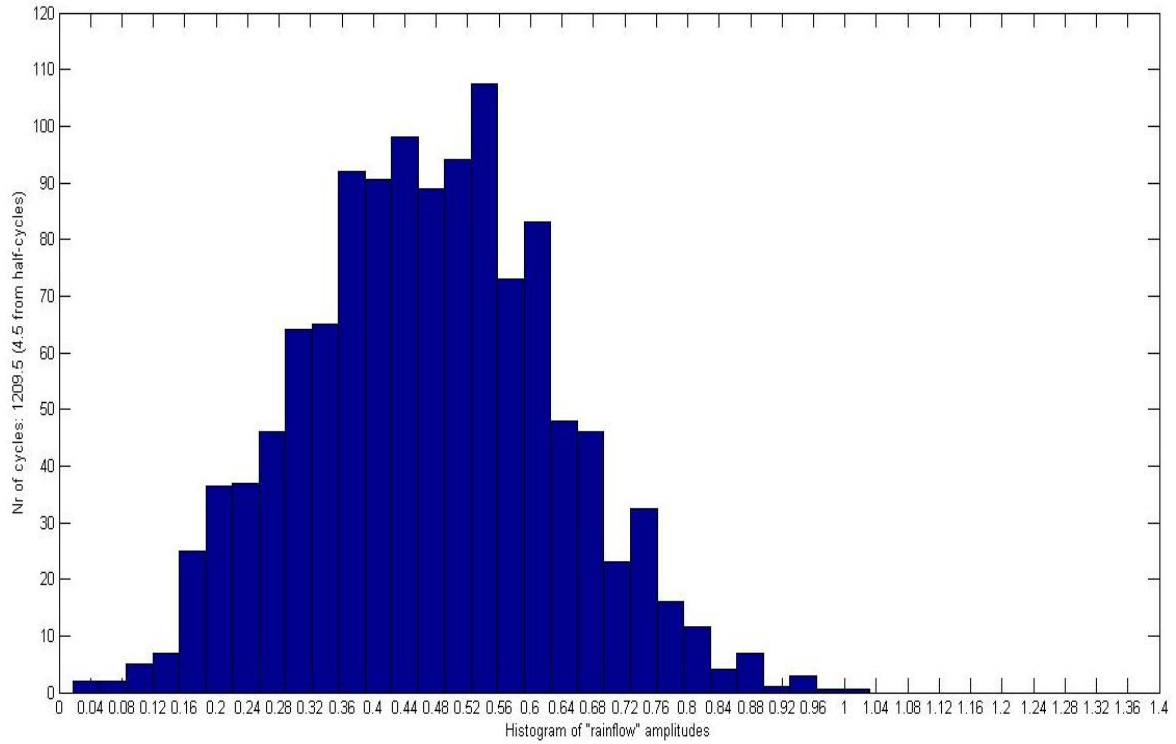


Figure 5.14: Stress ranges amplitudes versus Number of cycles for the Light traffic (Joint# 914)

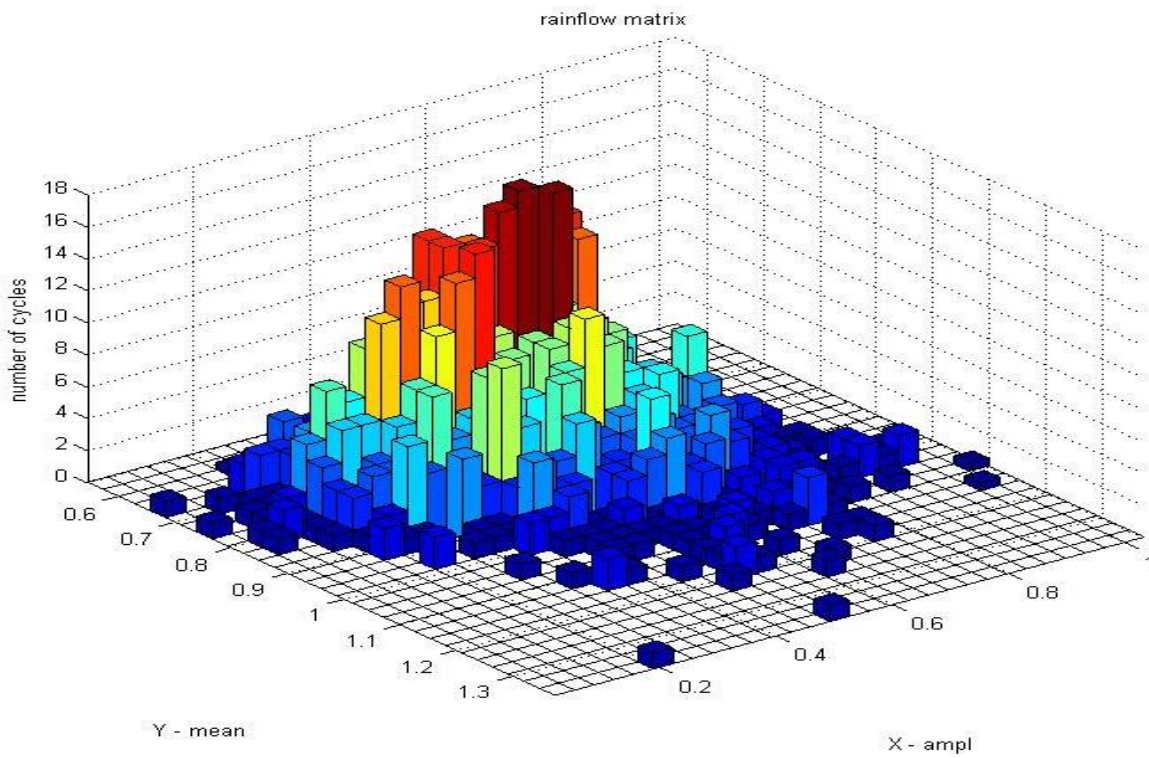


Figure 5.15: Stress ranges amplitudes and mean classes versus number of cycles for the heavy traffic (Joint# 914)

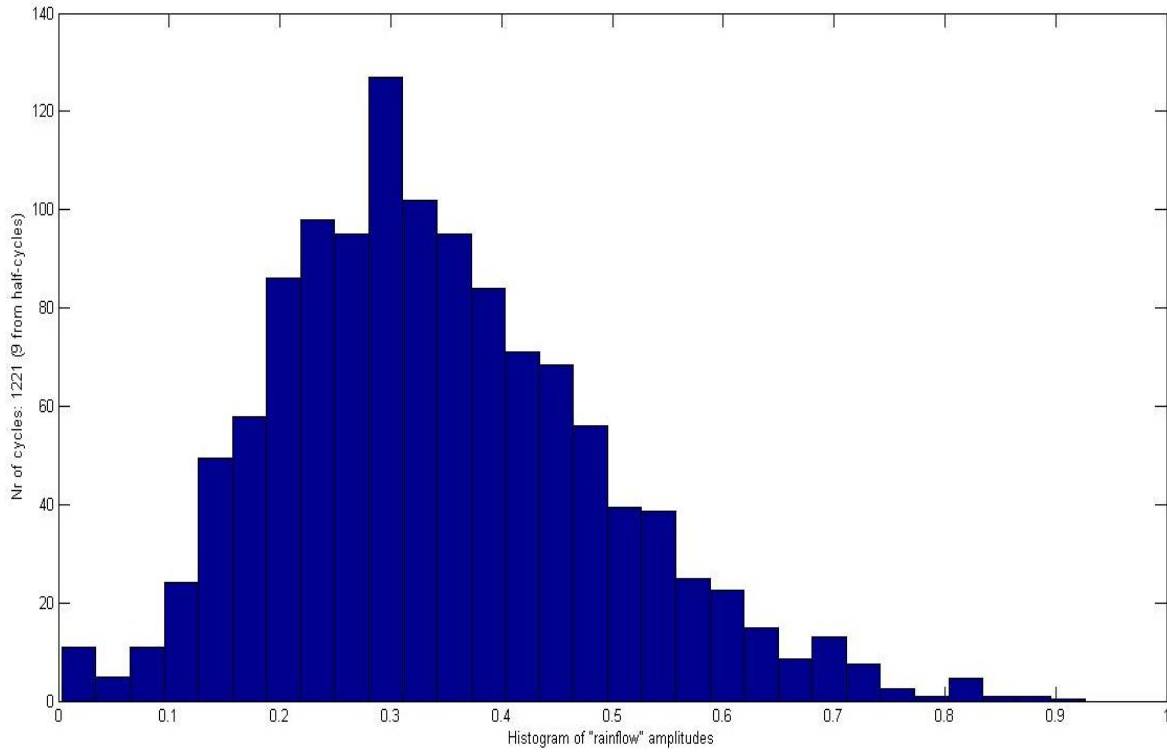


Figure 5.16: Stress ranges amplitudes versus Number of cycles for the Light traffic (Joint#914)

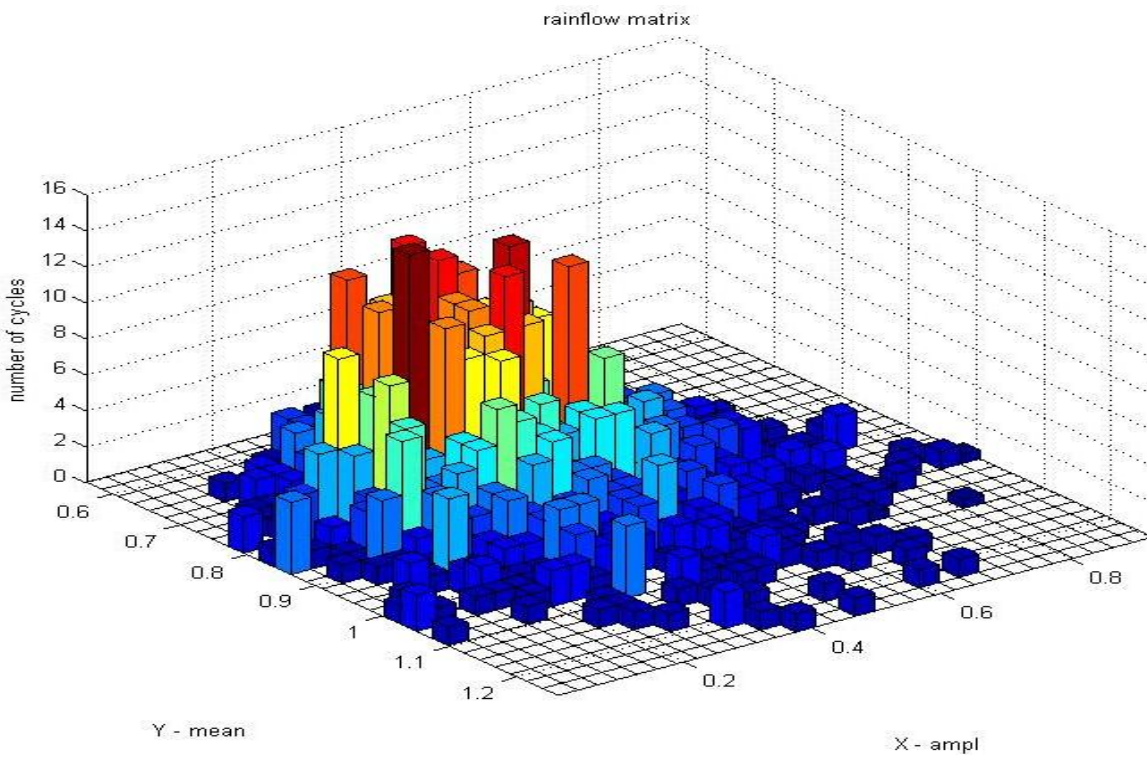


Figure 5.17: Stress ranges amplitudes and mean classes versus number of cycles for the heavy traffic (Joint#914)

5.4. Fatigue Damage Indices for Each Representative Scenario:

According to Palmgren-Miner rule, linear damage rule, the total damage is the sum of the individual damage ratios. Fatigue failure is defined to occur when the total damage equals to the unity.

$$D_i = \sum_{i=1}^n \frac{n_i}{N_i} = 1 \quad \text{Equation 5.2}$$

The total damage can be calculated by dividing the number of cycles found in the time domain for each stress from the Rainflow cycles counting method to the number of cycles found from the Equation 5.1. However, as we illustrated previously, in this study an hour is taken as the basic time period during which the traffic flow and corrosion rates are assumed to be constant. Because of that, the hourly fatigue damage factor (DF_i) for each representative scenario (CT_i) has been calculated through Equation 5.3 following Miner's law as following:

$$DF_i = \sum_{i=1}^n \frac{n_i}{N_i} * \frac{3600}{40} \quad \text{Equation 5.3}$$

Table 5.2 shows the hourly fatigue damage factors (DF_i) for each joint of the four elements chosen for each particular scenario. It is found that corrosion and rough road surface together can cause large fatigue damage index. However, the fatigue damage index does not always increase with the increase of the traffic density. For example, moderate traffic will cause the largest fatigue damage index per hour for the Joint #1544. By neglecting the growth factor of ADDT, the percentages of the total hours for each representative traffic condition in each year are assumed to be constant during the 20-year study period. By evaluating the hourly, daily and weekly variations of AADT as defined by FHWA (Wu et al. 2012), the percentages of the total hours for each representative traffic condition to occur for a typical year can be quantified, which are shown in Table 5.3. Specifically, the probability of occurrence of free flow, moderate flow

and busy flow is 48.31%, 44.55% and 7.14%, respectively. The cumulative fatigue damage factor for each typical year can then be calculated for each representative corrosion and Road roughness condition with taking into account the combination of each representative traffic condition (T_i) “Free, Moderate and Congested”. Finally, the cumulative damage factor for each particular joint has been calculated along the service life of the bridge, by linearly adding the cumulative damage factor for each typical year of each of the representative corrosion condition (C_i) “No corrosion, light corrosion, Medium corrosion and Sever corrosion” and Road roughness conditions. Table 5.4 shows the cumulative damage factor for each typical year of each of the representative corrosion and road roughness conditions. It is clear that the cumulative damage factor for each typical year increases slightly as the conditions of road roughness and corrosion deteriorate over time. This shows the combined effect of increasing surface roughness and steel rebar reduction due to corrosion on fatigue damage can be pretty significant. For example, as compared to the bridge deck in the first 1-5 years of service with “very good” roughness and “no-light” corrosion, cumulative fatigue damage factor of the bridge deck after 10 or more years of service with “average” roughness and “severe” corrosion can increase by 4 to 5 times.

Figures 5.18 to 5.37 show the fatigue damage index surfaces of different bridge deck nodes under different vehicle densities, corrosion conditions and the road roughness scenarios, as well as the cumulative damage factors versus service life for all of the joints chosen in this study. For nodes #899, #1232 and #1580, fatigue damage index generally increases with traffic density and corrosion severity. For nodes #1211, #1241, #1247, #1554, #1559, and #1226, fatigue damage index changes over traffic density in a more complex way: the highest fatigue damage index occurs at moderate traffic density, not in the highest traffic density. For node #914, when corrosion severity is low, fatigue damage index increases with traffic density. When corrosion

severity increases, fatigue damage index increases with traffic density first and then starts to decrease. Over years, the cumulative fatigue damage indices gradually increase. However, the cumulative fatigue damage indices show large variations among different nodes. To achieve 1.0 cumulative fatigue damage index, different deck elements will take different time periods. For example, node #1211 takes about 1.15 years, node #1559 takes 4.5 years, node #1226 takes 6 years, node #1544 takes about 7 years and #914 and #1241 take about 10 years. Node #1580 takes about 20 years and other nodes such as #1232 and #899 will not achieve unit cumulative fatigue damage index within 20 years. Table 5.1 lists all the required years to achieve unit cumulative fatigue damage index for different nodes.

Table 5.1 : Fatigue life for each node of the four elements chosen in this study (years).

Joint #	Number of years to reach unity
1544	6.9818
1559	4.424
1574	2.75
1580	19.739
1211	1.15
1226	6.153
1241	10.444
899	55.25
914	9.598
1232	33.619
1247	16.6314

Table 5.2: Hourly fatigue damage factors (DF_i) for each joint of the four elements chosen for each particular scenario

Road Roughness	Corrosion Conditions	Traffic Flow Conditions (Joint #1544)		
		Light	Moderate	Heavy
Very-Good	No	2.7670e-06	1.2061e-05	8.9717e-06
	Light	2.6537e-06	2.1141e-05	5.8237e-06
Good	Medium	5.8184e-06	6.3269e-05	4.0941e-06
Average	Severe	7.2125e-06	8.1450e-05	5.2844e-06
Road Roughness	Corrosion Conditions	Traffic Flow Conditions (Joint #1559)		
		Light	Moderate	Heavy
Very-Good	No	7.5028e-06	2.6045e-05	1.5564e-05
	Light	6.5432e-06	5.2704e-05	2.6225e-05
Good	Medium	1.1990e-05	1.1982e-04	8.8329e-06
Average	Severe	4.2055e-05	3.1589e-04	3.2191e-05
Road Roughness	Corrosion Conditions	Traffic Flow Conditions (Joint #1565)		
		Light	Moderate	Heavy
Very-Good	No	5.2408e-06	8.4602e-05	9.6405e-05
	Light	6.2037e-06	1.5591e-04	6.6098e-05
Good	Medium	5.7645e-06	4.9791e-05	1.7754e-05
Average	Severe	7.8891e-06	2.2524e-04	2.4257e-04
Road Roughness	Corrosion Conditions	Traffic Flow Conditions (Joint #1574)		
		Light	Moderate	Heavy
Very-Good	No	1.2927e-05	4.9810e-05	3.7891e-05
	Light	9.9706e-06	9.0093e-05	3.1682e-05
Good	Medium	2.0723e-05	2.0195e-04	2.0909e-05
Average	Severe	3.6782e-05	4.5169e-04	4.7152e-05
Road	Corrosion	Traffic Flow Conditions (Joint #1580)		

Roughness	Conditions	Light	Moderate	Heavy
Very-Good	No	5.2887e-07	6.9882e-06	2.0301e-05
	Light	5.8610e-07	1.0730e-05	1.1915e-05
Good	Medium	4.0128e-07	3.9730e-06	8.9819e-06
Average	Severe	1.5485e-06	1.1218e-05	2.3521e-05
Road Roughness	Corrosion Conditions	Traffic Flow Conditions (Joint #1211)		
		Light	Moderate	Heavy
Very-Good	No	2.2368e-05	1.5818e-04	7.6323e-05
	Light	1.8991e-05	3.8280e-04	5.4841e-05
Good	Medium	3.4472e-05	2.9692e-04	7.0712e-05
Average	Severe	5.4625e-05	6.8459e-04	8.1582e-05
Road Roughness	Corrosion Conditions	Traffic Flow Conditions (Joint #1226)		
		Light	Moderate	Heavy
Very-Good	No	4.8789e-06	1.6427e-05	7.7041e-06
	Light	3.5101e-06	3.6217e-05	8.1393e-06
Good	Medium	6.8015e-06	5.0176e-05	4.9716e-06
Average	Severe	9.6592e-06	7.5429e-05	9.5723e-06
Road Roughness	Corrosion Conditions	Traffic Flow Conditions (Joint #1241)		
		Light	Moderate	Heavy
Very-Good	No	1.4498e-06	5.2215e-06	2.1914e-06
	Light	1.3690e-06	8.3390e-06	1.8862e-06
Good	Medium	3.2470e-06	3.3735e-05	2.7046e-06
Average	Severe	3.3212e-06	3.9509e-05	3.8056e-06
Road Roughness	Corrosion Conditions	Traffic Flow Conditions (Joint #899)		
		Light	Moderate	Heavy
Very-Good	No	4.3921e-07	1.4366e-06	2.1914e-06

	Light	4.7453e-07	2.2547e-06	1.3435e-06
Good	Medium	3.7637e-07	1.2949e-06	4.7307e-07
Average	Severe	6.5485e-07	3.7454e-06	4.2514e-06
Road Roughness	Corrosion Conditions	Traffic Flow Conditions (Joint #914)		
		Light	Moderate	Heavy
Very-Good	No	3.3305e-06	1.3459e-05	2.2130e-05
	Light	3.9686e-06	1.8876e-05	1.6499e-05
Good	Medium	5.6585e-06	2.0805e-05	1.0307e-05
Average	Severe	7.9231e-06	2.8156e-05	3.5618e-05
Road Roughness	Corrosion Conditions	Traffic Flow Conditions (Joint #1232)		
		Light	Moderate	Heavy
Very-Good	No	5.9709e-07	3.0937e-06	3.1596e-06
	Light	6.2378e-07	4.3631e-06	4.3985e-06
Good	Medium	6.6373e-07	1.8383e-06	4.0824e-06
Average	Severe	8.6461e-07	4.5415e-06	5.1856e-06
Road Roughness	Corrosion Conditions	Traffic Flow Conditions (Joint #1247)		
		Light	Moderate	Heavy
Very-Good	No	1.0508e-06	6.1288e-06	1.6405e-06
	Light	1.3690e-06	8.7644e-06	6.9473e-06
Good	Medium	1.5478e-06	6.4048e-06	2.1565e-06
Average	Severe	3.6487e-06	1.1458e-05	5.4821e-05

Table 5.3: Total hours for each representative traffic condition to occur in each year

Traffic Condition	Total hours per year	Probability of occurrence %
Free flow (T_i)	4244	48.31
Moderate flow (T_i)	3913	44.55
Congested flow (T_i)	627	7.14

Table 5.4 the cumulative damage factor for each typical year of each of the representative corrosion conditions

Road Roughness	Corrosion Conditions	Joint #1544
		cumulative damage factor per typical year
Very-Good	No	6.46E-02
	Light	9.76E-02
Good	Medium	2.75E-01
Average	Severe	3.53E-01
Road Roughness	Corrosion Conditions	Joint #899
		cumulative damage factor per typical year
Very-Good	No	8.86E-03
	Light	1.17E-02
Good	Medium	6.96E-03
Average	Severe	2.01E-02
Road Roughness	Corrosion Conditions	Joint #1232
		cumulative damage factor per typical year
Very-Good	No	1.66E-02
	Light	2.25E-02

Good	Medium	1.26E-02
Average	Severe	2.47E-02
Road Roughness	Corrosion Conditions	Joint #1241
		cumulative damage factor per typical year
Very-Good	No	2.80E-02
	Light	3.96E-02
Good	Medium	1.47E-01
Average	Severe	1.71E-01
Road Roughness	Corrosion Conditions	Joint #1247
		cumulative damage factor per typical year
Very-Good	No	2.95E-02
	Light	4.45E-02
Good	Medium	3.30E-02
Average	Severe	9.47E-02
Road Roughness	Corrosion Conditions	Joint #1580
		cumulative damage factor per typical year
Very-Good	No	4.23E-02
	Light	5.19E-02
Good	Medium	2.29E-02
Average	Severe	6.52E-02
Road Roughness	Corrosion Conditions	Joint #1559
		cumulative damage factor per typical year
Very-Good	No	1.44E-01
	Light	2.50E-01
Good	Medium	5.25E-01
Average	Severe	1.43E+00

Road Roughness	Corrosion Conditions	Joint #914
		cumulative damage factor per typical year
Very-Good	No	8.07E-02
	Light	1.01E-01
Good	Medium	1.12E-01
Average	Severe	1.66E-01
Road Roughness	Corrosion Conditions	Joint #1226
		cumulative damage factor per typical year
Very-Good	No	8.98E-02
	Light	1.62E-01
Good	Medium	2.28E-01
Average	Severe	3.42E-01
Road Roughness	Corrosion Conditions	Joint #1211
		cumulative damage factor per typical year
Very-Good	No	7.62E-01
	Light	1.61E+00
Good	Medium	1.35E+00
Average	Severe	2.96E+00
Road Roughness	Corrosion Conditions	Joint #1574
		cumulative damage factor per typical year
Very-Good	No	2.74E-01
	Light	4.15E-01
Good	Medium	8.91E-01
Average	Severe	1.95E+00

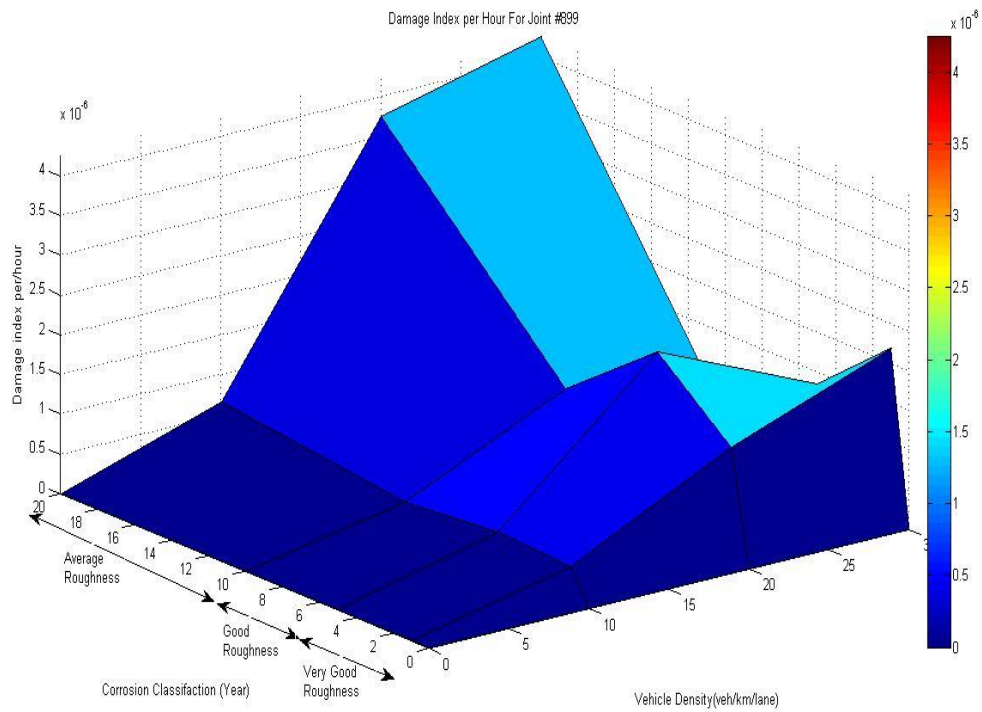


Figure 5.18 Fatigue damage index surface under different vehicle densities and corrosion effects for joint #899



Figure 5.19 Cumulative damage facto versus service life for joint #899

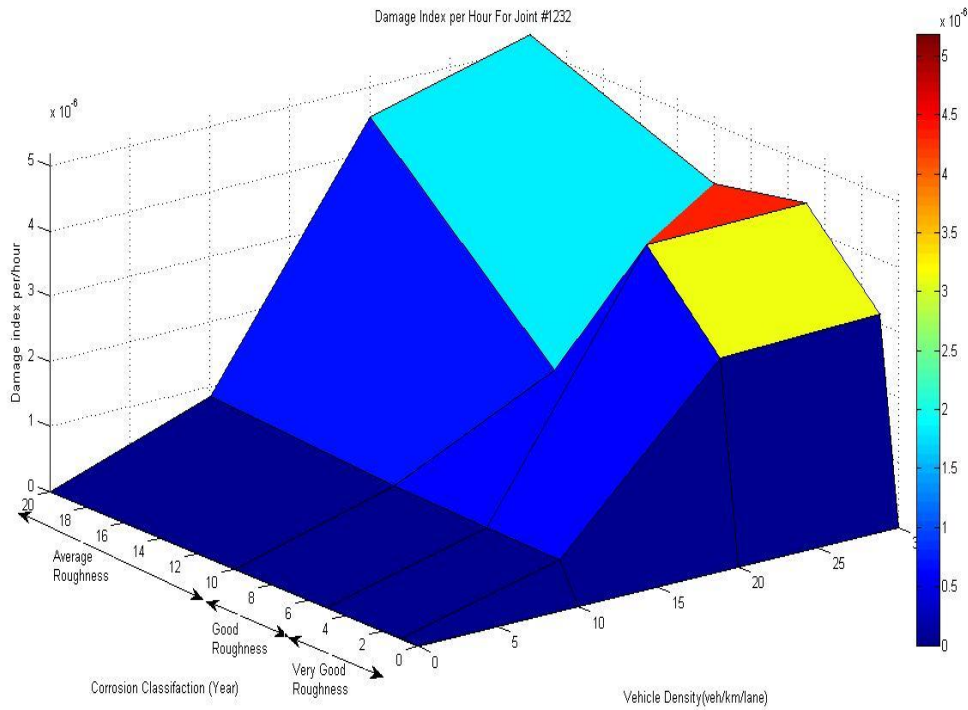


Figure 5.20 Fatigue damage index surface under different vehicle densities and corrosion effects for joint #1232

for joint #1232

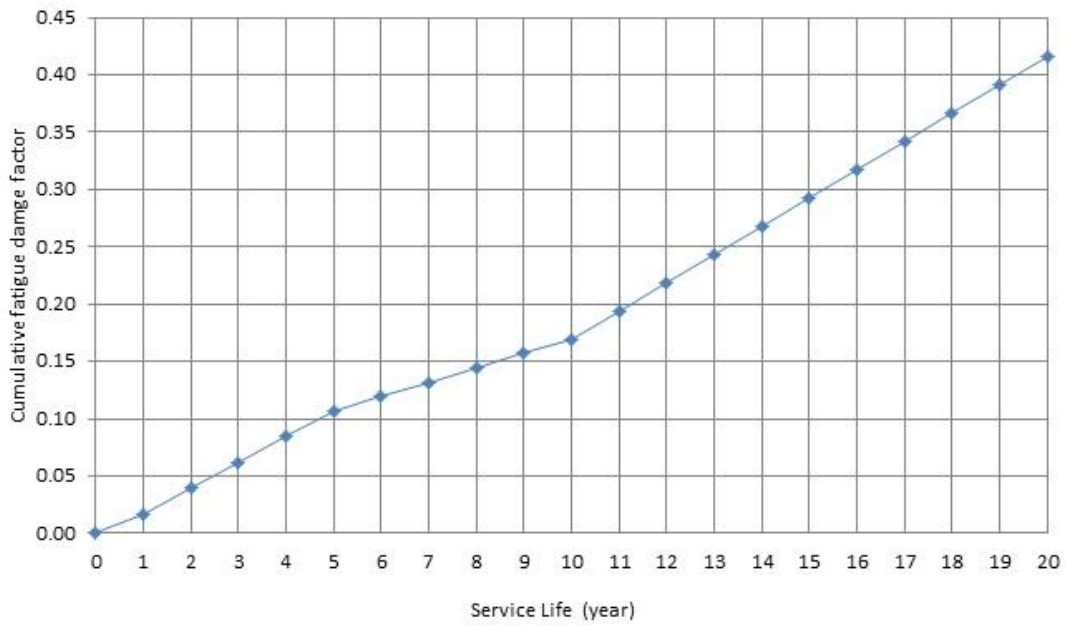


Figure 5.21 Cumulative damage facto versus service life for joint #1232

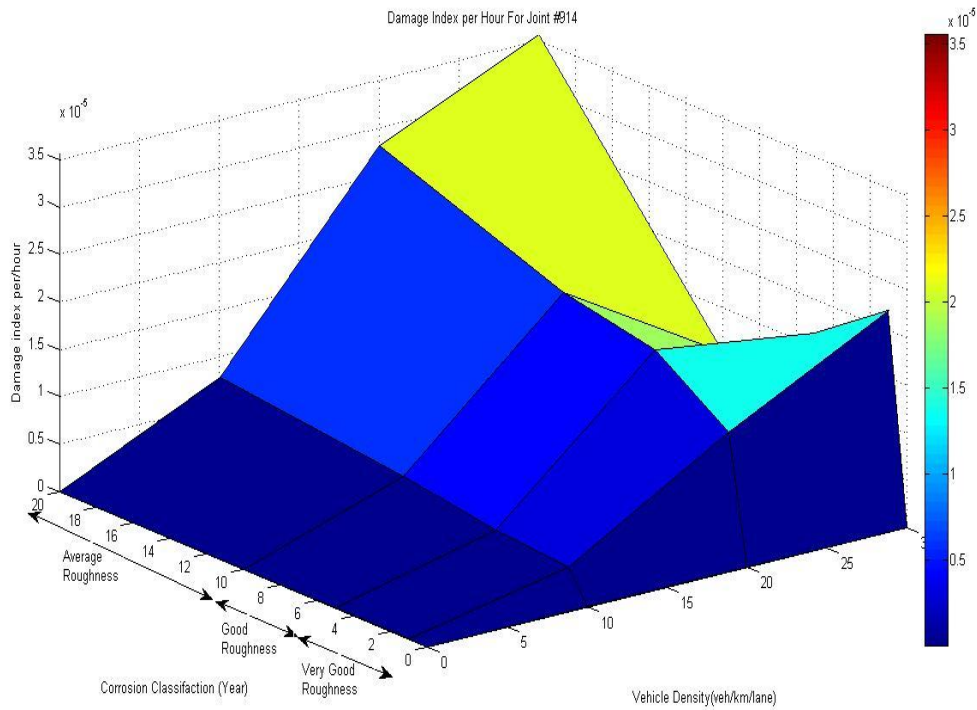


Figure 5.22 Fatigue damage index surface under different vehicle densities and corrosion effects for joint #914

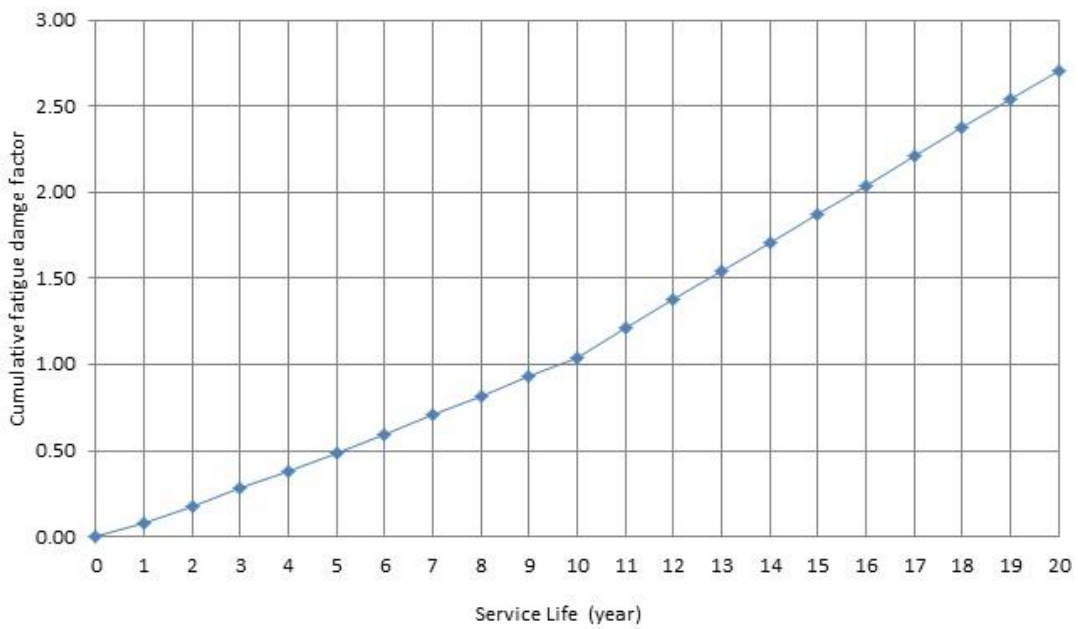


Figure 5.23 Cumulative damage facto versus service life for joint #914

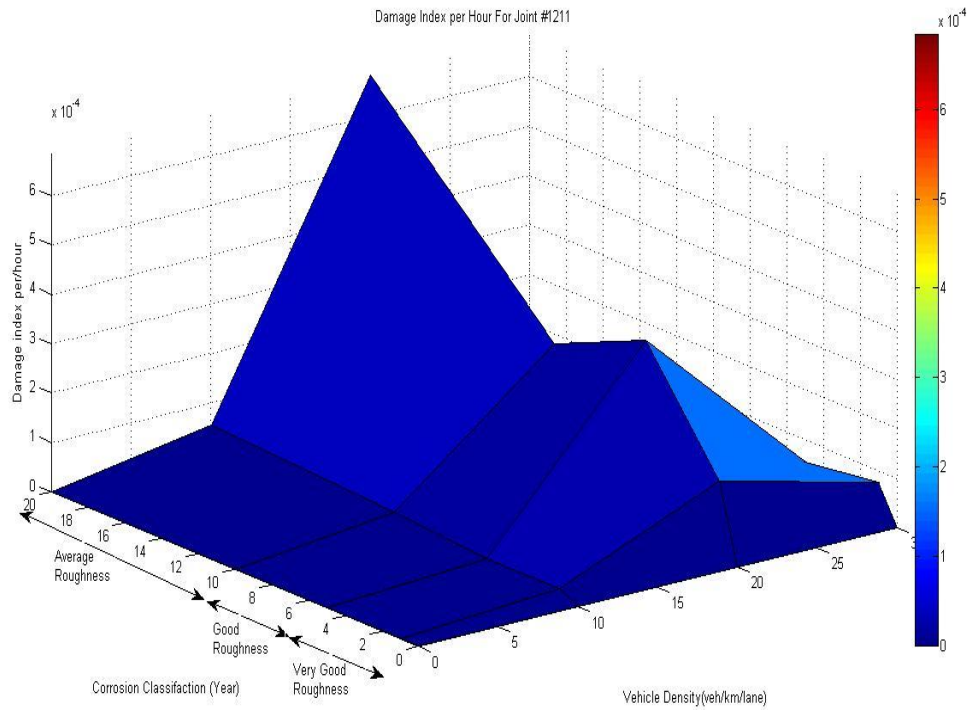


Figure 5.24 Fatigue damage index surface under different vehicle densities and corrosion effects for joint #1211

for joint #1211

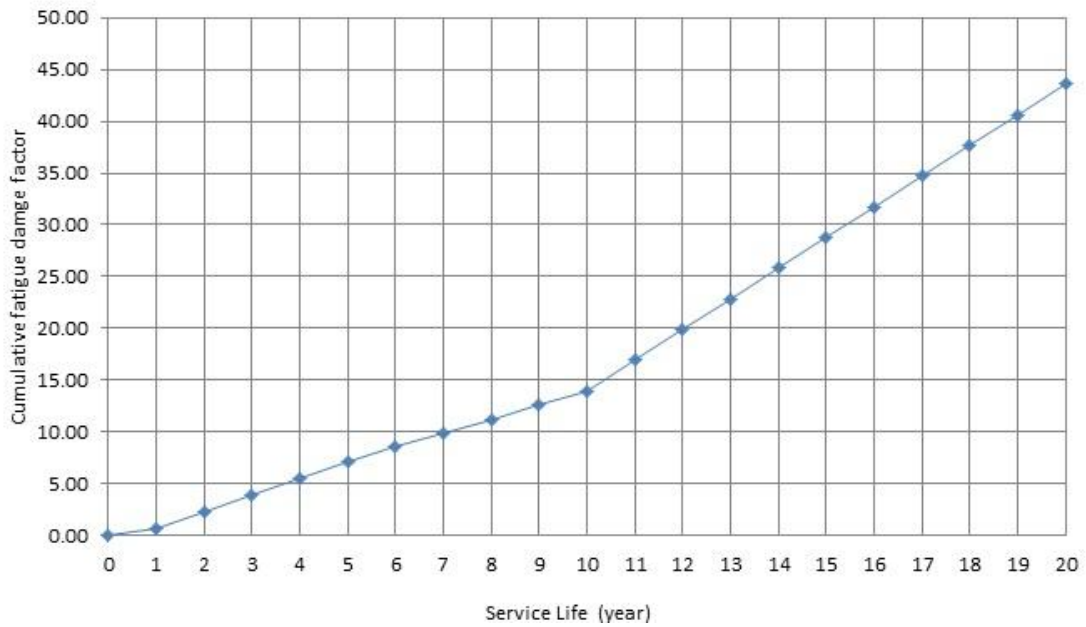


Figure 5.25 Cumulative damage facto versus service life for joint #1211

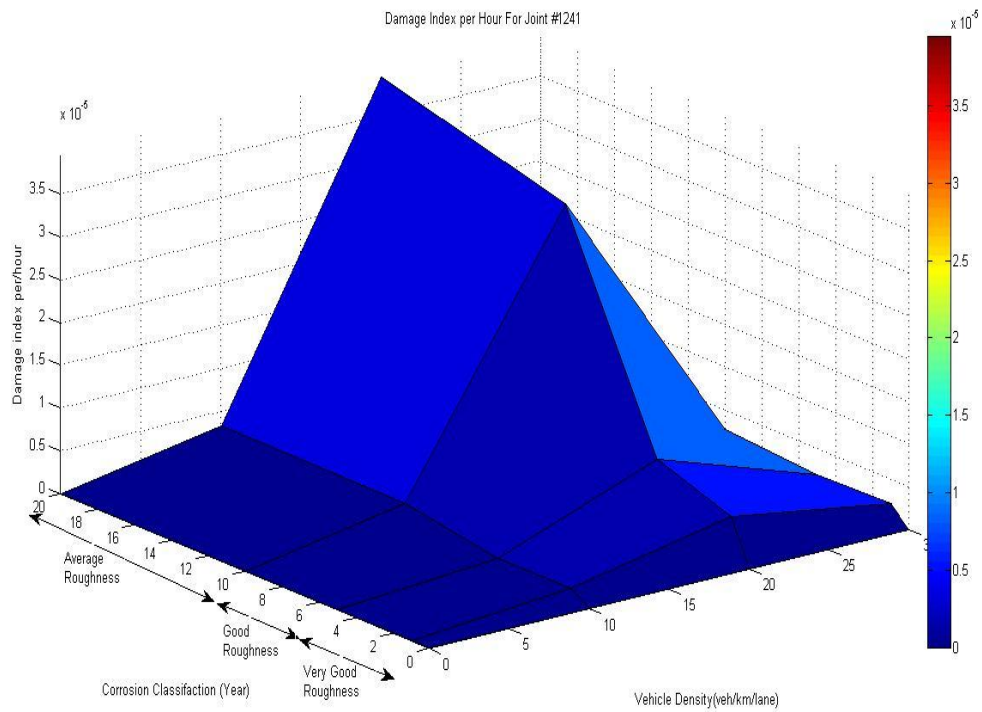


Figure 5.26 Fatigue damage index surface under different vehicle densities and corrosion effects for joint #1241



Figure 5.27 Cumulative damage facto versus service life for joint #1241

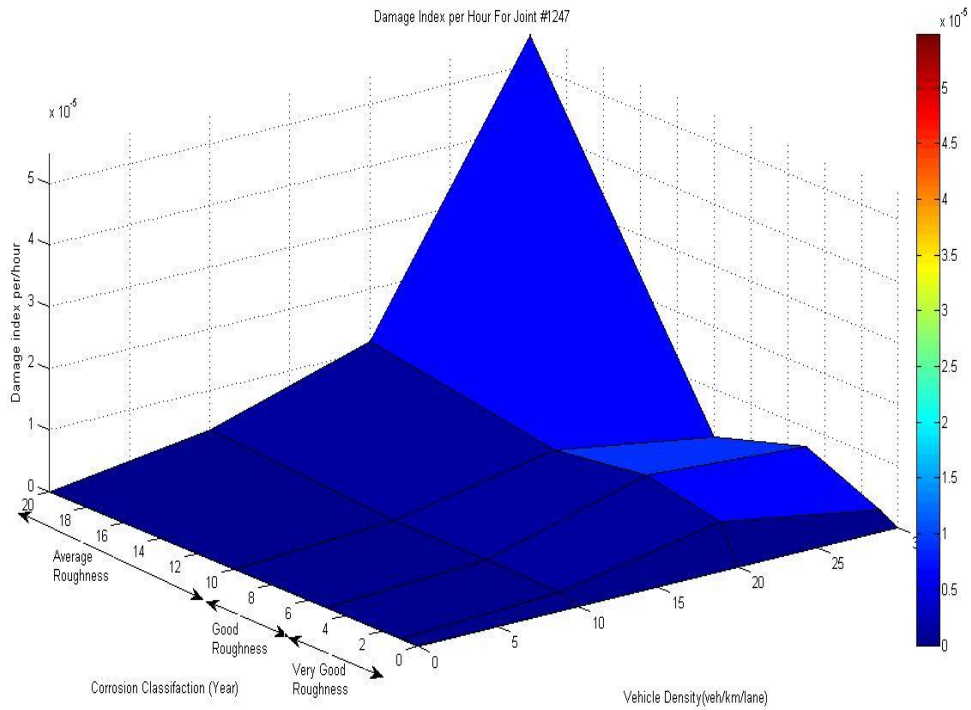


Figure 5.28 Fatigue damage index surface under different vehicle densities and corrosion effects for joint #1247



Figure 5.29 Cumulative damage facto versus service life for joint #1247

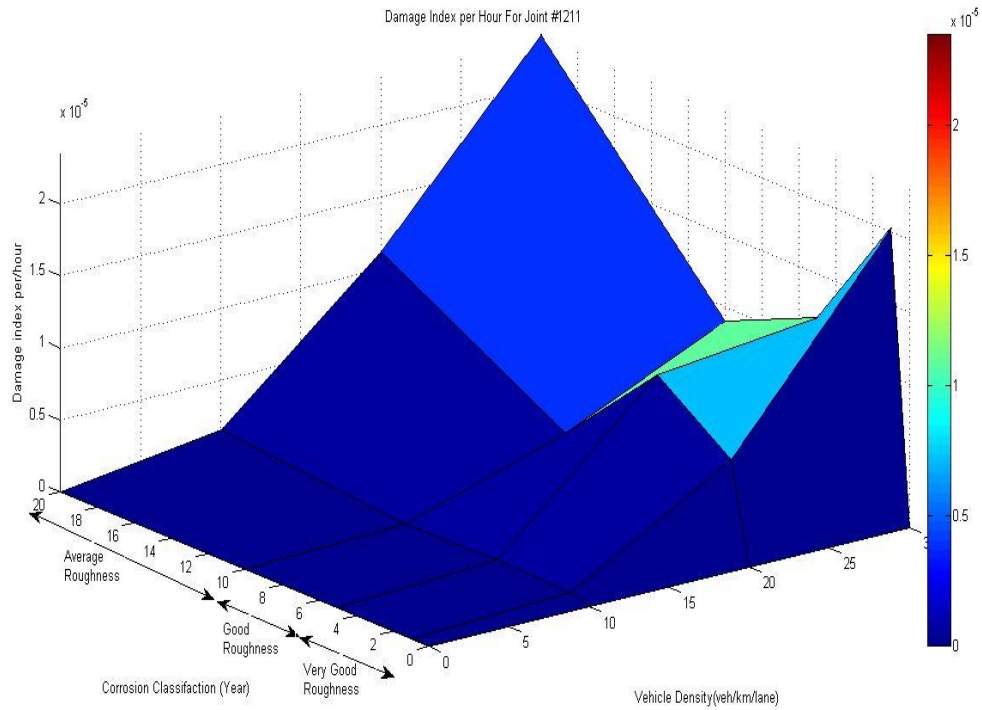


Figure 5.30 Fatigue damage index surface under different vehicle densities and corrosion effects for joint #1580

for joint #1580

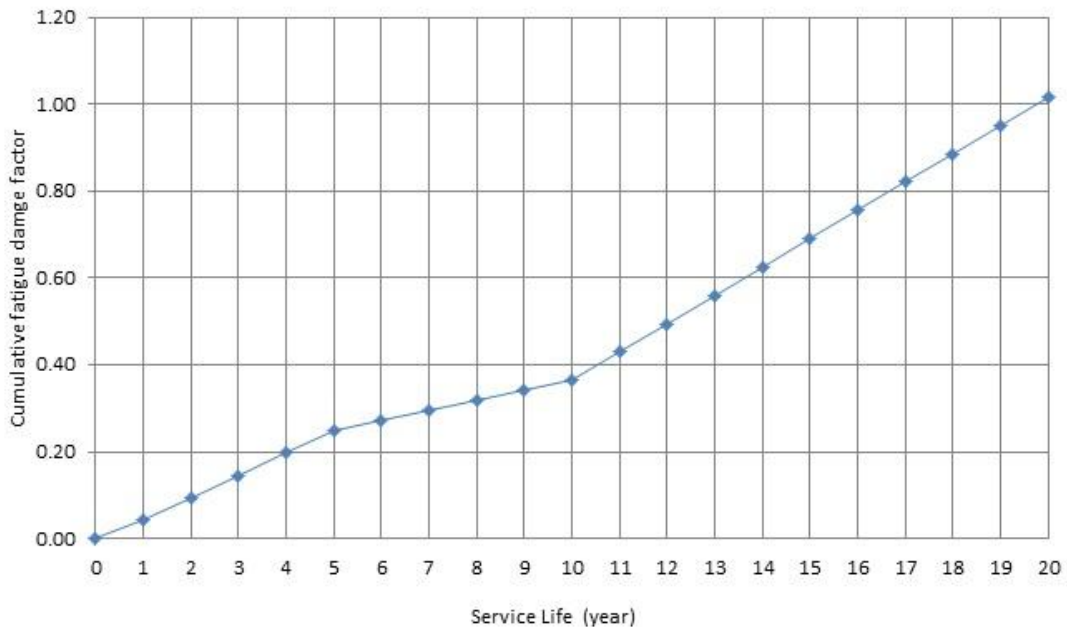


Figure 5.31 Cumulative damage facto versus service life for joint #1580

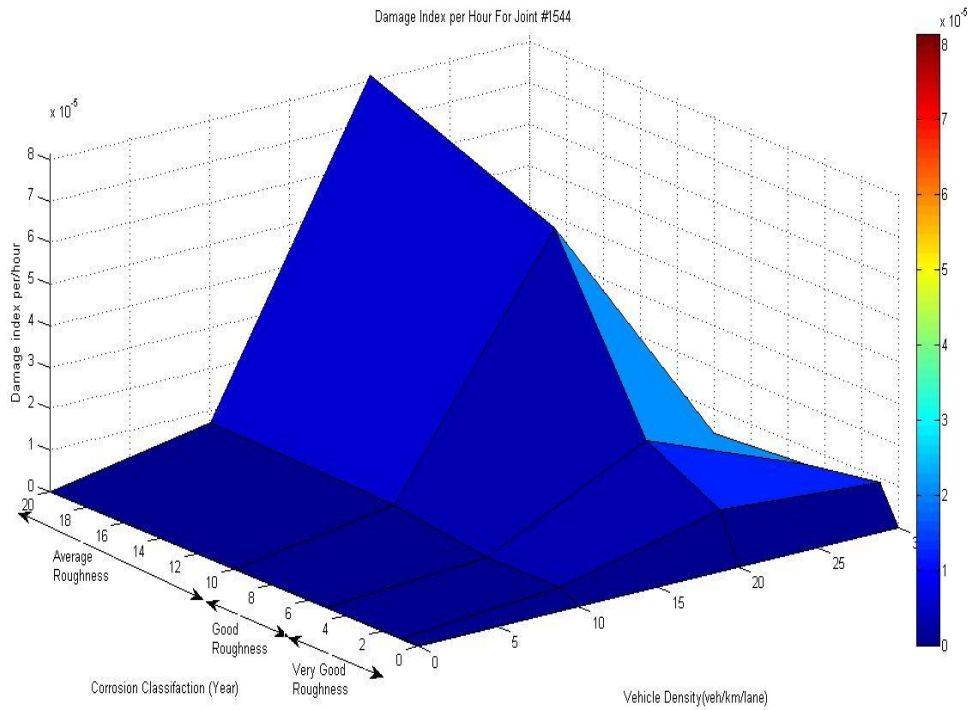


Figure 5.32 Fatigue damage index surface under different vehicle densities and corrosion effects for joint #1544



Figure 5.33 Cumulative damage facto versus service life for joint #1544

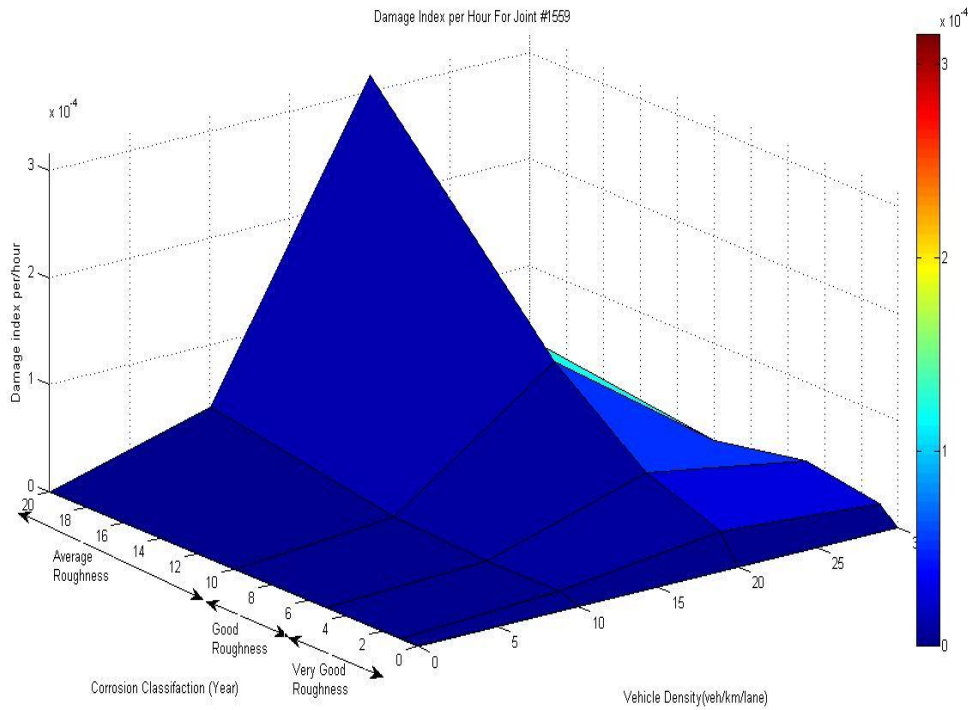


Figure 5.34 Fatigue damage index surface under different vehicle densities and corrosion effects for joint #1559

for joint #1559

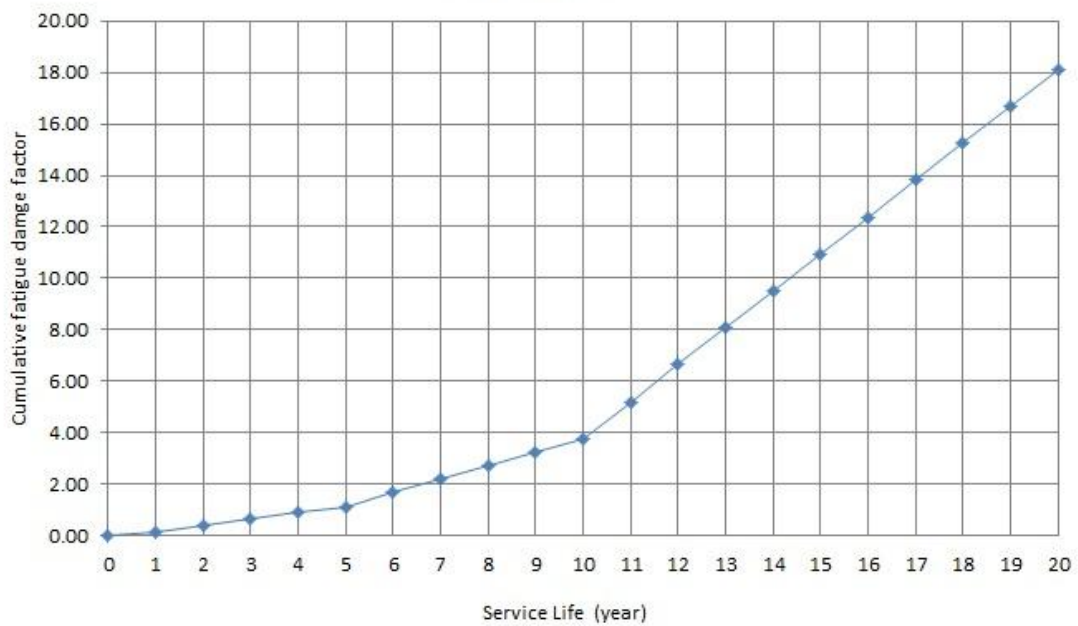


Figure 5.35 Cumulative damage facto versus service life for joint #1559

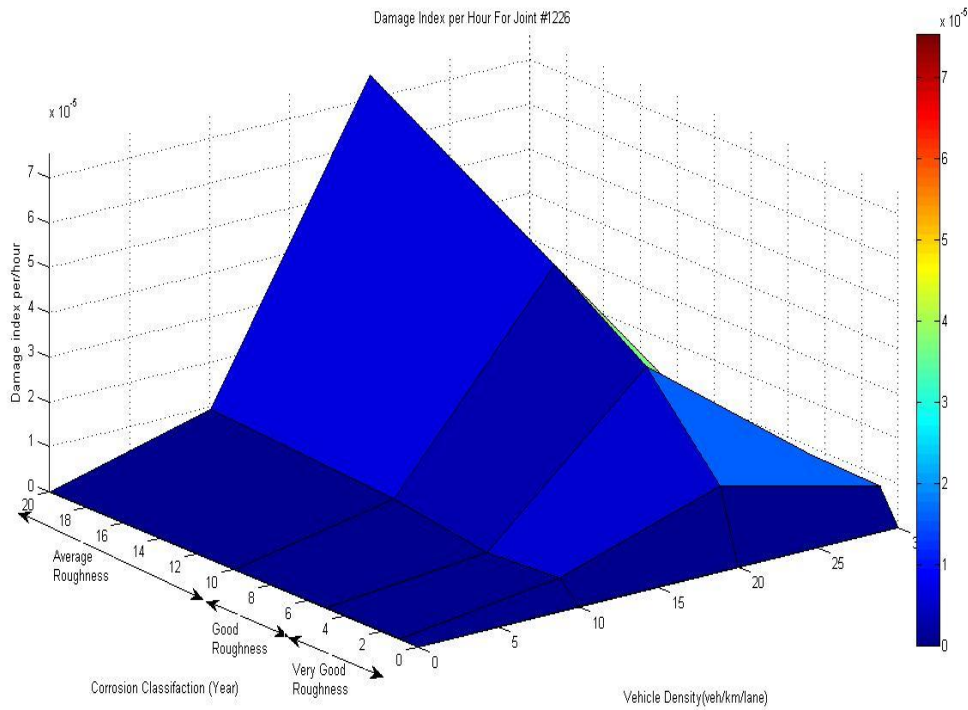


Figure 5.36 Fatigue damage index surface under different vehicle densities and corrosion effects for joint #1226

for joint #1226

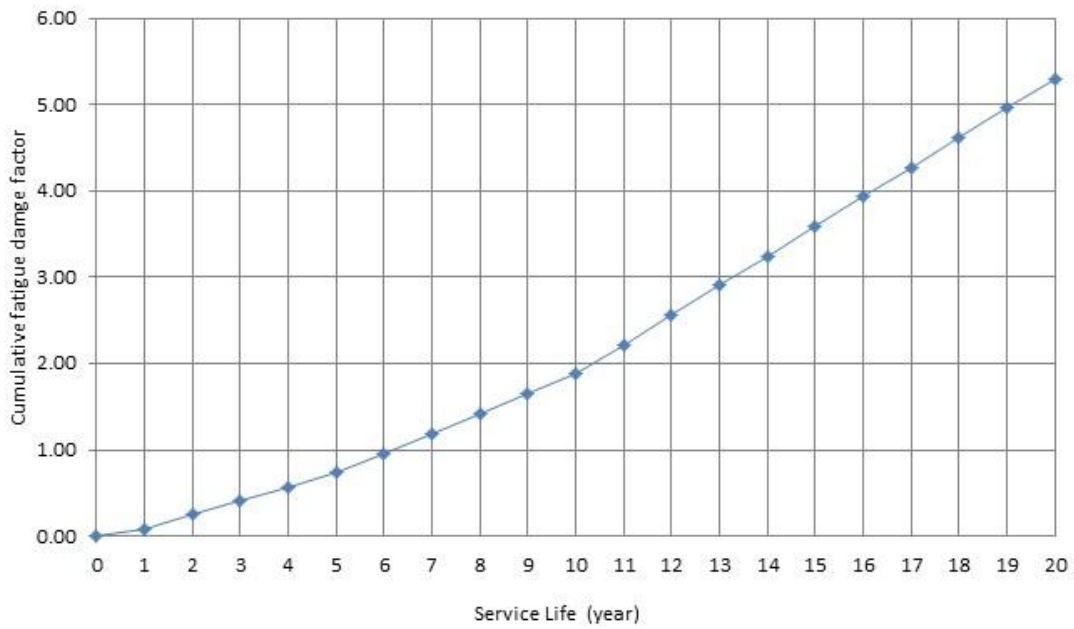


Figure 5.37 Cumulative damage facto versus service life for joint #1226

Chapter 6: Conclusion

The present study investigates the effect of reinforcing steel corrosion and road surface deterioration on short slabs bridges decks' dynamic response caused by moving vehicles. A hybrid analytical method was introduced which includes a reduced-DOF model and a refined FEM model. The reduced-DOF model is to simulate the actual wheel load from stochastic traffic considering dynamic interactions between vehicles, bridge and roughness level. Three categories of traffic vehicles have been adopted along with three road surface roughness and four corrosion conditions. The refined-scale FEM model based on SAP2000 was developed to study the dynamic stress of bridge deck. Time-progressive analysis was conducted to consider the time-dependent deck roughness change and steel rebar dimension reduction caused by corrosion. As a result, the stress ranges and the number of stress ranges cycles have been obtained in time domain for different representative scenarios and the fatigue damage index was assessed. The life-time fatigue performance of different bridge deck nodes are made. Following conclusions can be drawn:

1-The traffic rates clearly affect the dynamic performances of short slab bridges. When the traffic rate increases, higher resultant stresses ranges will be induced. Based on this study, heavy and moderate traffic conditions induce more damage indexes than those from light traffic conditions.

2-Heavy traffic rates do not always introduce stress-ranges cycles larger than those introduced from moderate traffic rates. Consequently, the heavy traffic flow is not necessary introduce the largest fatigue damage indexes per hour.

3-The road surface roughness condition affects the dynamic performance of short slab bridges. Based on this study, the more deteriorated road surface conditions, the larger stress ranges and number of stress ranges cycles for each truck passage will be introduced. Consequently, the more deteriorated road surface condition will introduce larger fatigue damage indexes per hour.

4-The corrosion of the reinforcement bars of the bridge decks influences the fatigue life of the short span bridge decks. The corrosion of reinforcement bars will introduce larger stress range and more stress-ranges cycles per hour will be introduced. As a result, the fatigue damage indexes per hour will increase with the increase of the percentage of steel bars affected by corrosion.

In order to get better understanding of the effect of the corrosion and road roughness based-scenario in future studies, some limitations of the present study and future directions are discussed:

1-In this study, the uniform corrosion model has been adopted to calculate the decrease of the diameter during the propagation stage of corrosion. This approach has been adopted because of its simplicity. The use of other improved corrosion models can be adopted for further work on this field.

2-This study provides deterministic analytical framework to consider the joint effect from corrosion and traffic. Reliability-based analysis may be conducted in the future to consider various uncertainties.

3-In this study, general road roughness variation model over time was adopted to indirectly consider the effect of corrosion. Once a more advanced model linking roughness and corrosion is available, more realistic estimation of the bridge deck performance can be expected.

Bibliography

- American Society for Testing and Materials. (2011). Standard Practices for Cycle Counting in Fatigue Analysis. E1049 – 85.
- National Research Council . (2000). Highway Capacity Manual.
- A.D. Pelton, T. E. (1972). Analytical Solution of Fick's Second law when the Diffusion Coefficient Varies Directly as Concentration. *Acta Metallurgica*, 20(11), 1269.
- ASTM. (1985). Standard Practices for Cycle Counting in Fatigue Analysis. American Society for Testing and Materials Standard .
- Baboian, R. (2005). Corrosion Tests And Standards: Application And Interpretation (Vol. 20). ASTM International.
- Bamforth, P. B. (1999). The Derivation of Input Data for Modelling Chloride Ingress from Eight-year UK Coastal Exposure Trials. *Magazine of Concrete Research*, 51(2), 87 –96.
- Bazant, H. O. (1983). Uncertainty Analysis of Creep and Shrinkage Effects in Concrete structures. *ACI*, 80(2), 116.
- Bazant, Z. P. (1979). Physical Model for Steel Corrosion in Sea Structures Theory. *Journal of the Structural Division*, 105(6), 1137-1153.
- Bond, A., & Harris, A. (2008). Decoding Eurocode 7.
- Cai, C. C., & Chen, S. (2004). Framework of Vehicle–Bridge–Wind Dynamic Analysis. *Journal of Wind Engineering and Industrial Aerodynamics*, 92(7-8), 579–607.
- Chen, S. R., & Cai, C. S. (2007). Equivalent wheel load Approach for Slender Cable-Stayed Bridge Fatigue Assessment under Traffic and Wind: Feasibility Stud. *J. Bridge Eng*, 12(6), 755–764.
- Chen, S. R., & Wu, J. (2010). Dynamic Performance Simulation of Long-Span Bridge under Combined Loads of Stochastic Traffic and Wind. *J. Bridge Eng*, 15(3), 219–230.
- Chen, S., & Wu, J. (2011). Modeling Stochastic Live Load for Long-Span Bridge Based on Microscopic Traffic Flow Simulation. *Computers & Structures*, 89(9-10), 813–824.
- Dimitri V. Val, M. G. (2003, October). Life-cycle Cost Analysis of Reinforced Concrete Structures in Marine Environments. *Structural Safety*, 25(4), 343-362.
- DuraCrete. (2000). Statistical Quantification of the Variables in the Limit State Functions. Project No.BE95-1347: The European Union - Brite EuRam III,.

- Feldmann, G. C. (2008). Concrete Repair Basics. From Structural Practices:
<http://www.structuremag.org/article.aspx?articleid=590>
- Guo, G. (2006). Laboratory and Field Tests of Multiple Corrosion Protection Systems for Reinforced Concrete Bridge Components and 2205 Pickled Stainless Steel. Lawrence, Kansas, University of Kansas Center for Research, Inc: ProQuest.
- High-Cycle Fatigue (HCF) Testing. Retrieved 2012 14-feb from MTS Systems Corporation:
<http://www.mts.com/en/products/application/materials-testing/metals/high-cycle-fatigue/index.htm>
- International Standard Organization. (1995). Mechanical Vibration - Road Surface Profiles - Reporting of Measured Data. Geneva: ISO 8608.
- J. G. MacGregor, S. A. (1983). Statistical Analysis of Resistance of Reinforced and Prestressed Concrete Members. *ACI*, 80(3), 167-176.
- Khatri, R., & Sirivivatnanon, V. (2004). Characteristic Service Life for Concrete Exposed to Marine Environments. *Cement and Concrete Research*, 34(5), 745–752.
- Koch, G., P.H.Brongers, M., & Neil G, T. (2002). Corrosion Costs and Preventive Strategies in the United States. Federal Highway Administration FHWA-RD-01-156.
- LeRose, C. (2001). The Collapse of the Silver Bridge. *West Virginia Historical Society Quarterly*, 15(4).
- Li, C. Z., J., L., W., & Melchers, R. (2007). Concrete Delamination Caused by Steel Reinforcement Corrosion. *JOURNAL OF MATERIALS IN CIVIL ENGINEERING*, 19(7), 591.
- Liu, Y. (1996). Modeling the Time-to Corrosion Cracking of the Cover Concrete in Chloride Contaminated Reinforced Concrete Structures. Dissertation.
- Lonaker, T. (2006). Silver Bridge Collapse. Retrieved from The Long Day:
<http://www.freewebs.com/silverbridgeaccident/thebridgecollapse.htm>
- Lounis, G. M. (2003). A New Approach to Programming Maintenance Activities for Concrete Bridge Decks. National Research Council Canada.
- M. Masi, D. C. (1997). Simulation of Chloride Penetration in Cement-Based Materials. *Cement and Concrete Research*, 27(10), 1591-1601.
- M.G. Stewart, J. M. (2007). Spatial Time-Dependent Reliability Analysis of Corrosion Damage and the Timing of First Repair for RC Structures. *Engineering Structures*, 29(7), 1457–1464.

- Maaddawy, T. E., & Soudki, K. (2007). A Model for Prediction of Time from Corrosion Initiation to Corrosion Cracking. *Cement and Concrete Composites*, 29(3), 168–175.
- Mangat, P. S., & Molloy, B. T. (1994, July). Prediction of Long Term Chloride Concentration in Concrete. *Materials and Structures*, 27(6), 338-346.
- Maymon, G. (1998). *Some Engineering Applications in Random Vibrations and Random Structures* (Vol. 178). American Institute of Aeronautics and Astronautics.
- Mazzolani, F. M. (2000). *Moment Resistant Connections of Steel Frames in Seismic Areas: Design and Reliability*. (1, Ed.) London: E & FN SPON.
- Mullard, J. A., & Stewart, M. G. (2009). *Corrosion-Induced Cover Cracking of RC Structures: New Experimental Data and Predictive Models*. University of Newcastle.
- Mullard, J., & Stewart, M. (2009). Stochastic Assessment of Timing and Efficiency of Maintenance for Corroding RC Structures. *Journal of Structural Engineering*, 135(8), 887–895.
- Nagel, K., & Schreckenberg, M. (1992). A Cellular Automaton Model for Freeway Traffic. *J. Phys. I France* , 2221-2229.
- Nasvik, J. (2003). *Rehabilitation for Our Nation's Bridges: Maintaining Bridges is no Small Task. Here's How We Make Decisions About Repair and Technology That Will Help them Last Longer*. Concrete Construction.
- Neville, A. M. (1996). *Properties of Concrete* (4, illustrated ed.). John Wiley & Sons.
- Oh, B., Lew, Y., & Choil, Y. (2007). Realistic Assessment for Safety and Service Life of Reinforced Concrete Decks in Girder Bridges. *Journal Of Bridge Engineering*, 12(7), 410.
- Oshima, Y., & Sugiura, K. (2008). Fatigue Life Estimation of a Concrete Slab Using B-WIM and Traffic Census. In B. Jacob, E. O'Brien, & P. Nordengen (Ed.), *International Conference on Heavy Vehicle* (pp. 359-368). Paris: John Wiley & Sons.
- Otieno, M., Beushausen, H., & Alexander, M. (2011). *Prediction of Corrosion Rate in Reinforced Concrete Structures – A Critical Review and Preliminary Results*. Cape Town / South Africa: Department of Civil Engineering, University of Cape Town.
- Papadakis, G., Fardis., N., & Vayenas., G. (1992). Effect of Composition, Environmental Factors and Cement-Lime Mortar Coating on Concrete Carbonation. *Materials and Structures*, 25, 293-304.

- Rigo, A. .. (2011). Scantling Optimization of Ship Structures Considering Fatigue at the Early Design Stage. *Advances in Marine Structures*, 569–579.
- Rosowsky, M. G. (1998). Time-dependent Reliability of Deteriorating Reinforced. *Structural Safety*, 20(1), 91-109.
- Rychlik, I. (1987). A New Definition of the Rainflow Cycle Counting Method. *International Journal of Fatigue*, 9(2), 119-121.
- S. Yehia, Y. T. (1998). Bridge Deck Deicing Crossroads 1998–2000 Transportation Conference (pp. 34–39). Iowa State University .
- Schläfli, M., & Brühwiler, E. (1998). Fatigue of Existing Reinforced Concrete Bridge Deck Slabs. *Engineering Structures*, 20(11), 991-998.
- SCHLITZ, W. (1996). A History of Fatigue. *Engineering Fracture Mechanics*, 54(2), 263–300.
- Scott, A. N. (2004). The Influence of Binder Type and Cracking on Reinforcing Steel Corrosion in Concrete. PhD Thesis. Cape Town: University of Cape Town.
- Shi, X., Cai, C. S., & Chen, S. (2008). Vehicle Induced Dynamic Behavior of Short-Span Slab Bridges Considering Effect of Approach Slab Condition. *Journal of Bridge Engineering*, 13(1), 83-92.
- Siemes, A. J. (1982). Miner's Rule with Respect to Plain Concrete Variable Amplitude Tests. *ACI* , 75, 343-372.
- Socie, S. D., & Downing, F. D. (1982). Simple Rainflow Counting Algorithms. *International Journal of Fatigue*, 4(1), 31-40.
- Stewart, J. A. (2009). Stochastic Assessment of Timing and Efficiency of Maintenance for Corroding RC Structures. *Journal of Structural Engineering* , 135(8), 887–895.
- Stewart, M. G., & Al-Harthy, A. (2008). Pitting Corrosion and Structural Reliability of Corroding RC Structures: Experimental Data and Probabilistic Analysis. *System Safety*, 93(3), 373-382.
- Sugaira, Y. O., & Kunitomo. (2008). Fatigue life Estimation of a Concrete Slab Using. BWIM and Traffic census. *International Conference on Heavy Vehicles*. Paris.
- Tanaka, Y., Murakoshi, J., & Nagaya, Y. (2009). Fatigue and Corrosion in Concrete Decks with Asphalt Surfacing. *Proceedings of the 25th U.S. – JAPAN Bridge Engineering Workshop*, (pp. 219-232). Tsukuba, Japan.
- Thun, H. (2006). Assessment of Fatigue Resistance and Strength in Existing Concrete Structures. Div. of Structural Engineering,. Ph D Thesis 2006:65: Luleå University of Technology.

- Tong, X. C. (2011). *Advanced Materials for Thermal Management of Electronic Packaging* (Vol. 30). Springer.
- Val, D. V., & Stewart, M. G. (2003). Life-cycle Cost Analysis of Reinforced Concrete Structures in Marine Environments. *Structural Safety*, 25(4), 343–362.
- Vu, K., & Stewart, M. G. (2000). Structural Reliability of Concrete Bridges Including Improved Chloride-Induced Corrosion Models. *Structural Safety*, 22(4), 313-333.
- Vu, K., Stewart, M. G., & Mullard, J. (2005). Corrosion-Induced Cracking: Experimental Data and Predictive Models. *ACI Structural Journal*, 102(5), 719 – 726.
- Wang, T.-L., & Huang, D. (1992). *Computer Modeling Analysis in Bridge Evaluation: Dynamic Response of Continuous Beam Bridges and Slant-Legged Rigid Frame Bridges*. Florida.: Department of Civil and Environmental Engineering, College of Engineering and Design, Florida International University.
- Wang, X., Nguyen, M., Stewart, M., & Syme, M. L. (2010). *Analysis of Climate Change Impacts on the Deterioration of Concrete Infrastructure*. Synthesis Report., CSIRO, Canberra.
- Weyers, R. E., Prowell, B. D., Sprinkel, M. M., & Vorster, M. (1993). *Concrete Bridge Protection, Repair, and Rehabilitation Relative to Reinforcement Corrosion: A Methods Application Manual*. Washington, DC: Strategic Highway Research Program, National Research Council.
- Weyers, Y. L., & E., R. (1998, November). Modeling the Time-to-Corrosion Cracking in Chloride Contaminated Reinforced Concrete Structures. *ACI Materials Journal*, 95(6), 675-680.
- Williamson, G. (2007). *Service Life Modeling of Virginia Bridge Decks*. Ph.D. Dissertation, Department of Civil and Environmental Engineering, Virginia : Virginia Polytechnic Institute and State University.
- Wright, J. R. (1995). Aims & Scope of the Journal. *Journal of Infrastructure Systems*, 1.
- Xu, Y., & Guo, W. (2003). Dynamic Analysis of Coupled Road Vehicle and Cable-Stayed Bridge Systems under Turbulent Wind. *Engineering Structures*, 25(4), 473–486.